IMPROVED MIDDLE EAR IMAGING WITH
OPTICAL COHERENCE TOMOGRAPHY
FOR CLINICAL OTOLOGY

by

Junzhe Wang

Submitted in partial fulfilment of the requirements
for the degree of Master of Applied Science

at

Dalhousie University
Halifax, Nova Scotia
July, 2023

Dalhousie University is located in Mi'kma'ki, the
ancestral and unceded territory of the Mi'kmaq.
We are all Treaty people.

To my loving parents, whose unwavering support and encouragement have been the pillars of my strength, and the guiding light on this remarkable odyssey of discovery, I dedicate this thesis with gratitude and love that no coherent light source could ever measure its depth.

Table of contents

List of tables

List of figures

Abstract

Conductive hearing loss (CHL) is a widespread and debilitating condition that affects millions of individuals worldwide. This impairment results from disruptions in the transmission of sound waves from the tympanic membrane (TM) to the inner ear. Unfortunately, existing diagnostic tools are often inadequate in pinpointing the root causes of CHL, leading to uncertainty when determining the most appropriate clinical management plans.

Optical coherence tomography (OCT) is an emerging imaging modality that offers non-invasive, high-resolution structural images of the middle ear. It also allows for measuring vibrations in middle ear structures in response to sound through an intact TM. Like all biomedical imaging methods, middle ear OCT (ME-OCT) aims to extract diagnostically significant information from the acquired images. However, its clinical application is limited by suboptimal image quality, due in large part to sidelobe artefacts and the effective imaging depth in the presence of optically opaque structures, such as cartilage tympanoplasty.

This thesis introduces two approaches to improve middle ear visualisation using OCT without modifying the existing imaging system. First, it presents a method that employs a convolutional basis pursuit framework to eliminate imaging artefacts related to strong reflections at tissue-air interfaces, which impede accurate morphology-based diagnoses. Second, it explores the potential of an optical clearing agent using a topical glycerol treatment to increase the transparency of cartilage grafts, allowing for OCT visualisation of the post-operative middle ear. The enhanced image quality could facilitate more precise CHL diagnoses based on morphological changes of middle structures, providing clinicians with more accurate and reliable diagnostics using ME-OCT.

List of abbreviations used

AOM	acute otitis media
ABG	air-bone gap
ADMM	alternating direction of multipliers method
ASE	amplified spontaneous emission
ADC	analog-to-digital converter
AR	anti-reflective
BPDN	basis pursuit denoising
CCD	charge-coupled device
COM	chronic otitis media
CI	cochlear implant
CP	cochlear promontory
CS	compressed sensing
CT	computed tomography
CHL	conductive hearing loss
CBCT	cone beam CT
CBPDN	convolutional basis pursuit denoising
CDL	convolutional dictionary learning
CSC	convolutional sparse coding
DAQ	data acquisition card
dB	decibels
DWT	discrete wavelet transform
DBR	distributed Bragg reflector
DV	Doppler vibrometry
ENT	ear, nose and throat
EPI	edge preservation index
ENL	equivalent number of looks
EAC	external auditory canal
FPGA	field-programmable gate array
FD-OCT	Fourier domain OCT
FT	Fourier transform
FSR	free spectral range
FWHM	full width at half maximum
gCNR	generalised contrast-to-noise ratio
GIS	gradual iterative subtraction
GPU	graphics processing unit

HL	hearing loss
HRCT	high-resolution CT
ISJ	incudostapedial joint
IDFT	inverse discrete Fourier transformation
IFT	inverse Fourier transformation
laser	light amplification by stimulated emission of radiation
MRI	magnetic resonance imaging
MEMS	micro-electromechanical systems
ME	middle ear
NA	numerical aperture
NIR	near-infrared
OCA	optical clearing agent
OCT	optical coherence tomography
OMP	orthogonal matching pursuit
OM	otitis media
PORP	partial ossicular replacement prosthesis
PSF	point spread function
PEG	polyethylene glycol
PPG	polypropylene glycol
PPP	purchasing power parities
PTA	pure tone audiogram
ROI	region of interest
RIN	relative intensity noise
SPSR	secondary peak suppression ratio
SOA	semiconductor optical amplifier
SNHL	sensorineural hearing loss
SLSR	sidelobe suppression ratio
SMSR	side-mode suppression ratio
SNR	signal-to-noise ratio
SPL	sound pressure level
SD-OCT	spectral-domain OCT
ST	stapedius tendon
SSIM	structure similarity index measure
SLED	superluminescent diode
SS-OCT	swept-source OCT
TD-OCT	time domain OCT

TM	tympanic membrane
VT-DBR	Vernier-tuned distributed Bragg-reflector
VCSEL	vertical cavity surface-emitting lasers
WHO	World Health Organization

Acknowledgment

As I draw closer to completing my Master's degree in biomedical engineering at Dalhousie university where I explored optical coherence tomography (OCT) as a non-invasive, radiation-free diagnostic tool for clinical otology, I find my mind wandering back through my incredible journey. It's a path that has led me from not even knowing the three ossicles to presenting research on middle ear imaging using OCT on a global stage. It is a reflection not only of my progress but of the collaborative spirit and nurturing environment that has made my exploration and contributions in the biomedical field possible.

First and foremost, I convey my sincere gratitude to my supervisor, Dr. Robert Adamson, for his dedication and commitment to nurturing my growth as a researcher. He provided me with an unparalleled opportunity with maximum amount of research freedom at every stage of my research journey.

I am also grateful to Dr. David P. Morris, whose generosity in providing direct clinical experiences through operating room and clinic shadowing, as well as unwavering encouragement, has been instrumental for me to appreciate the clinical rationale behind every project. Furthermore, the invaluable insights and feedback from Dr. Jeremy Brown as a committee member have significantly contributed to refining my work and elevating its quality. I am truly privileged to have collaborated with such knowledgeable and supportive mentors.

I have been fortunate to work alongside talented peers and clinical fellows who have selflessly shared their time and expertise. I would like to extend special recognition to Dr. Joshua Farrell. His invaluable contributions in establishing a robust software architecture for OCT imaging have made my wildest ideas possible. Additionally, I could not have asked for a better companion than him for the most unforgettable trip in Dubai. I want to express my gratitude to Dr. Gaurav Chawdhary, Dr. Mathieu Trudel and Dr. Floor Couvreur for imparting me with ear anatomy crash courses, meticulously preparing cadaver temporal bones, offering their clinical insights and exchanging idea after long days of surgery and clinics during their fellowships.

Chapter 1

Introduction

1.1   Challenges of imaging middle ear cavity through tympanic membrane

Middle ear optical coherence tomography (ME-OCT) has demonstrated promising capabilities in diagnosing conductive hearing loss (CHL) in vivo [1], [2] and providing valuable insights into understanding hearing mechanisms through ex vivo human cadaveric temporal bone studies [3]–[5] and small animal models [6], [7]. However, the clinical translation of ME-OCT faces challenges due to the narrow and angled external ear canals (EACs) [2], [8], which complicates the process of achieving comprehensive visualisation of the tympanic membrane (TM) and middle ear (ME) space. For example, in a study involving 120 patients to assess the degree of TM perforation [9], it was found that nearly 30% of EACs obstructed the line of sight, preventing adequate ME-OCT images from being obtained.

OCT can produce cross-sectional digital reconstruction of the ME space through the TM. However, its imaging capabilities are restricted when it comes to bone or soft tissue thicker than approximately 1 mm [8], as light cannot fully penetrate these structures. TM is a thin, delicate, and translucent structure that separates the middle ear from the EAC [10]. Functionally, TM conducts sound from the outer ear to the inner ear. When sound waves reach the TM, they cause it to vibrate. These vibrations are then transmitted through the ossicles, ultimately reaching the cochlea [11]. A key aspect of sound transmission is the integrity and health of the TM. For instance, damage to the TM, such as perforation (which can be addressed through tympanoplasty), or changes in its pathological state (e.g., otosclerosis or otitis media) can result in varying degrees of CHL.

Structurally, TM is composed of three distinct anatomical layers which is illustrated in Figure 1.1 (b) [10]: the outer epidermal layer, the fibrous middle layer (lamina propria) with radial and circular fibers, and the inner mucous membrane layer (mucosal layer). The outermost epidermal layer is a continuation of the epidermis from

the EACs, and it features a unique self-cleaning mechanism due to its lateral migration. The innermost mucosal layer is a thin, single-cell layer with a thickness of 1-10 μm [10], which connects to the mucosal lining of the middle ear cavity. Sandwiched between these two layers lies the fibrous middle layer, containing radial and circular collagen fibers that vary in organisation between the pars tensa and pars flaccida regions of the TM. The TM is held in place by a thick ring of cartilage with various diameter (0.6 [12] to1 cm [13]) and section – dependent thickness [10], [14], [15]. For example, the mean thickness of the pars tensa ranges between 79 and 97 μm [15], while the thickness in the pars flaccida region varies between 30 and 230 μm [15].
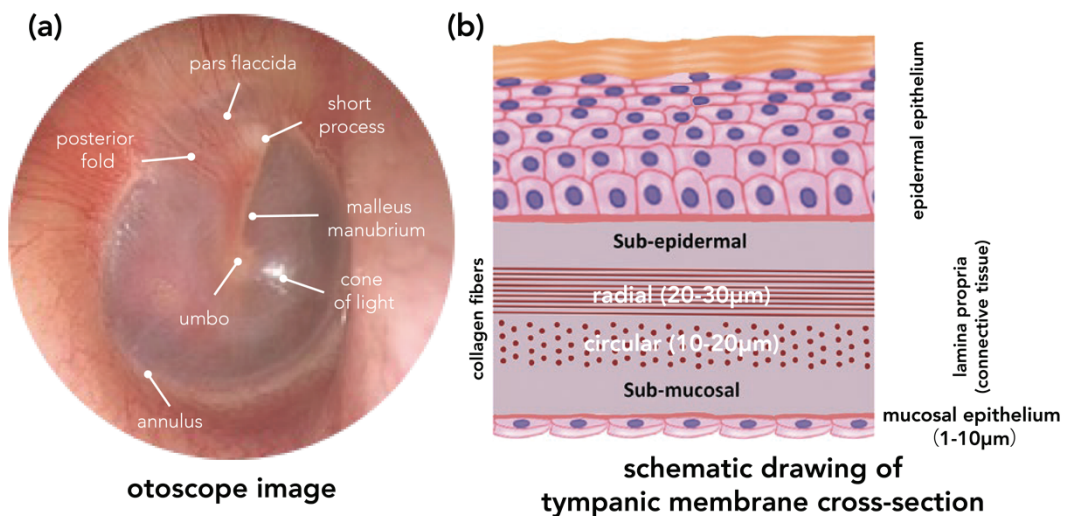
Figure 1.1: Otoscope image and cross-sectional view of the tympanic membrane (TM) where (b) is retrieved and modified with permission from [10].

Optically, TM impedes imaging of the ME space as light may not reach the targeted middle ear space or the detector [4] when scattering or absorption occurs in the TM on either the incident or reflected pass. Although the scattering coefficient in human TM tissue has not been directly measured, studies suggest that it is comparable to the dermis [4]. For instance, an ex-vivo experiment using a normal TM sample demonstrated a two-way transmission loss of 13.5 dB [4]. This finding aligns with a theoretical analysis of 19 dB [2], [4], which assumes of a TM thickness of 100 μm and a scattering coefficient of $\sigma_s = 22\ mm^{-1}$ [4].

In diagnosing CHL using OCT, it is of clinical interest to capture the entire volume of the ME space without disturbing the TM [2], [4], [8]. While OCT imaging of

the TM itself offers clinical value [9], [14], [15], its presence poses significant challenges for further investigation of ossicular involvement. These challenges primarily arise from the unique optical properties of the TM. This includes substantial optical losses due to scattering within the TM, and the strong reflectors it produces when the imaging light is normal the TM. These factors, coupled with sidelobe artefacts, can obscure weaker reflections emanating from structures within the middle ear. Figure 1.2 features a selection of middle ear OCT images sourced from various studies [3], [4], [16]–[18]. The images highlight the capabilities of various research OCT systems that have been reported on. Of particular note in these high-quality images is the prevalence of sidelobe artefacts (red arrows), the severity of which varies between systems, and which are most prominent at the tissue-air interface on the proximal aspect of the TM. These challenges become more pronounced in cases of increased TM thickness due to either pathological thickening, calcification of the TM or the use of graft material in the tympanoplasty [2], [8], which limits the effective imaging depth that OCT can achieve.
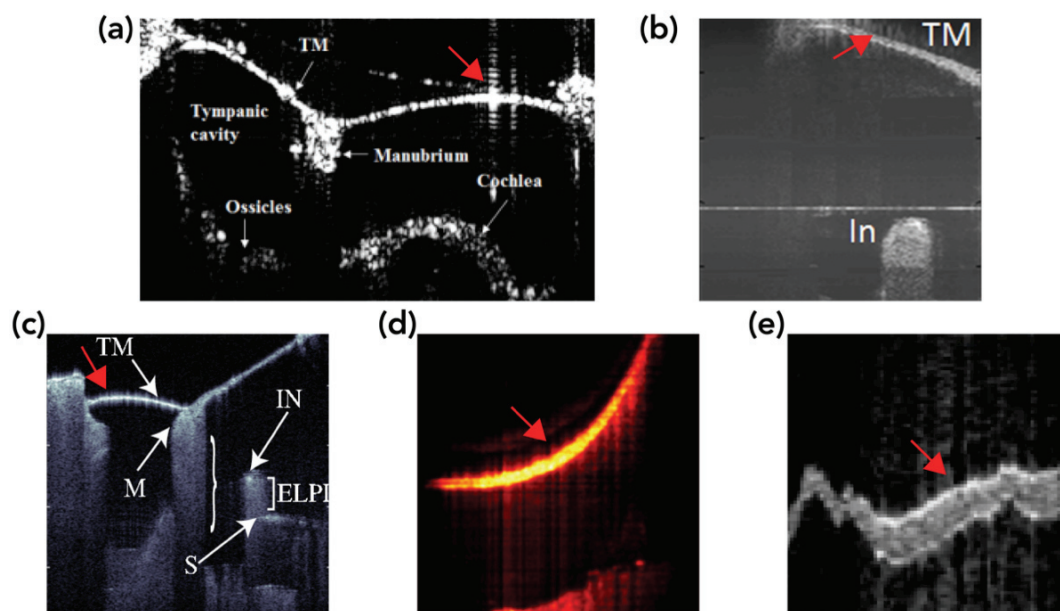
Figure 1.2: Sample middle ear OCT images from published literature with red arrow indicates the presence of the sidelobe artefacts. All images were retrieved and modified with permission from their respective copyright holders. (a) 2D image of in-vivo, whole mouse ear structure, adapted with permission from [16] © the Optical Society; (b) structural image of right temporal bone after mobilization of incus and stapes and separation of the incudostapedial joint [19]; (c) 2D image of a human cadaveric ear [4]; (d) 2D image of a human ear with the tympanic membrane as the bright structure at the top of the image, adapted with permission from [17] © the Optical Society; (e) healthy normal TM, retrieved under Creative Commons CC BY 4.0 license [18].

While primarily recognised as a research tool in otology, ME-OCT has shown significant promise as a clinical diagnostic imaging modality. ME-OCT technology enables a three-dimensional (3D) visualisation of the middle ear space through an intact TM, all without exposing patients to radiation. ME-OCT could potentially improve our understanding and clinical management of CHL. In essence, ME-OCT presents a non-invasive, radiation-free alternative for clinicians aiming to explore ear-related pathologies. However, the translation of ME-OCT into clinical settings is met by several limitations and challenges. Being a line-of-sight modality, its imaging capabilities can be hampered by obstructions like bone or soft tissue with thickness of more than 1mm. Furthermore, ME-OCT is susceptible to imaging artifacts. These artifacts, caused by multiple scattering and from imperfection in the axial PSF combine with bright reflections at the TM surfaces, can limit the amount of clinically useful information obtainable from ME-OCT. Unless these challenges are properly addressed, they can

create significant barriers to the adoption of ME-OCT as a point-of-care diagnostic technology in clinical otology.

1.2 Organisation of this thesis

This thesis is organised into one introduction chapter providing the motivation of this work, three self-contained chapters and a conclusion chapter.

Chapter 2 lays the background information for the thesis by offering an extensive literature review and background information on hearing, conductive hearing loss (CHL) existing diagnostic tools in clinical otology, optical coherence tomography (OCT), and its application in middle ear imaging. This chapter examines the current state of knowledge and research in the field, identifies gaps and opportunities for further exploration, and establishes the research questions and rationale for subsequent chapters.

Chapter 3 provides a detailed account of the research on a sparsity-regularised, complex, blind deconvolution method for removing sidelobe artefacts and stochastic noise from OCT images. It also discusses the potential limitations and relevance of the chosen methodologies in the context of middle ear OCT.

Chapter 4 focuses on addressing the optical loss in transmission caused by increased eardrum thickness because of cartilage tympanoplasty. The chapter presents a detailed ex-vivo investigation of the feasibility of using a topical glycerol treatment to enhance the transparency of cartilage grafts and enable OCT visualisation of the post-operative middle ear.

In Chapter 5, the main findings from the three chapters are synthesised, drawing connections between them and reflecting on their broader implications. This section also suggests avenues for future research, which could accelerate the clinical translation of OCT in otology.

Chapter 2

Background

2.1   Epidemiology of hearing loss

The sense of hearing is one of the most critical senses humans possess, as it plays a crucial role in our daily communication and emotional connection with others [20], [21]. Our sense of hearing allows us to enjoy music, appreciate the sounds of our environment, and communicate with those around us, which significantly improves to our quality of life by adding richness and depth to our sensory experiences [20]. Without the ability to hear, we would miss out on the sound of a loved one's voice, the laughter of a child, or the soothing sounds of nature.

Hearing loss (HL) is one of the most common chronic conditions among older Americans [22], it is estimated that approximately 5.2 million children and 26 million adults in the United States alone have significant noise-induced HL [23], [24]. Around 2 to 3 of every 1,000 children are born with a detectable level of hearing loss in one or both ears, while approximately 15% of adults aged 18 and over in the United States report having difficulty hearing [25]. The strongest predictor of hearing loss is age, with the highest levels occurring in the 60 to 69 age group [26]. Men are nearly twice as likely as women to experience hearing loss among adults aged 20 to 69 [26]. Standard hearing examinations indicate that one in eight people aged 12 or older in the United States has HL in both ears [27].

In Canada, the estimates of hearing loss prevalence have historically been based on self-reported data, which may not accurately reflect the true extent of hearing impairment. A recent study conducted by Statistics Canada based on a combination of collected audiometric and self-report data from more than 3,000 Canadians shows that the Canadian estimates of hearing loss are consistent with reporting from countries like the United States [28]. Based on audiometric measurements (i.e., a pure-tone average of four frequencies), 19.2% (i.e., 4.6 million) of Canadians between the age of 20 to 79 have hearing loss in at least one ear, and 35.4% have high-frequency hearing loss (HL) [28].

These levels were higher than the self-reported estimate of 3.7%. The prevalence of hearing loss increases with age and was more common in men and those with lower income and education levels [28].

The severity of hearing loss, as clinically determined by audiometry, is based on perceptual thresholds defined in decibels (dB HL) [29]. Symptoms of hearing loss may include difficulty in understanding words, muffled speech, trouble of hearing consonants, and frequently asking others to repeat conversation more slowly and loudly [30]. People of all ages, ranging from infants to the elderly, can experience hearing loss [31]. For children, hearing loss hinders their linguistic, cognitive, behavioural, and academic developments [32]. Studies [24], [33] indicate that school-age children with mild (26 – 60 dB HL [25], [29]) to moderate hearing loss (41 – 60 dB HL [25], [29]), on average, do not perform as well in school as children with no hearing loss. This gap in academic achievement widens as they progress through school if they do not receive the proper intervention. In adults, hearing loss (HL) has important implications for patient quality of life and proper management of hearing loss can improve one's overall health outcomes [30]. In the elderly, hearing loss also correlates strongly with depression as frustration arises from the functional decline of one's communication ability [22], [30].

Hearing is a critical aspect of how we communicate and connect emotionally and intellectually. Its loss, if not appropriately addressed, can also lead to a significant economic cost (i.e., nearly one trillion international dollars[a] [34]) and societal burden [30], [35].

According to a recent report by the World Health Organization (WHO) [36], by 2050, nearly 2.5 billion people globally will be living with some degree of hearing loss. This report not only brings to light the worldwide prevalence of hearing loss and its consequences but also draws attention to the current deficiency in ear health and hearing care services worldwide. Based on a model that uses hearing aid usage as a reference, the report suggests an 83% disparity in access to hearing healthcare [32], [37], and it further

---

[a] International dollars here refer to purchasing power parities (PPPs) international dollars [2]. PPPs are economic measures used to compare the standard of living between different countries by considering the relative prices of goods and services in different regions and they are commonly used in economic analysis for an accurate comparison of cost of good or service.

elucidates several reasons for this gap, including the lack of accurate information and stigmatizing mindsets surrounding ear diseases and hearing loss [36], [38], [39]. Even among healthcare professionals, there is often a considerable knowledge gap regarding the prevention, early detection, and management of hearing loss and ear diseases, which ultimately result in suboptimal clinical outcomes [32], [40], [41]. Given the high prevalence and significant societal impact of hearing loss, it is critical to screen, identify, and adequately manage patients with hearing issues at an early stage [22]. However, this report identifies that in low- and middle-income countries, ear and hearing care is often not integrated into healthcare systems, which further exacerbates the problem. This situation is compounded by a severe shortage of healthcare professionals in this field [36], [37], [42], making it challenging for them to access the necessary tools and support for adequate hearing care. Among the low-income countries surveyed [36], [42], 78% have fewer than one ear, nose and throat (ENT) specialist per million population, while 93% have fewer than one audiologist per million. Even in countries with relatively high proportions of hearing care providers, inequitable distribution of healthcare resources and other factors can limit access to essential ear health services [36], [39].

2.2 Physiology and anatomy of hearing

The human ear, a remarkable sensory organ, is capable of processing a broad spectrum of sound frequencies that ranges from 20 Hz to 20 kHz [a] [35]. Its ability to detect sounds as low as 0 dB SPL[b] [44] and tolerate sounds as high as 130 dB SPL (e.g., sound from a jet engine when one stands in its proximity [45]) for brief periods of exposure is a testament to its exceptional sensitivity and versatility [11].

Among the range of frequencies the ear can detect, signals between 500 and 4,000 Hz are especially well detected [35]. These frequencies are of particular importance for speech processing. The process by which the ear detects and interprets sound is a

---

[a] Frequency, measured in Hertz (Hz), quantifies the number of sound vibrations occurring in one second. Following the conventions in clinical audiology [43], frequency is divided into octave intervals rather than a linear scale. An octave represents a frequency that is double that of a given frequency.

[b] The intensity of sound, which quantifies the magnitude of a sound wave, is expressed in logarithmic units using the Sound Pressure Level (SPL) measured in decibels (dB). The formula to calculate dB SPL is 10 log (pressure/reference pressure), where the reference pressure is fixed at 20 μPa RMS [43].

complex one that involves physiological, anatomical, and cognitive mechanisms [11], [35].
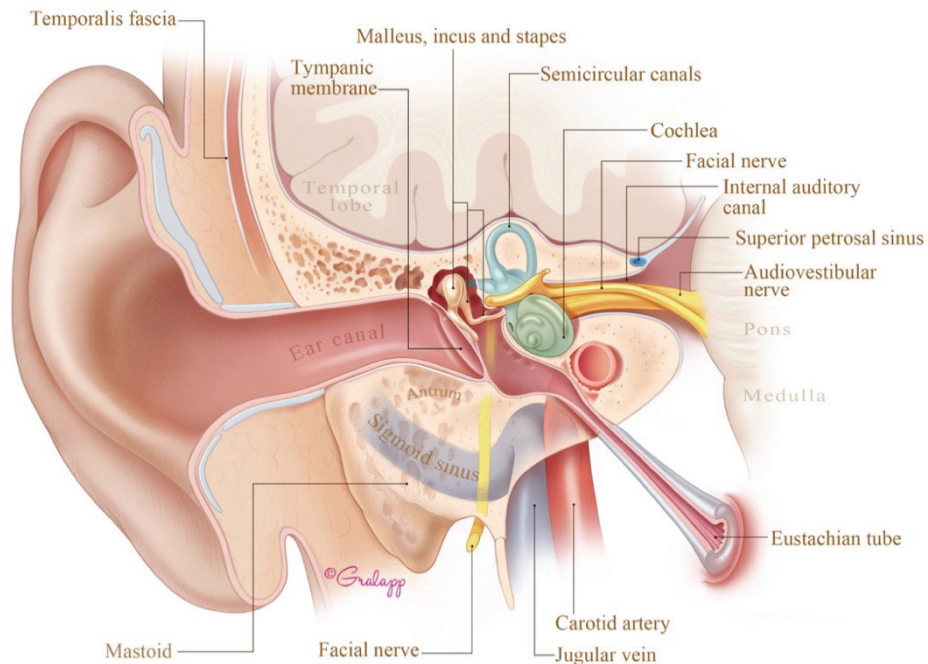
Figure 2.1: Coronal view of the anatomy of the ear © (2023) Chris Gralapp, used with permission [46].

Human ear can be divided into three main regions: the external ear, the middle ear (ME), and the inner ear. The external ear consists of the auricle (or pinna) and the external auditory canal (EAC) [10]. EAC is a cartilaginous structure that is often narrow and curved, with an approximate length of 2.5 cm [12] and a small opening of 0.6 cm [12] in diameter. Hearing is accomplished by collecting sound-induced air pressure change in the external ear [35], where sound travels down the EAC to the tympanic membrane (TM) or eardrum: a thin membrane with a thickness of 100 μm to 280 μm [47]. TM separates the external canal from the middle ear space and passes vibrations to the ossicular chain [22]. The middle ear, which is located within the temporal bone on each side of the skull [10], houses three bony structures (collectively known as the ossicles or ossicular chain): the malleus, incus, stapes, and supporting ligaments [10], [11], [22] – that amplify and transmit sound vibrations to the inner ear through the stapes

footplate[a] [11]. The inner ear contains the cochlea, a spiral-shaped structure that is responsible for converting the mechanical motions propagated from the ossicular chain into neural signals [31], [35]. When sound waves enter the cochlea, they cause the hair cells to vibrate – specialised sensory cells that respond to specific frequencies of sound (i.e., tonotopic mapping of the sound, the base of the cochlea senses higher frequencies, whereas the apex of the cochlea senses lower frequencies [11]), which, in turn, causes the release of neurotransmitters that stimulate adjacent neurons [11]. The neural signals generated by the hair cells are transmitted to the auditory cortex in the brain via the auditory nerve.

2.2.1 Forms of hearing loss

Overall, the physiology of hearing involves a complex interplay between the anatomical structures of the ear and neural pathways which lead to the sensation of sound [11]. Unfortunately, any disruption which can occur at any age and for a variety of reasons can result in hearing loss [27]. There are three main categories of hearing loss, each with its own unique causes and characteristics. The first type is sensorineural hearing loss (SNHL) and it encompasses disorders that affect the inner ear (e.g., damaged hair cells) or the neural pathway to the auditory cortex that impedes the conversion of mechanical vibration to neuroelectric signals [25], [27]. SNHL is the most common type of hearing loss and can be caused by a wide range of factors [22], [33], including aging, exposure to loud noises, certain medications, genetic factors, and trauma [28], [31], [32]. As there is no known treatment for repairing the hair cells, cochlear implantation, which directly stimulates the vestibulocochlear nerve, is the only solution in the case of profound (≥ 91 dB HL [25]) hearing impairment [48], [49].

On the other hand, conductive hearing loss (CHL) typically involves abnormalities of the TM and middle ear, which interferes with the normal transmission and/or the amplification of sound and conversion of sound to mechanical vibration [22], [25], [29]. This type of hearing loss can be temporary due to cerumen impaction of the

---

[a] Amplification of sound induced pressure is achieved by efficiently utilising the lever-like arrangement of ossicles as well as area ratio between the TM and stapes footplate [11].

EAC [25], [32], and also be caused by conditions such as ear infections [32], fluid accumulation [25], [27] in the middle ear or damage to the TM or ossicles [22].
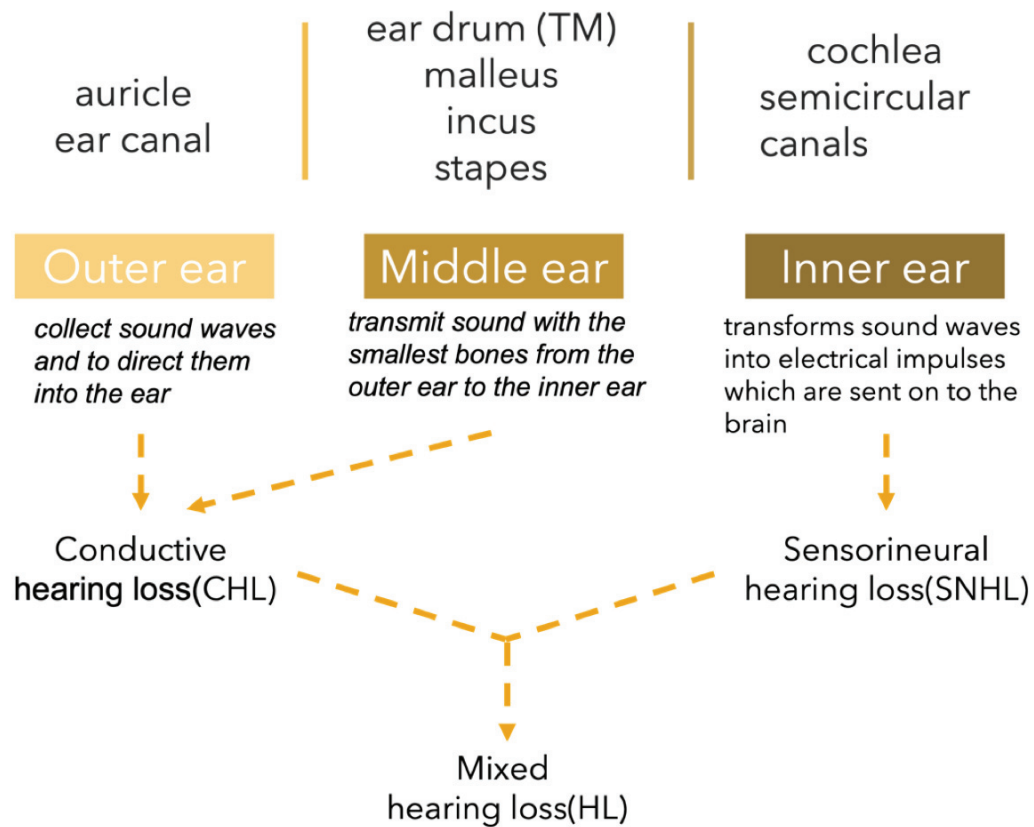
Figure 2.2: Basic hearing loss types

Finally, mixed hearing loss occurs when both conductive and sensorineural hearing loss are present, which indicates that there may be damage to both the outer or middle ear and the inner ear or auditory nerve [31], [36]. Pure-tone audiometry test [43], [44], a clinically standard method for classifying hearing loss, charts air and bone conduction levels across all tested frequencies and the difference between these levels is known as the air-bone gap (ABG). Hearing loss, regardless of its type, can lead to substantial health and quality of life burdens – communication difficulties [27], [42], cognitive decline [33], and mental health issues [32], if hearing loss is not managed properly and in a timely manner.

2.3   Conductive hearing loss: implications

This work focuses on conductive hearing loss (CHL). Clinically, CHL is considered when there is an ABG of 15 dB or greater present at 500 or 4,000 Hz during pure-tone audiogram (PTA) evaluation [30], [50]. A study suggests that CHL is prevalent in 2.26 % (i.e., 37 / 1636) of the adult population in the age group between 48 to 92 years old [50]. CHL is also common among the pediatric population, where it is usually caused by acute otitis media (AOE[a]) and its complications. A study conducted on primary school children found that 15% of them had hearing loss, with 88.9% of those cases being conductive in nature [51].

Similarly, a Canadian study conducted on school children from kindergarten to grade 6 found that 19% of them had hearing loss (HL), with 93% of those cases being conductive. The same study also found that TM perforations was present in 37% of cases with unilateral loss and 46% of cases with bilateral loss [52]. Most middle ear pathology, whether acquired or congenital, leads to some degree of hearing loss [25]. Pathologies such as TM perforations [22], [25], tympanosclerosis [25], [53], ossicular discontinuity or fixation [1], [8], and cholesteatoma [54], [55] are common disorders that contribute to the prevalence of CHL.

2.3.1   Current diagnosis of conductive hearing loss

While conductive hearing loss (CHL) is often treatable with surgery, the diagnosis of middle ear disorders remains challenging in daily otologic practice due to the complexity of middle ear anatomy and physiology [56]. Clinicians rely on information provided by a combination of patient history, an oto-microscopic examination [8], [57], functional auditory assessment [22], [58] and diagnostic imaging [36], such as high-resolution computed tomography (CT) [55], [59], and/or magnetic resonance imaging (MRI) [56], [60] to form a diagnostic opinion.

Prior to implementing a treatment plan, clinicians must integrate all available information to develop a thorough understanding of the patient's pathological condition.

---

[a] According to data, there is a high incidence rate of acute otitis media (AOM) at 10.85%, resulting in over 700 million cases each year, with children being the majority of those affected [32].

Below are brief descriptions of the current diagnostic tools available to hearing specialists, i.e., audiologists and otolaryngologists [22].
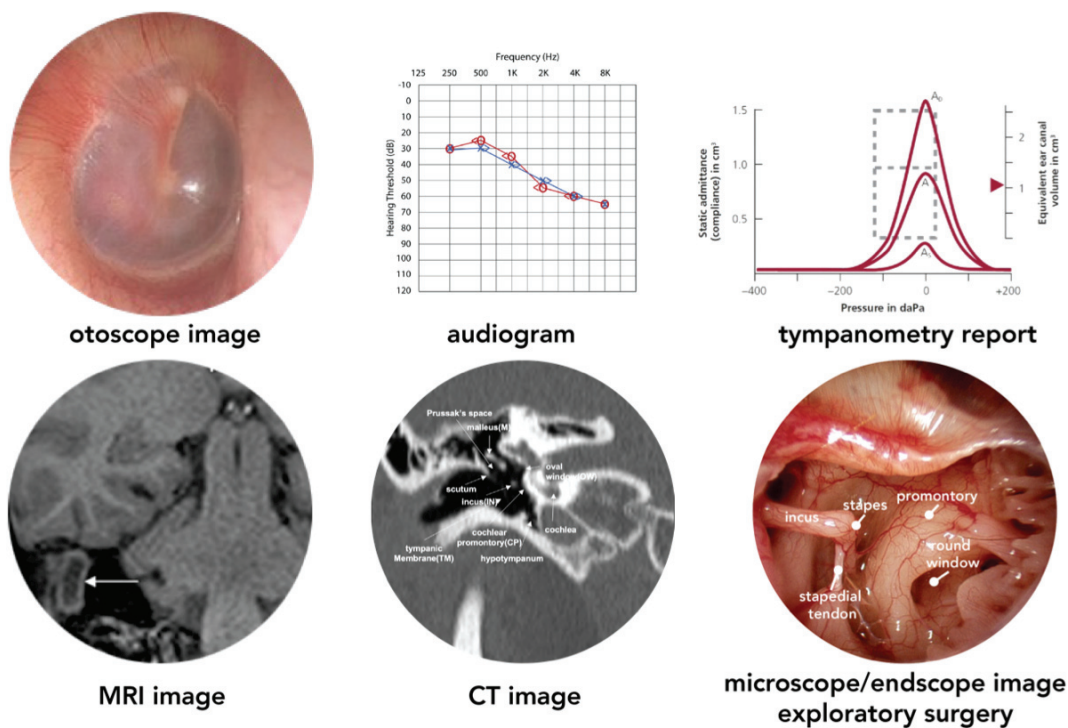
Figure 2.3: Current diagnostics in clinical otology

Optical examination

The otoscope is a special-purpose, low magnification handheld microscope used to assess the EAC and TM for structural integrity [22]. It can confirm conditions including TM perforation or cerumen impaction through illumination and magnification of the TM [25]. However, its usefulness is limited as the opacity of the TM precludes direct visualisation of the middle ear space.

Air-bone audiometry

Pure-tone audiometry is a standard auditory assessment that evaluates the degree and types of hearing loss [25]. By sweeping through sounds at different levels and frequencies for each ear, using either air conduction (i.e., sounds presented through the headphones) or bone conduction (i.e., sounds presented through a vibrator placed behind the ear) [43], it charts patients' reported hearing thresholds at various frequencies from 250 Hz to 8 kHz [22], known as an audiogram. The audiogram also reveals the ABG,

which is the difference between the air and bone thresholds [43]. The ABG is a key metric for evaluating the outcomes of middle ear surgeries with the aim to address CHL, such as tympanoplasty with or without middle ear reconstruction [61], [62]. Although PTA can reliably detect SNHL (i.e., with a 91.4% sensitivity[a] and 93.5% specificity[b] [64]), it lacks desired specificity for identifying middle ear pathologies related to conductive hearing loss [43], [65].

Tympanometry

Tympanometry is a routine functional test that evaluates the mobility of the TM in response to changes in air pressure [22], [25]. It assesses middle ear function based on acoustic immittance – a combination of impedance and admittance of the ear [43]. A small probe is placed in the sealed ear canal during the test to generate sound and quasi-static pressure changes – small, gradual changes in air pressure over a long period of time. The measurement is done by delivering a pure-tone signal (266 Hz for adults and 1,000 Hz for children [43]) at a constant sound pressure level – 85 dB SPL. A curve that represents immittance over sound pressure level is referred to as a tympanogram. The characteristics of the tympanogram serve as indicators for middle ear pathologies. For example, a type A tympanogram indicates normal middle ear function, while a type B tympanogram indicates an increased middle ear mass such as the presence of middle ear fluid.

However, tympanometry measurements are considered to be only suggestive of a diagnosis [66] as the measurements are heavily influenced by the admittance of the tympanic membrane (TM), which can vary widely between individuals. Consequently, this method is less specific for diagnosing middle ear pathologies other than otitis media [25], [67].

Radiological imaging

Complementary to each other [56], [68], CT and MRI have been well integrated into the clinical otology workflow, long-serving as the preferred visualisation techniques for

---

[a] Sensitivity = true positive / (true positive + false negative) [63]
[b] Specificity = true negative / (false positive + true negative) [63]

middle ear pathology investigation and surgical planning. CT is excellent at visualising complex osseous structures in the temporal bone – reliably identifying malleus (sensitivity: 94 %, specificity: 100 % [69]), incus (sensitivity: 86 %, specificity: 84 % [69]), stapes incus (sensitivity: 80 %, specificity: 85 % [69]) as well as small boney erosions in the lateral semicircular canal (sensitivity: 100 %, specificity: 97.73 % [70]) but has poor soft-tissue contrast, exhibits metal-induced artefacts[a] in the presence of middle ear prosthesis or cochlear implant (CI) [1] and exposes the patient to radiation.

MRI, on the other hand, is great at differentiating soft-tissue or fluid-containing structures but does not provide adequate bony-tissue contrast [68], [72] and exhibits strong susceptibility artefacts due to the presence of air in the middle ear[b] [74]. However, both CT (400 μm [2]) and MRI (300 μm [2]) have insufficient spatial resolutions to adequately resolve microstructures (e.g., TM and middle ear structures) in the middle ear space as illustrated in

Figure 2.4, and provide suboptimal visualisation of the middle ear. This resolution gap can lead to low specificity in diagnosing middle ear pathologies.

However, pre-operative investigations may not always result in a reliable diagnosis, as the available tools may lack the desired specificity and sensitivity [75], [76]. For example, pre-operative misdiagnosis contributes to the observed 15% failure rate for middle ear surgeries [77] which means that patients are not receiving the treatment they need and may have to undergo further procedures. It has also been reported that about 15% [77] of primary surgeries and up to half of the revision surgeries failed to restore hearing [78].

---

[a] Metal objects can degrade CT images by creating streaks, shadows, or dark bands. This is due to beam hardening, where the high-energy X-ray beam is preferentially absorbed by the metal, resulting in fewer photons reaching the detector [71].

[b] Air-tissue interfaces can cause magnetic field distortion, known as susceptibility artefact, resulting in signal loss or distortion in the image. This makes it difficult to see the structures of interest [73].
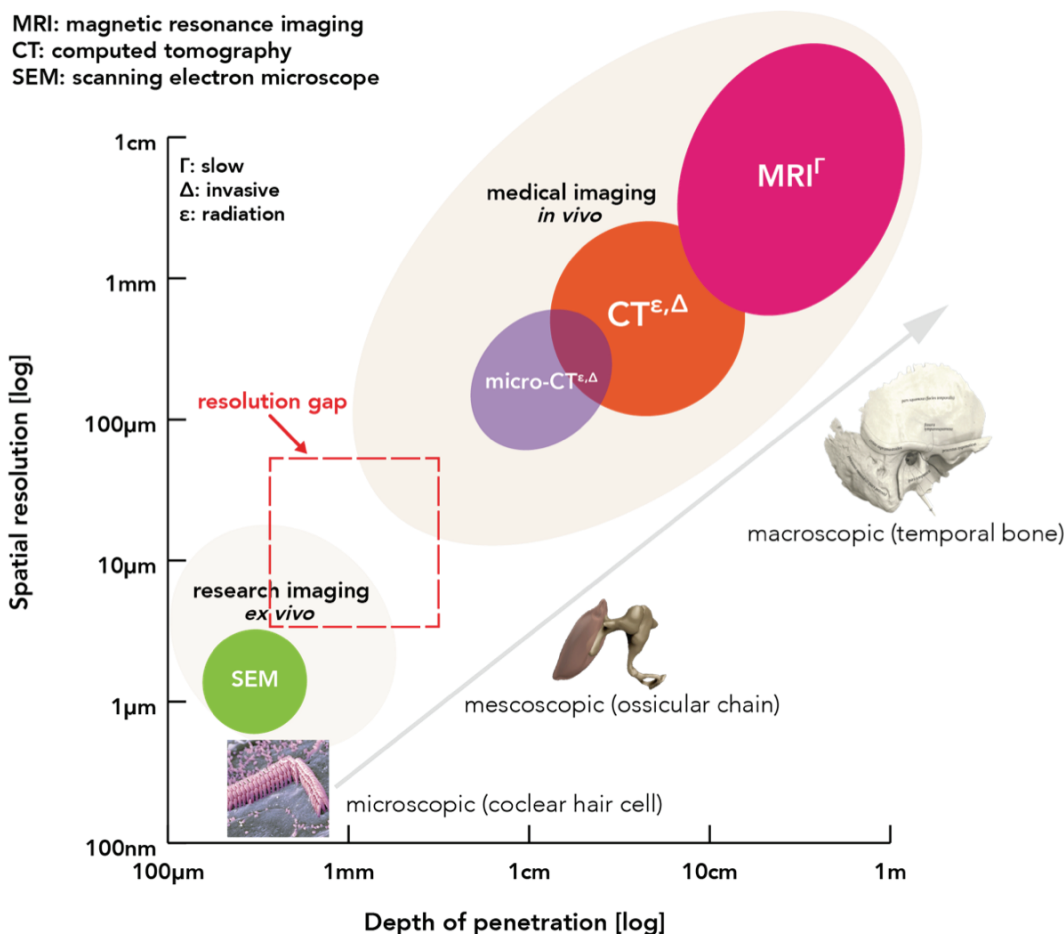
Figure 2.4: Depth of penetration vs. spatial resolution comparison on imaging modalities commonly used in otology diagnostics and hearing research. Here the term CT encompasses standard clinical high-resolution CT (HRCT) and cone beam CT (CBCT), which have a spatial resolution of 400 μm [2] and 200 μm [79], respectively.

In some cases, clinicians may need to resort to a more invasive diagnostic measure, such as exploratory tympanotomy, which allows direct visualisation of the middle ear space [76] in order to obtain a conclusive diagnosis [62], [75], [76]. Exploratory tympanotomy is considered a relatively safe option for investigating middle ear disorders with a low surgical complication rate but it is still invasive and comes with risks, such as accidental injury of chorda tympani [62]. Therefore, there is a significant clinical need for diagnostic tools that can provide a non-invasive visualisation of the structural and functional state of the middle ear.

2.4   Optical coherence tomography (OCT)

A non-invasive imaging technique known as optical coherence tomography (OCT) has the potential to improve conductive hearing diagnostics [1], [2], [4], [8]. OCT measures light waves reflected from tissue to create depth-resolved images of the structure being studied which bears similarities to ultrasound images [80]–[82]. In OCT images, subsurface structures become visible and can be differentiated based on differences in their optical properties at the OCT wavelengths [81].

The choice of optical wavelength range for OCT depends on several factors including the specific application, the availability and cost of light sources. For example, in ophthalmology, OCT typically operates in the range of 650 - 1300 nm as it offers a good balance of penetration depth, low scattering and absorption in the cornea and vitreous, and the availability of low cost, high power superluminescent diodes and swept source lasers [80], [82], [83]. However, some applications may require longer or shorter wavelengths, depending on the specific imaging needs [2], [4], [8], [84].

2.4.1   Time domain OCT (TD-OCT)

OCT was first described in 1991 by Fujimoto et al. [81] as a novel imaging method for the retina. Since then, it has become a powerful non-invasive clinical imaging technique with exceptional spatial resolutions at the micro-meter level [82], [85]. OCT has revolutionised clinical practice and is considered the standard of care in ophthalmology [8], [86]. OCT also has found biomedical applications in various fields, such as dermatology [87] gastroenterology [87], lung imaging [88], imaging of the oral [89] and respiratory tract mucosa [90] and dental imaging [91].

The fundamental principle of OCT is low-coherence interferometry [82], [83], which utilises low-coherence or partially coherent light[a] to localise structures by correlating interfering light that is back-scattered from the sample arm, E_s, with the light reflected from the reference arm, E_r. In OCT, a photodetector measures the intensity of the interfered light I_o, which is proportional to the total electrical field as described by its relationship $I = |E|^2$.

---

[a] coherent light refers light that maintains a consistent phase over distance.

$$I_o \sim \langle E_r E_r^* \rangle + \langle E_s E_s^* \rangle + E_s E_r^* \mathrm{e}^{-i2k(\Delta l)} + E_r E_s^* \mathrm{e}^{-i2k(\Delta l)} \tag{2.1}$$

$E_r E_r^*$, often referred to as the "DC" term, is time average of the square of the electric fields or irradiance[a] of the light from the reference arm and represents the dominant component in the detector current. $E_r E_r^*$ is independent of sample reflectivity and optical pathlength difference Δl. The autocorrelation term $E_s E_s^*$, describes the interference caused by multiple reflectors present within the sample. In conventional OCT, this interference is a source of unwanted artifacts, but it can be minimized by ensuring that the reference intensity is much higher than the sample intensity. The terms of interest, the cross-correlation term $E_s E_r^* \mathrm{e}^{-i2k(\Delta l)} + E_r E_s^* \mathrm{e}^{-i2k(\Delta l)}$, depend on the intensity in the sample and reference arms, the path length difference between the sample and reference arms, and the sample reflectivity. To ensure that this desired term is larger than the undesired autocorrelation term $E_s E_s^*$, the system is designed such that $|E_r| \gg |E_s|$. Some authors describe the relative increase in the cross-correlation term as compared to the autocorrelation term in terms of a "gain" applied to the sample signal by the reference arm signal [82].

The first-generation OCT technology, TD-OCT [86], employs this concept and obtains depth information as a function of time by moving a reference mirror with a motorized actuator over the depth range. The intensity at the output of the interferometer is measured with a photodetector, while changing the optical path length in the reference arm. In TD-OCT, interference fringes can only be observed when the relative optical path length difference between the sample (containing objects of interest) and reference arms machetes within the coherence length of light source, allowing different reflectors to be spatially resolved by translating the reference mirror along the optical axis in TD-OCT. The envelope of the interference pattern (known as the A-line) represents the depth-resolved optical reflectance of the sample arm at a specific lateral position along its axial direction.

---

[a] In the realm of OCT literature [82], [92], both irradiance and intensity are frequently encountered terms that describe the distribution of light's power or energy. Although often used interchangeably, a distinct difference exists between them [93]. Irradiance focuses on the energy flow arriving at the detector, and it measures the flux per unit area. In contrast, intensity takes the point view from the source, and it is described as the flux per solid angle.

Two (2D) or three-dimensional (3D) cross-sectional images can be constructed by obtaining a set of raster-scanned A-lines along a desired lateral direction. OCT images are usually displayed in grayscale, where the horizontal axis corresponds to the direction of transverse or lateral scanning, and the vertical axis corresponds to the direction of axial scanning. To account for the high dynamic range and speckle noise often present in OCT images, pixel intensity in an OCT image is typically mapped to the logarithm of the interferogram envelope magnitude [86] which compresses the dynamic range and enhances the image contrast.
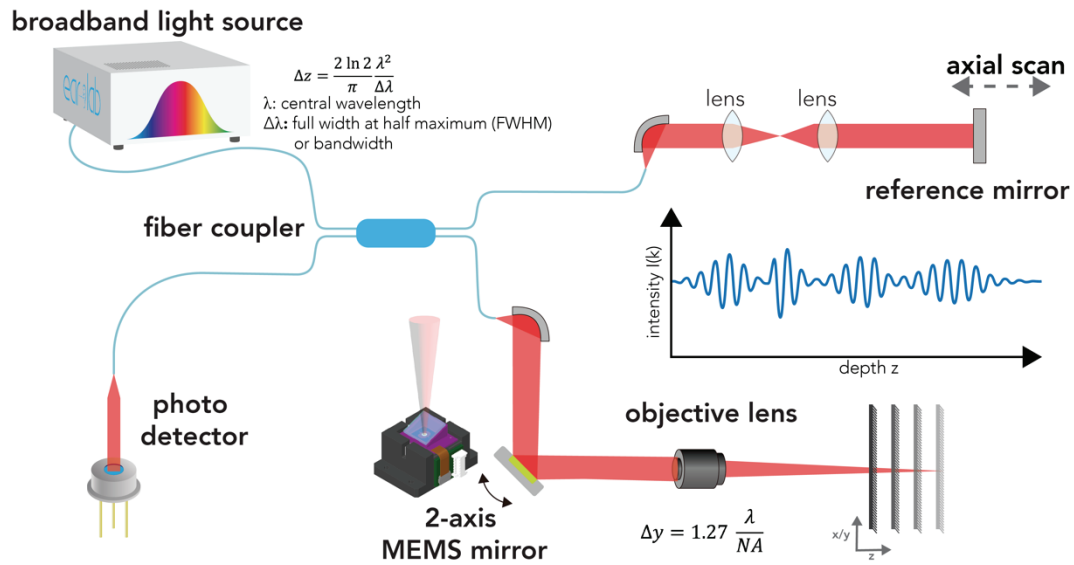
Figure 2.5: Time domain OCT (TD-OCT), in a Michelson-type configuration, performs imaging by measuring the echo time delay of reflected light using low-coherence interferometry.

In TD-OCT, light is emitted from a broadband source, such as a superluminescent diode (SLEDs). The characteristics of the light determine one key OCT performance metric: the axial resolution, Δz, or coherence length, l_c. Assuming that the spectral distribution of SLEDs is Gaussian [82], [83], [94], the axial resolution is given by:

$$\Delta z = \frac{l_c}{2} = 2 \frac{\ln 2}{\pi} \frac{\lambda_o{}^2}{\Delta \lambda} \tag{2.2}$$

where λ_o is the center wavelength, and $\Delta \lambda$ is the full width at half maximum (FWHM) spectral bandwidth. As the axial resolution is inversely proportional to the spectral bandwidth, broadband source is preferred to achieve a higher axial resolution. In OCT, the lateral resolution is decoupled from the axial resolution and is governed by its optical

design. The lateral resolution is inversely proportional to the numerical aperture (NA)[a] [94]:

$$\Delta y = 1.27 \frac{\lambda_o}{NA} \tag{2.3}$$

In 2001, Pitris et al. [3] demonstrated the feasibility of using a TD-OCT system to acquire cross-sectional images of the middle ear space in a human cadaveric temporal bone through the intact tympanic membrane (TM) [3], [8]. Since then, OCT has been of significant interest to the scientific community as a tool for clinical otology.

Although TD-OCT is simple to construct and offers a long-depth scan range, TD-OCT suffers from [86] slow imaging acquisition speed and an unfavourable trade-off between imaging depth, imaging acquisition speed, and sensitivity[b] [4], [82], [94], [95].

2.4.2 Fourier domain OCT (FD-OCT)

An alternative solution to TD-OCT is Fourier domain OCT (FD-OCT) [95], which is used in most modern OCT systems owing to superior acquisition speed and sensitivity [95].

---

[a] The numerical aperture of an optical system is defined by $NA = n \cdot \sin\theta$ where n is the refractive index of the medium between the lens and the object and θ is half-angle of the cone of light that can enter the lens. A larger NA indicates that more light can pass through the lens.

[b] Sensitivity here refers to the minimum detectable signal as compared to an ideal reflector in the OCT system [82], [83].
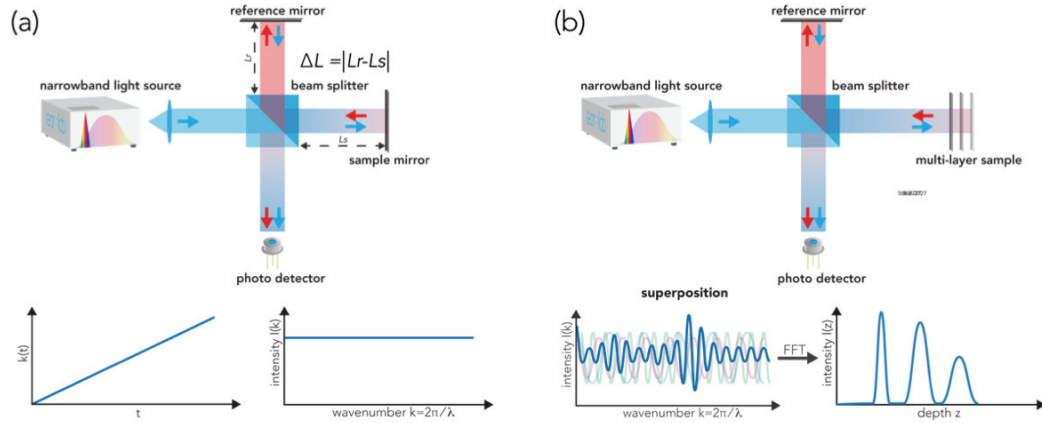
Figure 2.6: Illustration of Fourier Domain OCT (FD-OCT) utilising a Michelson interferometer, featuring a tunable swept laser source and photodetector. (a) the frequency of the interference spectrum changes as the wavelength in the light source changes over time, due to the fixed, relative path length difference. ΔL. (b) depth-resolved information of a multi-layer sample is encoded in the frequency domain of the interference spectrum. This information can be obtained by performing a Fourier transform of the detected spectral interference pattern.

In TD-OCT, axial detection is performed sequentially through the mechanical translation of the reference mirror [96] whereas FD-OCT samples all axial depths simultaneously, enabling high sensitivity and fast acquisition [85], [96], [97]. In FD-OCT, a spectral interferogram signal is generated by performing a spectrally resolved measurement of the interference intensity between the light reflected from the sample and light from a fixed reference arm, as shown in Figure 2.6 [82]. The frequency of the cosine term, seen in (2.6), in the interferometric signal is proportional to the relative path length difference between the reflector in the reference arm and the sample arm. Meanwhile, the amplitude of the interferometric signal encodes information about the sample reflectivity. As reflected light from all axial depths in the sample is captured and modulated in the source spectrum, all the spectral components are captured simultaneously [96], [97] which leads to faster acquisition speed and higher sensitivity as compared to TD-OCT.
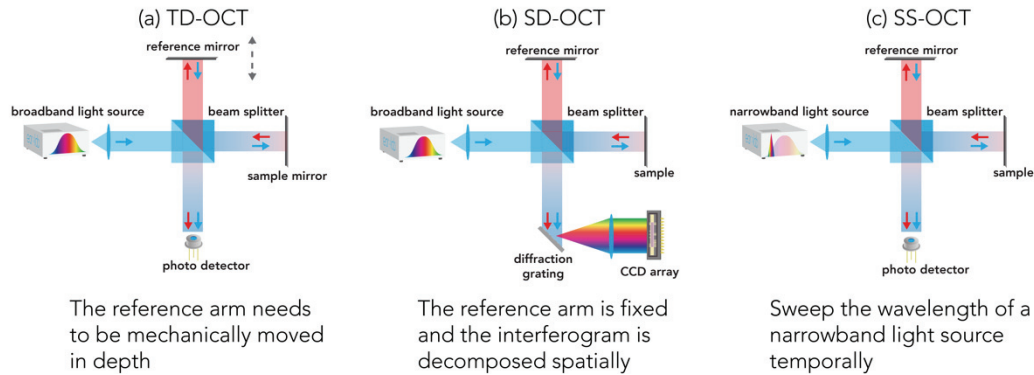
Figure 2.7: Technical implementation of OCT technologies: TD (time domain)-OCT, SD (spectral-domain)-OCT and SS (swept-source) -OCT.

Two Fourier-domain architectures have been developed: spectral-domain OCT (SD-OCT) and swept-source OCT (SS-OCT) [95]. SD-OCT employs the same broadband light source as TD-OCT. However, instead of using a single detector to capture the entire A-scan, the spectrum of the interfered light is spatially separated with a diffraction grating[a] and then sampled with a high-speed line camera. SD-OCT simultaneously illuminates and detects all the spectral channels. As a result, the signal-to-noise ratio (SNR) is improved in comparison to TD-OCT[b] [80], [96]. In SD-OCT, the number of resolvable wavelengths determines the maximum scan range (i.e., sensitivity roll-off in depth), which is mostly dependent on the number of pixels available in the spectrometer (e.g., 512 or 4096 [82]).

Instead of spatially decomposing a broadband source with a diffraction gating, an alternative that achieves a similar effect is to temporally sweep the wavelength of a narrowband source, a technique called swept source OCT (SS-OCT). SS-OCT utilises a wavelength-tunable laser to rapidly sweep through a range of wavelengths which allows the spectrum of the interferometer output to be sequentially recorded using a single

---

[a] A diffraction grating is an optical component with evenly spaced grooves that diffracts incoming light into its component wavelengths [85], [98].

[b] In an ideal setting where both FD-OCT and TD-OCT operate within the shot noise regime and have same scanning depths, with each spectral channel of the OCT systems receiving equal optical power, the SNR advantages of FD-OCT over TD-OCT become evident that FD-OCT illuminates all depths of the sample simultaneously, allowing the coherent integration of optical power across spectral channels, while permitting the incoherent integration of noise variances. A detailed discussion of FD-OCT SNR for both SD-OCT can SS-OCT can be found in [82], [85], [92].

photodetector [96], [99].The interferogram obtained from SS-OCT contains a range of frequencies that correspond to different depths within the tissue being imaged.

Compared to SD-OCT, SS-OCT exhibits reduced detection losses owing to the higher detection efficiency of photodetectors as compared to CCDs [80], [82]. SS-OCT also make it possible to use balanced detection to remove common-mode interference much more easily than SD-OCT. Furthermore, SS-OCT offers additional benefits: the narrow linewidth permits a deeper scan range, the wider bandwidth enables higher axial resolution, sweep rates can be engineered to be significantly higher than the scan rates of line scan cameras, and the higher output power enables an improved sensitivity.

2.4.3   Signal and artefacts in FD-OCT

Although the two techniques differ in their respective technical implementations, the detection of the diffraction spectrum is equivalent to the measurement of a wavelength-swept interferogram from the perspective of signal processing. Whether the decomposition of the spectrum into its spectral components is achieved spatially or temporally, the measured spectral interferogram signal $I(k)$ is given by [97], [100], [101]:

$$I(k) = G(k) \left\langle \left| E_r(k) + \int_{-\infty}^{\infty} \alpha(z) e^{i2k\hat{n}z} dz \right|^2 \right\rangle \tag{2.4}$$

$$
\begin{aligned}
I(k) = G(k) \Bigg\langle |E_r(k)|^2 &+ 2\Re\left\{ E_r^*(k) \int_{-\infty}^{\infty} \alpha(z) e^{i2k\hat{n}z} dz \right\} \\
&+ \left| \int_{-\infty}^{\infty} \alpha(z) e^{i2k\hat{n}z} dz \right|^2 \Bigg\rangle
\end{aligned}
\tag{2.5}
$$

$G(k)$ is the normalised source spectral intensity distribution where $\int G(k)\, dk = P_o$ and P_o is the source output power. $\alpha(z)$ is the complex scattering amplitude of the sample as a function of path length difference z, encoding the phase as well as the amplitude of each reflection. $k = 2\pi/\lambda$ is the wavenumber, and $\hat{n}$ is the complex refractive index where $\hat{n} = n + i\alpha$ includes both refraction and losses [82], [100]. A more detailed derivation of (2.4) and (2.5) can be found in Appendix A.

DC term

The first term inside the bracket on the right-hand side of (2.5), is the DC component of the signal, shown in Figure 2.8. This term is independent of the sample reflectivity [82] and it is typically the largest signal component in FD-OCT. If not removed, it can lead to a significant signal distortion centred at zero path length difference. In TD-OCT, the DC component can be easily removed with a high pass filter [82], as it does not modulate with the sample.

In FD-OCT, removal of the DC component is usually achieved by either subtracting a recorded interferogram in the absence of the sample from each subsequent acquired interferogram [82] or, for SS-OCT, by employing a balanced detection scheme [82], [102], [103] – using an optical circulator and a 50:50 optical coupler to create two interference signals, differing by a phase shift of π, where a differential signal can be obtained from the outputs from a pair of detectors by subtracting one from another. This cancels out the contribution from the DC component and relative intensity noise (RIN) present in the acquisition [103].

Cross-correlation term

The cross-correlation term, the second term in (2.5), in the interferogram signal is influenced by both the light source wavenumber k and the relative path length difference between the reference arm and the sample reflectors [101]. As this term encodes the complex scattering amplitude of the sample, it is the signal of interest.

Auto-correlation term

The last term in (2.5) is the autocorrelation term. It arises from the interference between the light reflected from different layers within the same sample, and its amplitude is generally much smaller in comparison to the cross-correlation term. However, even though the autocorrelation term is comparably smaller, it can still contribute to artefacts in the reconstructed image near the location of the path length difference if not properly accounted for, as the distance between reflectors within a sample is typically much smaller than the distance between the sample reflectors and the reference arm path length. Assuming the auto-correlation term is significantly smaller compared with the cross-

correlation term, it is possible to minimise its impact by choosing an appropriate display range [104] or by using balanced detection [96], [103].
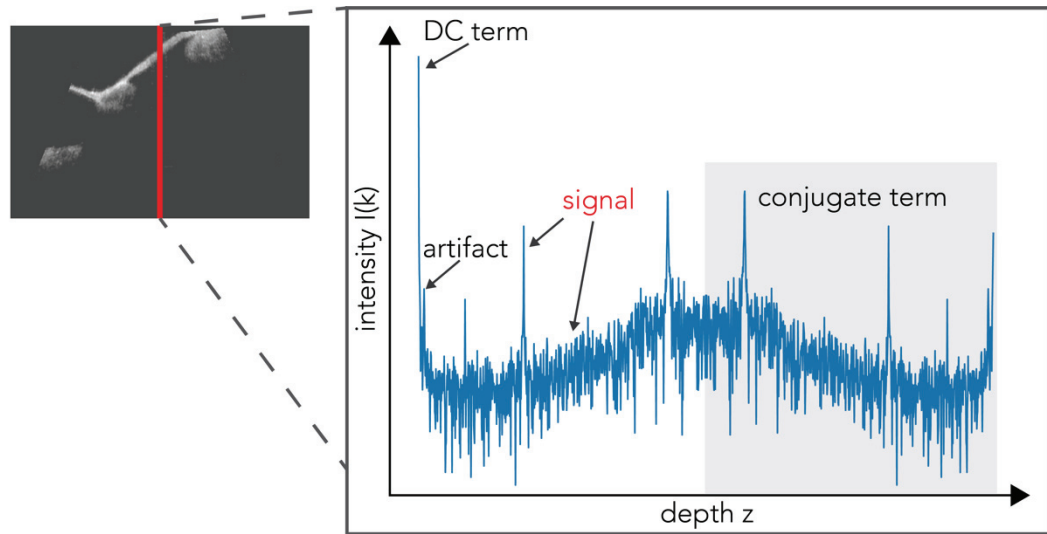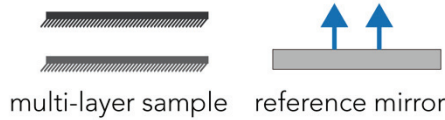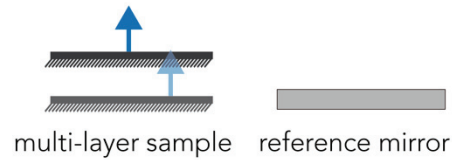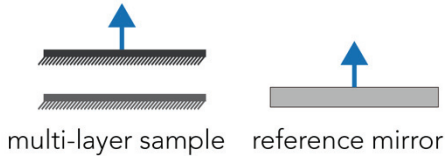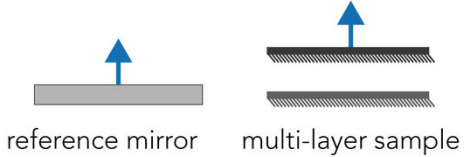
Figure 2.8: Visual representations of signal components in FD-OCT A-line.

For the sake of clarity and simplicity, we formulate the measured spectral interferogram signal $I(k)$ by substituting $\hat{n} = n$, $2E_r(k) = 1$ as well as neglecting the constant and auto-correlation terms as they can be effectively managed through either filtering or balanced detection in a well-design system so as to leave only the second term

containing the scattering amplitude. The measured OCT spectral interferogram signal $I(k)$ [100], [101] can be obtained by using the Euler's rule[a] :

$$I(k) = G(k)\left(\int_{-\infty}^{\infty} \alpha(z)\cos(2knz)\,dz\right) \tag{2.6}$$

The complex A-line $s(z)$ is usually calculated via inverse discrete Fourier transformation (IDFT),

$$s(z) = F^{-1}\{I(k)\} = F^{-1}\{G(k)\} * \alpha(z) \tag{2.7}$$

where the $*$ operator denotes convolution. We can interpret the factor $F^{-1}\{G(k)\}$ as an axial point spread function (PSF) $d(z)$ that blurs out the response from a point scattering target in the A-line signal. Since source spectral imperfections can affect both magnitude and phase, $d(z)$ is generally a complex function of depth given by

$$d(z) = F^{-1}\{G(k)\} \tag{2.8}$$

so that the A-line signal $s(z)$ has a convolutional structure given by:

$$s(z) = F^{-1}\{I(k)\} = d(z) * \alpha(z) \tag{2.9}$$

Complex conjugate term

In FD-OCT, besides the signal components in the previous section, there is an artefact known as the complex conjugate term [80], [105], which reduces the effective OCT imaging depth by half. This artefact arises because the collected interferometric spectrum is real-valued, and its inverse Fourier transform (IFT) must be Hermitian symmetric[b]. The complex conjugate artefact in FD-OCT limits the imaging depth and creates ambiguity in distinguishing signals reflected from negative path lengths (beneath the zero delay) from those reflected from positive path lengths (above the zero delay) as depicted in Figure 2.8 [82].

A widely used approach in most FD-OCT systems is to ensure that the region of interest (ROI) in the sample lies exclusively on one side of the zero-path length position and to crop out duplicate data on the other side of the zero position [82], [106]. Although

---

[a] $e^{ix} = \cos(x) + i \cdot \sin(x)$ [3].
[b] Given a real-valued function $x[n]$ to and its Fourier transform $X(e^{jw})$ that $X(e^{jw}) = X^*(e^{-jw})$ [3].

this method is simple, it is not very efficient as it results in the discarding of half of the imaging range.

Wavenumber resampling

In FD-OCT, the reflectivity profile in the axial direction is encoded with optical frequency or wavenumber, k. If spectral information is not collected at evenly spaced wavenumbers, then it must be resampled onto a grid of evenly spaced wavenumbers before the inverse Fourier transform can be performed [82], [100]. In practice, the interference signal $I(k)$ is not acquired in k directly, but rather is obtained through an intermediate coordinate, time in SS-OCT or space in SD-OCT. Resampling the spectrum involves interpolating the spectral data to obtain uniformly spaced wavenumber k [82].

Specifically, in SD-OCT, the spectrometer generates an interference spectrum that is a function of wavelength instead of wavenumber. Nonlinearity can arise between the linear mapping of the interference spectrum from wavelength to wavenumber due to several sources, including dispersion of the diffraction grating, misalignment of the CCD, finite CCD pixel sizes, or surface imperfections of the optics [82].

SS-OCT systems use a tunable laser and a photodetector to acquire the optical signal, which is then digitised by an analog-to-digital converter (ADC) at constant time intervals [82], [105]. Although for some swept source lasers, the nonlinear tuning of the laser in k space might require the ADC to be sampled with nonuniform time intervals so as to construct evenly spaced interference signal $I(k)$ to minimise nonlinearity [99].

In addition, some system requires an external optical clock to control the laser for acquisitions and triggering the digitisation of the interference signal [99]. The external clock is typically generated by a highly stable reference oscillator to ensure that the laser wavelength is accurately controlled and stable during the acquisition process [82]. Any mismatch between the clock and interference signal timing is caused by either synchronisation issues or propagation delays [82], which can be optical – the time it takes for the light signal to travel from the sample to the detector or electronic – the time it takes for the electronic signal to propagate through the circuitry.

Collectively, those optical and electronic propagation delays can result in errors in the sampling process, causing distortion in interference signals. For example, if the clock

signal is faster than the interference signal, the ADC will sample the same interference signal multiple times, leading to over-sampling. Conversely, if the clock signal is slower than the interference signal, the ADC may miss some interference signals, resulting in under-sampling [82]. Nonlinearities resulting from interference signal distortions can degrade axial resolution if left uncorrected [99], [107].

Sidelobe artefacts

The purpose of OCT, as with any other biomedical imaging technique, is to extract diagnostically useful information from acquired images and a primary goal of OCT image processing is to obtain an accurate estimate of the scattering amplitudes $\alpha(z)$ from the measured $s(z)$ in (2.9). Conventionally, $s(z)$ is taken as the estimator of $\alpha(z)$ which is an effective approximation as long as the PSF is spatially localised (i.e., it approximates a delta function) as shown in Figure 2.9 (b).
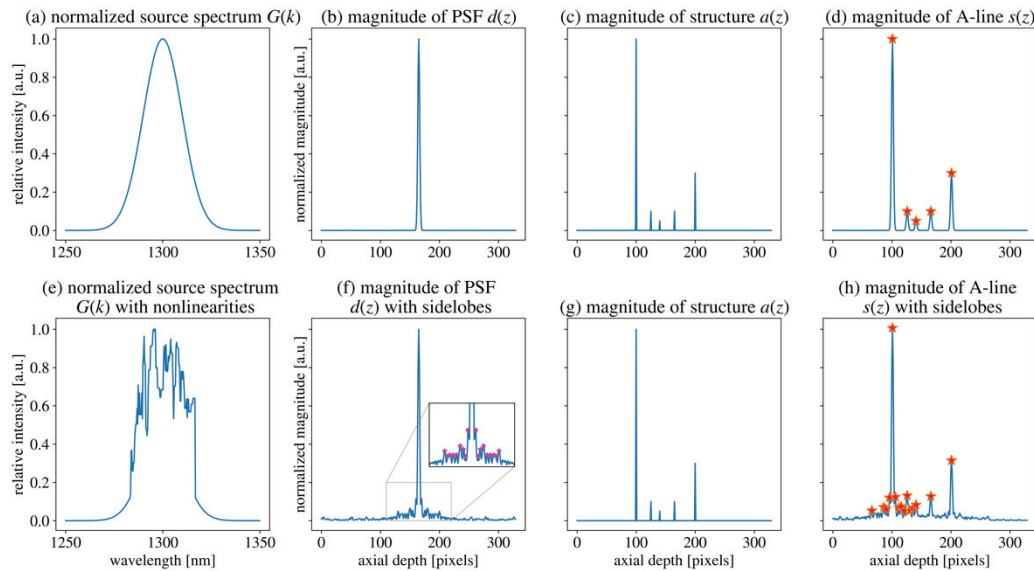
Figure 2.9. OCT A-line formation and effect of nonlinearity in the spectrum with two scenarios where the top (i.e., from (a)-(d)) is the ideal case that source spectrum $G(k)$ has a perfect Gaussian shape whereas the bottom (i.e., from (e)-(h)) shows when the source spectrum deviates from a Gaussian shape and introduces sidelobe near the main peak.

However, in practice, OCT axial PSFs are not perfectly localised as the source spectrum deviates from a Gaussian shape. Rather the PSF typically has sidelobes (i.e., Figure 2.9(f)) near the central peak caused by non-uniformity of the light source spectrum and/or imperfect linearity in spatial frequency of the swept light source in swept source

OCT or detector system in spectral domain OCT [108]. In well-designed OCT systems, sidelobes can be 40 dB [82] or more lower than the main PSF peak, but when there is a bright reflector on a given line, the PSF sidelobes can rise above the noise floor and appear as artefacts extending from the reflector in the depth direction [82], [97], [109].

These sidelobes artefacts can obscure structures of diagnostic interest and limit contrast and degrade image quality. Figure 2.9 illustrates OCT A-line formation and the sidelobe effect with a simplified simulation that only considers the magnitude of $d(z)$, $\alpha(z)$, and $s(z)$ as defined in (2.9). Each reflector in the A-line appears broadened or blurred out to a width of about a coherence length by convolution with the axial PSFs. One dimensional (1D) convolution[a] can be seen as making weighted and shifted copies of the axial PSF at the location of each reflector. The quality (i.e., degree of deviation from ideal Gaussian shape) of the axial PSF provides a measure of the fundamental limitations on the quality of image possible with a given OCT system and it is entirely dependent on the optical source.

To be more specific, A narrower PSF results in higher axial resolution, which means that the system can better distinguish two nearby reflectors. On the other hand, a broader PSF or PSF with sufficiently large sidelobes leads to lower axial resolution and reduces the ability of the system to distinguish closely spaced structures [111]–[113] as demonstrated in Figure 2.9(d) and (h) where sidelobes arise from the noise floor and introduce spurious structures [82], [111].

2.5   Light sources in FD-OCT

Since the axial PSF is primarily determined by the spectral shape of the employed optical source, it is helpful to provide a brief discussion of the light sources used in FD-OCT. In FD-OCT, the light sources used are typically either superluminescent diodes (SLEDs) in SD-OCT [103] or tunable lasers in SS-OCT [106], [114].

SLEDs are semiconductor-based light sources that use a waveguide structure to generate broadband output at high power through spontaneous emission with a single-

---

[a] $s[n] = d[n] * \alpha[n] = \sum_{k=-\infty}^{\infty} d[k] \cdot \alpha[n-k]$ where $\alpha[n]$ here is the input function, $d[n]$ is the convolutional kernel and we obtain output $s[n]$ by multiplying the terms of $d[n]$ with the terms of shifted $\alpha[n]$ and then sum them up [110].

pass amplification [82], [115]. In comparison, tunable lasers or light amplification by stimulated emission of radiation (LASER or commonly known as laser), operates based on the principle of stimulated emission to output light with a narrow spectral width [82].

The wavelength tunability of swept lasers is achieved by modifying the properties of the gain medium or cavity structure to produce a variable output wavelength over a range. The specific tuning mechanism for the laser output depends on the type of swept laser [82], [107]. For example, distributed Bragg reflector (DBR) lasers use a grating structure within the cavity to reflect light back into the cavity, allowing a tunable single mode emission by changing the refractive index of the cavity and selectively amplifying light at a specific wavelength [99], [107].

2.5.1   Fundamentals of light emission

The following illustration (i.e., Figure 2.10) offers a simplified depiction of the key phenomena outlining the operating principles of lasers and Superluminescent Light Emitting Diodes (SLEDs).

Absorption

Absorption occurs when an electron transitions from a ground state with lower energy level to a higher energy level and this process takes place only if, the photon possesses the precise energy need for the transition [115], [116]

Spontaneous emission

In spontaneous emission an electron at a higher energy level spontaneously decays to the ground state, releasing a photon that carries energy equal to the difference between the excited and ground energy levels [115], [116].

Stimulated emission

In stimulated emission, an incoming photon with a specific frequency interacts with an electron that resides at the excited state, resulting in emission of a new photon. This newly emitted photon is identical to the original photon in terms of wavelength, phase, and polarisation. Stimulated emission is therefore a form of light amplification.
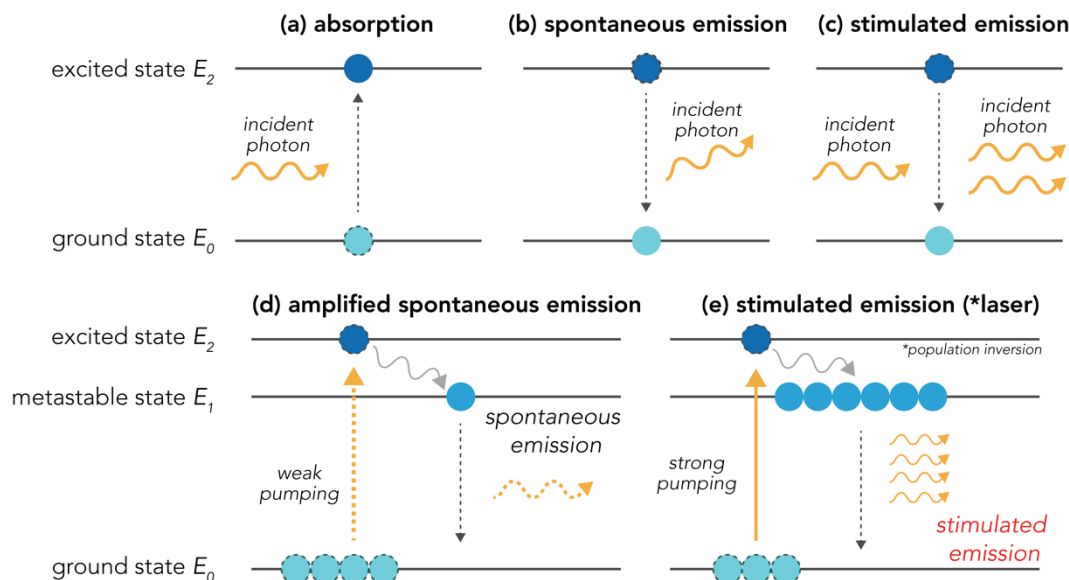
Figure 2.10: The interactions between electrons and photons that are important to the understanding of laser and SLEDs operating principle. Electrons reside in discrete energy states [115], [116]. These energy levels represent the permissible values of an electron's energy, with electrons being restricted to energy levels within an atom. As an electron absorbs or releases energy, it undergoes a transition between these levels, resulting in the emission or absorption of electromagnetic radiation at specific frequencies [115], [116].

Population inversion

Under normal conditions, the statistical distribution of electrons is such that the majority are in the ground state with only a small percentage in the excited state. To achieve stimulated emission, a material must be in a state of population inversion in which there are more electrons in the excited state electrons than in the ground state. This situation can be achieved by electrically or optically pumping electrons into an excited state with a slow rate of spontaneous emission [82], [115].

2.5.2   Operation principle of semiconductor SLEDs and swept source laser

The basic structures of semiconductor SLEDs and lasers share similarities [115], that both structures consist of an active layer serving as a waveguide, sandwiched between P- and N-type cladding layers, and have a voltage applied across the P-N junction through electrodes. When a forward bias voltage is applied, the depletion region between the P- and N-type layers narrows, causing injected electrons to populate the conduction band (i.e., excited state), while holes are created in the valence band (i.e., ground state), and with recombination of hole and electron pairs taking place in the depletion region. The

recombination process results in light emission, with SLEDs designed to output light with a broadband spectrum and lasers designed to produce monochromatic and coherent light.
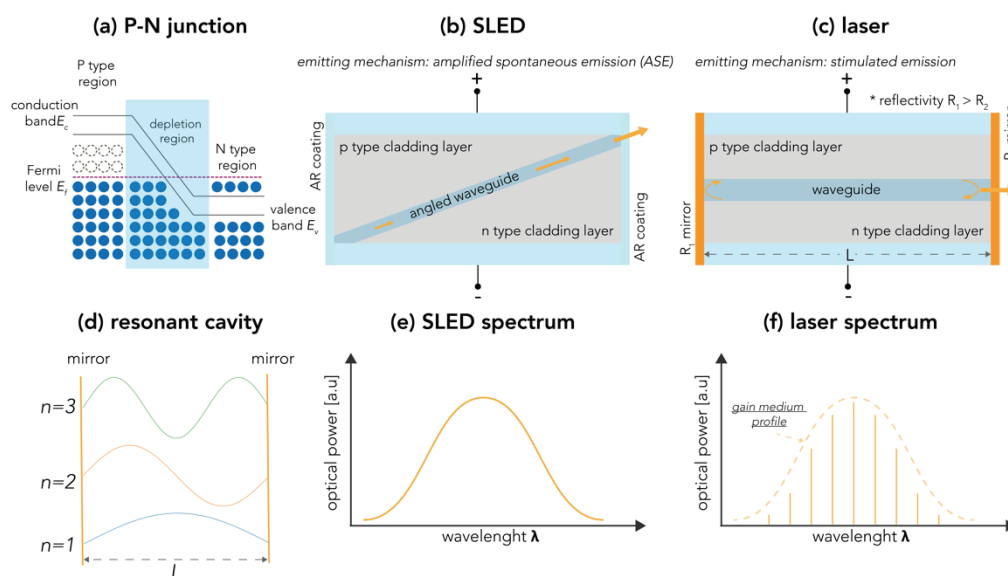
Figure 2.11: Schematics and spectrum profiles of semiconductor SLEDs and edge emitting laser. The waveguide is surrounded by materials with a lower refractive index, the emitted light is naturally guided through the process of total internal reflection which eliminates the need for additional confinement techniques to guide the light within the waveguide. SLED: When a forward bias is applied across the P-N junction, spontaneous emission experiences amplification via stimulated emission. Optimised geometries such as tilting the waveguide with respect to the end facets further suppresses backreflected light. Laser: When a forward bias is applied to the gain medium and sufficient pumping is achieved, the gain medium reaches a population inversion [82], making lasing possible via stimulated emission.

SLEDs

SLEDs are designed to enable a single-pass amplified spontaneous emission (ASE) generated along the waveguide [116], [117]. To prevent optical feedback in SLEDs, both waveguide ends are coated with an anti-reflective (AR) layer [115], [116]. In practice, achieving zero reflection from the facets of the waveguide in a SLED is nearly impossible due to the high reflection coefficient of the cleaved semiconductor facets as well as the minor lot-to-lot variance in the semiconductor structures [117]. These residual reflections inevitably cause parasitic Fabry-Perot modulation[a], commonly referred to as

---

[a] Change in the phase of the light as the distance between mirrors varies [115].

spectral ripple [117]. In the presence of spectral ripple, the output spectrum of a SLED deviates from its ideal Gaussian shape, which ultimately gives rise to sidelobes in the axial PSF as demonstrated in Figure 2.9.

Swept source laser

In general, a swept source laser consists of three key components: a gain medium, a resonator cavity, and a narrowband tunable wavelength selection filter [82], [105], [107]. The gain medium plays a crucial role in providing optical amplification in swept-source lasers. A commonly used gain medium is the semiconductor optical amplifier (SOA) due to its advantageous properties, such as a short gain response time, high gain, and broad bandwidth [82].

When a forward bias is applied to the gain medium and sufficient pumping is achieved, the gain medium reaches a population inversion [82]. This means that there are more electrons in a higher energy state than in a lower energy state, creating a favourable condition for stimulated emission where injected electrons from the conduction band combine with holes in valence band. In an edge-emitting laser configuration [107], a linear resonator cavity is formed by two mirrors and a gain medium. One of the mirrors is totally reflective while the other is partially reflective. The mirrors are arranged to form a Fabry-Perot resonator where light reciprocates in the waveguide and forms standing waves [115]. When the amplitude of the standing waves exceeds a certain threshold because of the repeated roundtrip amplification, light is emitted from the partially reflective mirror.

Those standing wave are referred as the longitudinal modes [82], [118], which are the allowed discrete wavelengths of light that can exist along the optical axis of the cavity. These modes correspond to standing waves that are aligned with the optical axis and have a well-defined wavelength and frequency [82]:

$$\frac{m\lambda}{2} = nL \tag{2.10}$$

where m is the longitudinal mode index integer, λ is the free-space wavelength, n is the effective index of the waveguide, and L is the cavity length. The free spectral range (FSR) represents the frequency or wavelength interval between two consecutive longitudinal modes [116]:

$$FSR = \frac{c}{2nL} \tag{2.11}$$

where c is the speed of light. As shown by (2.11), the FSR in an optical resonator is inversely proportional to the cavity length L. That is, shorter cavities have larger FSR. In some cases, mode-hopping can occur when the laser experiences an instantaneous transition between different longitudinal modes [99], [119], [120]. This can be caused by factors such as mechanical vibrations or changes in temperature, which alter the cavity length or the refractive index of the gain medium [82], [99], [120]. This sudden jump in wavelength due to mode-hopping can lead to an increase in laser noise as well as the presence of sidelobes in the axial PSFs.

In other words, in order for a laser to emit at a desired wavelength, that wavelength must coincide with a longitudinal mode present inside the optical cavity for which the gain is large enough to provide adequate amplification [82]. Moreover, since every resonator will have some loss at the mirrors as 100% reflectivity is impossible to achieve in reality [82], the output wavelengths are not perfect delta functions. Instead, they have a certain linewidth or broadening dependent on the reflectivity of the mirrors [115].

In addition to longitudinal modes, the cavity can also support transverse modes, (e.g., micro-electromechanical systems tunable vertical cavity surface-emitting lasers or MEMS-VCSELs) [118], which are the various spatial patterns light waves can take within that cavity, perpendicular to the axis of propagation [115]. In the case of MEMS-VCSELs, the presence of sidelobes in the axial PSFs can be attributed to two factors: the unwanted higher-order transverse modes and parasitic reflections within the laser cavity [118].

An ideal swept-source laser for OCT should maintain a perfectly linear sweep in terms of frequency as exemplified in Figure 2.12 (a) (or equivalently, a linear sweep in terms of wavenumber) while operating at a high sweep rate [82], [99], [105]. Achieving linearity in the sweep ensures that the acquired OCT data can be directly processed without the need for additional calibration or resampling steps [82], [105]. The tuning range of a swept-source laser system refers to the difference between the start and end wavelengths, as shown by the Gaussian spectral envelope in in Figure 2.12 (b). The tuning range is a crucial factor that determines the performance of swept source OCT as

indicated by (2.2) that the axial resolution is inversely proportional to the tuning range of the laser.

On the other hand, a high sweep rate (i.e., reciprocal of the sweep period), is essential for real-time acquisition of large volumetric datasets, reducing motion artefact susceptibility, and imaging dynamically varying physiological processes [8], [82]. The sweep rate determines the A-line acquisition rate and most clinical application require a sweep rate of 20 kHz or greater [4], [82]. Moreover, in SS-OCT, the maximum ranging depth z_{max} relates to the tuning range and sweep rate such that $\delta\lambda = \frac{\Delta\lambda}{N_s}$ and $N_s = \frac{f_s}{f_{sweep}}$ where f_s is the rate at which the interferogram is sampled and f_{sweep} is the sweep rate, [82], [107]:

$$z_{max} = \frac{\lambda_o^2}{4n\delta\lambda} = \frac{\lambda_o^2 f_s}{4n\Delta\lambda f_{sweep}} \qquad (2.12)$$

that n is the group refractive index of the sample, the instantaneous linewidth ($\delta\lambda$), shown in Figure 2.12 (d), characterises the swept laser's average coherence length [107]. It represents the linewidth of the laser output at any given instant during the sweep. N_s is the sample within the tuning range of the spectrum where it can be calculated as the ratio of the sampling rate of the ADC and A-line sweep rate [106], [114]. It can be noted from (2.12), increasing the sweep rate effectively reduces the maximum ranging depth in kinetic swept lasers.

The tunable wavelength selection filter in swept-source lasers can be achieved through various methods [82], [99], [107]. One such method involves using a diffraction grating, which can be either stationary or tuned with MEMS-based actuation, in conjunction with a polygonal mirror assembly. This setup selectively feeds back a specific wavelength based on the angular position of the mirror, providing the required tunable wavelength selection [82]. Another commonly employed method involves adjusting the cavity length of a Fabry-Perot tunable etalon, as indicated in (2.11), using a piezoelectric actuator. By applying voltage to the piezoelectric actuator, the etalon cavity length can be precisely controlled, enabling the selection of different wavelengths [82].

(a) tuning curve

tuning range

time t

wavelenght λ (vertical axis)

(b) output spectrum

optical power [a.u] (vertical axis)

tuning spectrum

instantaneous spectrum

wavelenght λ

(c) time trace

sweep period

wavenumber k (vertical axis)

decelerate → stop ← accelerate

← accelerate   decelerate → stop ← accelerate

time t

(d) magnitude of axial PSF

relative intensity [a.u] (vertical axis)

axial depth [pixels]

Figure 2.12: Example of mechanically tuned swept source laser output properties.

While adjusting the mechanical movement of the wavelength selection filter has been the basis for most swept lasers, in practice, kinetic lasers often face challenges concerning sweep linearity and efficiency [107], [119], [121]. These challenges stem from the need to create and deplete momentum, which is inherent to the mechanical nature of the tuning process. To be more specific, in a mechanically-tuned swept laser, the tuning mechanism involves physically moving a mirror or grating to vary the wavelength of the laser output [99], [119], [121]. This multi-stage stages process, illustrated in Figure 2.12 (c), includes initiation of movement, acceleration, maintenance of a constant tuning rate (i.e., the green shaded portion in Figure 2.12 (c)), deceleration, and stopping [82], [99], [107]. During the acceleration and deceleration phases, the tuning mechanism must build up momentum and then slow down to a stop. This accelerate-decelerate cycle can be optimised, but not eliminated [82], which can limit the linearity of the wavelength sweep and reduce the efficiency of the kinetic swept lasers.

In swept-source lasers that utilise kinetic tuning, the adjustment of cavity length is achieved either mechanically or electrically [82], [107], often leading to a relatively extended cavity length. This increased cavity length can pose challenges for attaining single longitudinal mode operation [99], [119] due to the increased likelihood of coherence revival. Coherence revival occurs when multiple longitudinal modes oscillate

simultaneously within the laser cavity, as FSR diminishes in response to the elongated cavity length as indicted in (2.11) [99], [107], [119]. Moreover, as the cavity length expands, the buildup time for individual modes also experiences an increase [82]. In situations where the sweep rate increase, lasing may not experience sufficient time to build up anew from spontaneous emission to stimulated emission at each successive wavelength [82]. Furthermore, the resulting extended cavity lengths are susceptible to mechanical vibrations [82], [119], [121].

As kinetic lasers generally cannot achieve frequency versus time sweep linearity, they require an external k-clock for resampling or triggering [82]. The external k-clock can be generated with an interferometer by setting the path length difference to match the desired sampling frequency [119], [122]. Consequently, the interferogram can be uniformly sampled at each zero crossing point of the sinusoidal k-clock signal [82], [122]. However, employing an external optical k clock can introduce nonlinearities during sweep, which can be largely attributed to synchronisation errors between the sweep start and the k-clock [82], [119], [121] or the intrinsic timing jitter noise of the ADC [82], [105]. The latter represents the inherent fluctuations in the timing of the conversion process within the ADC [82], [105], [122]. Furthermore, kinetic lasers are susceptible to mechanical wear and mechanical changes with time and temperature, which could lead to amplitude variation in the output power and create sidelobe artefacts.

In summary, sidelobe artefacts arise from spectral non-uniformity and/or spectral non-linearity in the OCT light source. Key contributors to nonlinearity in the spectrogram, which result in sidelobes in axial PSFs, include inaccuracies in k-space sampling, synchronisation errors between the k-clock signal and interference signal triggering, parasitic Fabry-Perot modulation causing spectral ripples in SLEDs, nonlinear sweeping behavior of k, mode hopping, coherence revival in kinetic swept lasers, and the presence of high-order transverse modes in VCSELs.

2.6   Middle ear optical coherence tomography (ME-OCT)

Optical coherence tomography (OCT) has emerged as a significant advancement in otology and auditory physiology, offering complementary information for clinical decision-making in the examination of the tympanic membrane (TM), ossicular chain,

and inner ear. This non-invasive, depth-resolved imaging technique for hearing diagnostics has many advantages over traditional otoscopes and surgical microscopes, which are the primary tools for otologic point of care imaging.

Pitris et al. first demonstrated the potential of OCT imaging for the TM and middle ear in 2001[3]. However, widespread interest in OCT technology for otology research and clinical applications took nearly a decade to develop due to technological limitations [2], [8]. The introduction of swept-source OCT (SS-OCT) in the 2010s, featuring akinetic all-semiconductor lasers and other highly phase-stable systems, made real-time in-vivo middle ear OCT clinically viable [106], [114], [123].
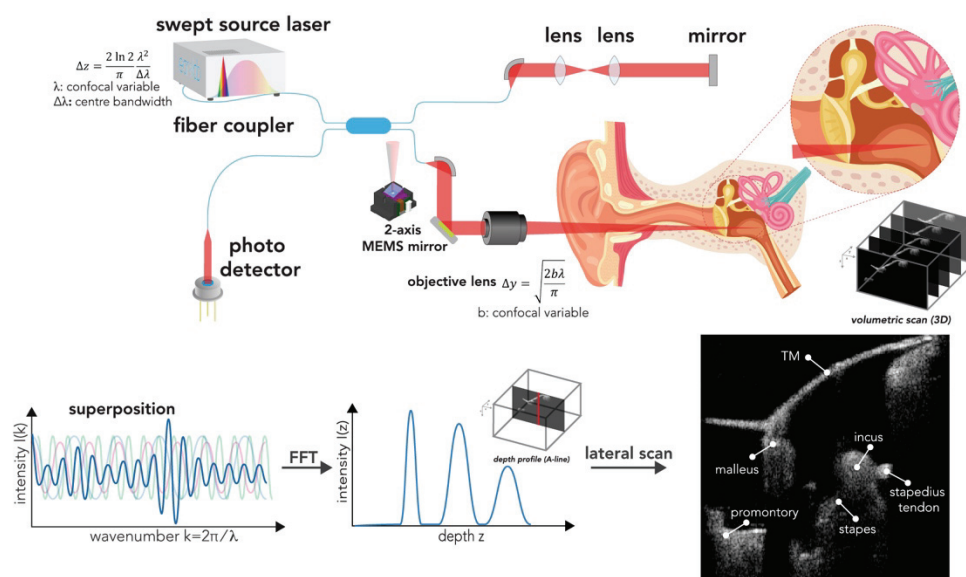
Figure 2.13: Middle ear imaging with SS-OCT. In the cross-sectional view of the middle ear, anatomical structures such as the tympanic membrane (TM), malleus, promontory, stapes, incus, and stapedius tendon are visible.

ME-OCT has since been applied to various clinical applications, such as detecting cholesteatomas [54], guiding ear surgery [124], measuring TM thickness [14], grading otitis media [125]–[127], evaluating tympanoplasty success [58], and discriminating presumptive otosclerosis from healthy controls [1]. Notably, OCT has shown potential to improve otitis media (OM) diagnosis by detecting biofilm presence behind the TM, resulting in higher diagnostic sensitivity (83% vs. 74%) and specificity (98% vs. 60%) compared to standard otoscopy [125]. In a study conducted with a pediatric population [128], OCT showed compelling diagnostic accuracy in detecting effusion in the middle

ear space, exhibiting high diagnostic accuracy of 90.6%, sensitivity of 90.9%, and specificity of 90.2%. This improvement has the potential to optimise clinical workflow in comparison to traditional methods, such as pneumatic otoscopy, which often necessitates sealing the ear canal [128].

To accelerate the clinical adoption of OCT in otology, several form factors have been explored to address the diverse clinical needs. For example, integrating OCT with surgical microscopes [16], [17], [129] has enabled detection of microanatomic changes in TM layers [106] and differentiation of keratin from normal or inflamed middle ear mucosa. Handheld OCT probes [18], [130], [131], resembling otoscopes [1], [9] or endoscopes [14], [58], [132], have demonstrated their ability to detect biofilm behind the TM [125], [125], [133] and to identify ossicular fixations [1].

In addition to structural imaging, OCT can also evaluate middle ear status by detecting micro-movements of the TM, ossicles, and foreign objects (e.g., prostheses [106] or retained surgical items [134]) when present, in response to pure tone sound stimuli with Doppler vibrometry. In particular, OCT-DV can distinguish otosclerotic ears from normal ears in vivo through an intact TM, achieving 100% sensitivity and 98% specificity respectively, based on measurements obtained at the lenticular process of the incus with a 500 Hz stimulation frequency [1].
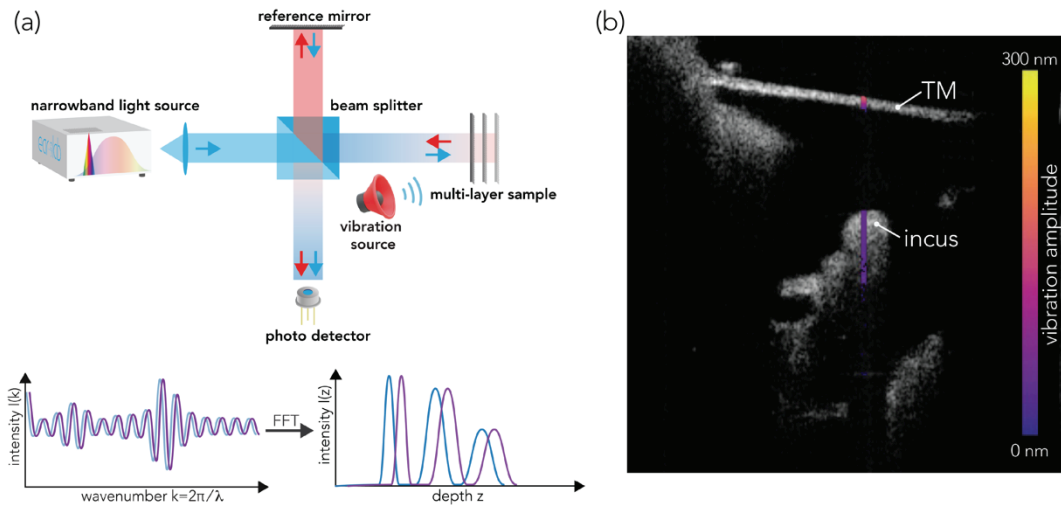
Figure 2.14: Principle and application OCT-DV for middle ear vibrometry. Vibrational information is overlaid on top of a structural image of the middle ear. During ME-OCT measurements, an acoustic stimulus with a much lower frequency than the laser sweep is generated, causing periodic motion of the structure of interest and introducing a Doppler shift in the measurements [17], [106]. This Doppler shift appears as an optical phase shift, modulated at the acoustic stimulus's frequency, between A-lines acquired sequentially in time [1], [57], [75], [106] as illustrated above. The resulting optical phase shift represents a frequency-resolved vibration signature that can be extracted by first calculating the phase difference of sequential A-lines and then taking the Fourier transform (FT) across those phase differences at each depth [17], [106]. This approach allows for obtaining velocity information directly with high accuracy and avoids motion noise during acquisition.

ME-OCT enables structural and functional analysis of the middle ear space through the TM, providing high resolution vibrometry information that cannot be obtained from standard auditory testing [17], [106]. Recent studies have highlighted the advantages of OCT both independently and as a complement to current otology diagnostic tools [2], [135]. Its various applications, such as stapes fixation detection [1], otitis media evaluation [126], antibiotic treatment monitoring [133], and effusion classification [128], [136], could help bridge the gap between the limitations of existing clinical diagnostic tools and the need for more accurate and precise diagnoses [2], [8].

2.6.1 ME-OCT with akinetic swept laser source

The growing interest in examining the middle ear using OCT has led to the development of various systems [1], [14], [123], [133], [136], [137]. This thesis focuses on the ME-OCT system developed in our lab [130], [131], [135], which utilises an SS-OCT architecture to acquire phase-stable interferograms at a high sweep rate (~200 kHz) —

crucial for in-vivo structural and functional exploration and interrogation of the middle ear space.

This handheld swept-source OCT system is designed to resemble an otoscope and can produce real-time, high-resolution transcanal, transtympanic images of the middle ear (ME) with excellent soft-tissue contrast at the point of care, without exposing patients to radiation. A key component of this ME-OCT is a Vernier-tuned distributed Bragg-reflector (VT-DBR) akinetic swept-source laser (Insight Photonics Solutions, Model: SLE-101 [99]). This laser has a center wavelength of 1550 nm, a sweep range of 35.4 nm[a], and a nominal sweep rate of 200 kHz, allowing it to achieve axial and lateral resolutions in air of 40 μm [135]. With a scan range limited to 10.9 mm [135], the system effectively images the entire depth of the human middle ear, from the most lateral aspects of the TM to the most medial visible parts of the cochlear promontory (CP).

2.6.2 Akinetic all-semiconductor programmable swept-source

The Vernier-Tuned Distributed Bragg Reflector (VT-DBR) laser is a monolithically-constructed, akinetic swept-source laser that offers substantial performance improvements in sweep linearity and phase stability compared to conventional tunable lasers that depend on mechanical tuning mechanisms [99], [107].

The VT-DBR laser operates solely through electronic tuning, which involves changing the refractive index of semiconductor materials in the laser cavity using precisely controlled and synchronised injection currents [99], [121]. This current induced change of refractive index essentially modifies the effective cavity length. For instance, (2.10) can be rearranged to illustrate the tuning process of relative wavelength $\Delta\lambda$ [119]:

$$\frac{\Delta\lambda}{\lambda} = \frac{\Delta n}{n} + \frac{\Delta L}{L} - \frac{\Delta m}{m} \tag{2.13}$$

where $\frac{\Delta n}{n}$ is tuned by the net cavity index change, $\frac{\Delta L}{L}$ is tuned by the physical length of cavity and $\frac{\Delta m}{m}$ is tuned by the changing either the refractive index or the grating angle of the tunable wavelength selection filter. The laser cavity consists of five sections as shown

---

[a] As of the time this was written [135], the sweep bandwidth has been enhanced to 35.4nm, up from the 40nm mentioned in the later chapters. This improvement was achieved through a firmware update.

in Figure 2.15 (a): two Vernier mirrors (i.e., controls $\frac{\Delta n}{n}$, $\frac{\Delta m}{m}$ and $\frac{\Delta L}{L}$), a cavity length adjustment unit (i.e., controls $\frac{\Delta L}{L}$), a gain section, and a semiconductor optical amplifier (SOA). Each section is driven by a current source, allowing for accurate control of output power and wavelength [99], [119], [121].
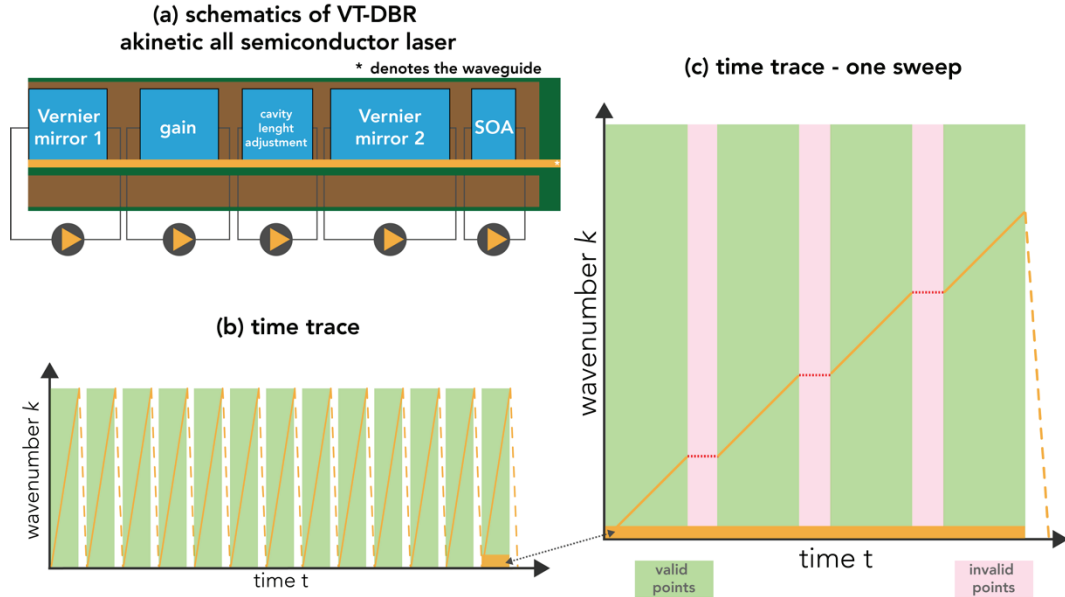
Figure 2.15: Schematics of VT-DBR and illustration of the sweep switching processing. The figure above is re-created based on the description in [99].

The control and synchronisation of the electronic currents in each section are managed by software-driven algorithms via a field-programmable gate array (FPGA) [99]. The control algorithm continuously monitors and regulates current intensities and phases to ensure the accuracy, linearity, and repeatability of each laser sweep while taking into account of the environmental factors that could alter the laser operating condition such as temperature changes and semiconductor device degradation [121].

The VT-DBR laser utilises Vernier mirrors that offer wavelength-dependent feedback [82], [107], while a cavity length adjustment unit allows real-time fine-tuning of the cavity length to ensure single-mode operation. The laser cavity features a monolithic construction with a length of approximately 2 mm [82], [99] and this compact design leads to decreased cavity variations, reduced inter- and intracavity reflections [82], and a lower likelihood of coherence revival artefacts in comparison to kinetically tunable lasers with relatively longer cavity lengths (e.g., 10 mm [82]). Owing to the multiple feedback

mechanisms and control algorithms implemented in the laser, sweep performance is optimised, ensuring mode-hop-free operation and an excellent side-mode suppression ratio (SMSR) [82], [99].

Furthermore, the VT-DBR laser exploits the Vernier effect in conjunction with a Distributed Bragg reflector (DBR) [107], [138]. Each mirror in the DBR consists of a structure made up of alternating layers of materials with different refractive indices. The refractive indices can be directly controlled with current, allowing the mirrors to reflect light at specific wavelengths [82], [138]. The slight mismatch in Bragg wavelengths between the two reflectors enables a wide wavelength tuning range while minimising the amplitude of secondary modes, resulting in stable single-mode operation [99], [119], [121]. The gain section offers the necessary amplification for lasing, and the SOA provides the final stage of output power boosting and spectral reshaping of the spectrum [82]. The single longitudinal mode operation offers a long coherence length that is beneficial for OCT applications [82], [106].

Another key aspect of the VT-DBR laser operation is the stitching process which is demonstrated in Figure 2.15 (c), as the full sweep range cannot be achieved in a single pass. Instead, the sweep is constructed by stitching together sweep sub-intervals, clocked by a 400MHz internal clock (referred as the master clock) [99]. Each sub-interval consists of valid points interspersed with transition intervals and the position of the valid points can be accessed either in real-time from the master clock signal or from a stored array generated during the calibration sequence. Furthermore, the internal electronic clock is optimised to minimise jitter noise and can be used to directly clock and trigger the data acquisition card (DAQ) without requiring an external optical clock for resampling [82], [99]. This approach not only reduces nonlinearity caused by synchronisation between DAQ and laser but also simplifies the overall system design [82], [107].

During these transition intervals, the output is not disabled, as they are necessary to update the driving current status [99], [107]. The final output spectrum of the laser is a time-sequenced ensemble of both valid and invalid wavelength values which is programmable for various sweep rates [106], [114], [119]. The stitching quality of those consecutive valid data sequences determines the linearity of the laser output spectrum and

is determined by of the calibration algorithm which can be improved through firmware updates to optimise the performance of the laser [82], [99].

Although the innovative combination of electronic tuning mechanism with multiple feedbacks, single-mode operation, reduced cavity variations, and monolithic construction of short cavity enables exceptional inter-sweep linearity and intra-sweep repeatability of the laser operation that can remain stable over extended periods. However, certain sources of nonlinearity persist in the VT-DBR laser, leading to the presence of sidelobe artefacts [99], [121]. For instance, the quality of the calibration process can be quantified by measuring the axial PSF of the laser in the setup illustrated in Figure 2.16, where a gold mirror (Thorlabs, PF10-03-M01 - Ø1" protected gold mirror) with 96% reflectivity is placed in the sample arm [139]. The high dynamic range observed in PSF measured with the akinetic laser also indicates that the fringe contrast ratio remains high throughout the tuning range, suggesting single-mode behavior. On the other hand, the presence of sidelobes indicates the presence of nonlinearity in the spectrum. This observation further corroborates the simulation performed in Figure 2.9, that sidelobe artefacts are caused by spectral non-uniformity in the OCT light source and/or spectral non-linearity, rather than the samples themselves.
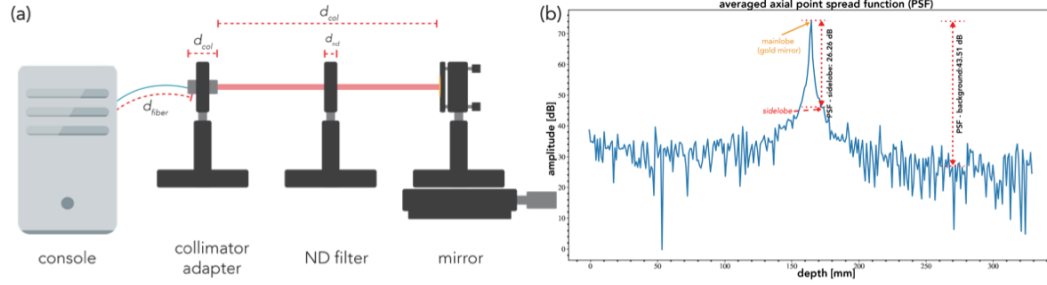
Figure 2.16: (a) Experimental setup for the PSF measurement of the described ME-OCT. The laser was coupled by a collimator (Thorlabs, model: F240 APC -1550) via a collimator adapter (Thorlabs, model: AD12), secured on an SM1-threaded kinematic mount (Thorlabs). The laser was set normal to a gold mirror (Thorlabs, PF10-03-M01 - Ø1" protected gold mirror), indicated as M. A neutral density filter (Edmund, 3.0 OD 25mm, absorptive ND filter[a]) was placed in the beam path with a slight tilt to avoid back reflection into the collimator. The mirror was secured and placed on a linear translation stage and the total optical path length was set so that the following condition could be met $2(d_{fiber} + d_{col} + d_{nd} + d_a) = d_{console}$. (b) Measured PSF in log scale the dynamic range [99] of 26.26 dB was calculated as the amplitude difference between the PSF peak amplitude relative to the nearest PSF sidelobe peak amplitude, as denoted with PSF – sidelobe [141]. Another metric, PSF – background [141] of 43.51 dB, was estimated from the difference between the peak amplitude of the PSF and the average amplitude, with the latter being calculated after excluding the peak. The reduced PSF – sidelobe and PSF – background can be attributed to the use of a neutral density filter. Within its blocking wavelength range, a two-way transmission reduction can be calculated as $20 \times OD$ dB.

One dominant source of nonlinearity in VT-DBR laser spectra has its root in the sub-optimal stitching process [82], [99], [114]. This process, largely influenced by the calibration procedure [99], [114], introduces minor irregularities or discontinuities between the sub-intervals of the laser sweep, degrading the decimated signal. Besides the stitching process, other sources of nonlinearity contribute small yet noticeable variations between sweeps, resulting in deviation from the desired spectrum shape. As the spectrum is sparsely sampled at a 400 MHz rate, statistical fluctuations in amplitude between sweeps can be observed and attributed to limitation in electronics and control algorithms [119], [121]. At higher sweep rates [99], [121], such as 200 kHz, noticeable axial PSF

---

[a] The neutral density filter utilised for the PSF experiment was an Edmund, 3.0 OD 25mm, absorptive ND filter, optimized for sources within the 250-700 nm range [140]. However, the central wavelength of the aforementioned OCT system is 1550 nm. While a two-way transmission reduction is anticipated with this filter, it was not quantified because the wavelength lies outside the ideal blocking range of this filter.

degradation can be observed due to increased phase variation during the sweep, affecting the linearity and repeatability of the laser over time.

To assess the impact of drift over time on the phase stability and sweep linearity of the akinetic swept source, a static gold mirror was placed in the sample arm, as illustrated in Figure 2.16, allowing the extraction of magnitude and phase measurements for each recorded power spectrum at the peak position of the PSF coincident with the gold mirror's location. Furthermore, the magnitude and phase differences of the peak between adjacent A-lines at the mirror location were computed, and standard deviations were obtained from the respective distributions in Figure 2.17 (a) and (b). Figure 2.17 (d) presents a Gaussian-like profile with a standard deviation of 0.0061 a.u. for the magnitude difference, indicating low fluctuations in output power characteristic of the relative intensity noise (RIN) associated with the akinetic swept source. However, Figure 2.17 (e) also reveals a standard deviation of 27.97 mrad for the phase difference, attributed to phase drift occurring between adjacent A-lines. This value is considerably higher than previously reported values [99], suggesting the presence of a certain degree of phase instability within the imaging system.
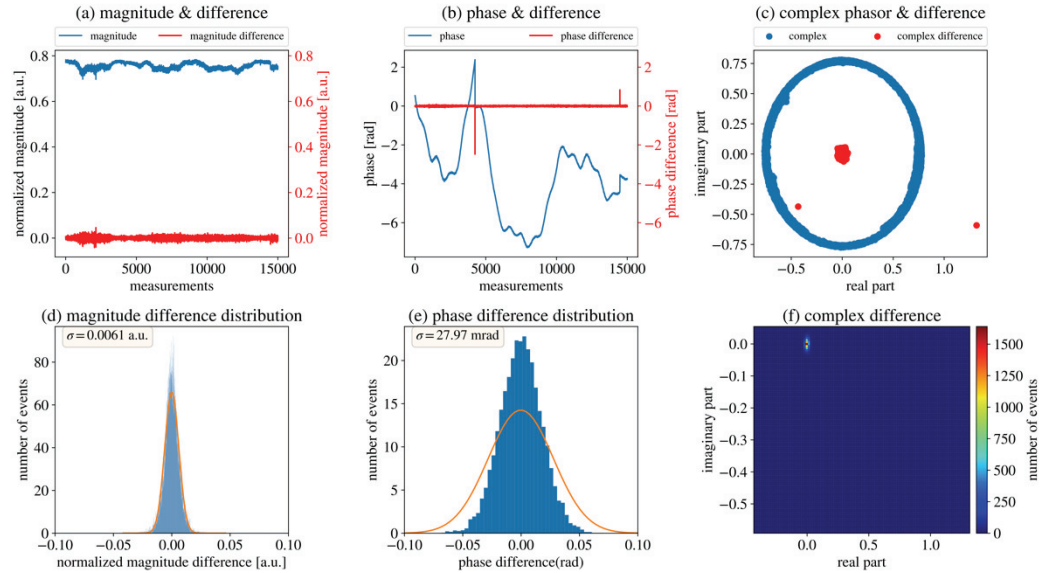
Figure 2.17: Insight akinetic swept source [99] phase stability and sweep linearity analysis conducted on the complex data using a gold mirror as described in Figure 2.16. The swept source laser's line scan rate was set to 100 kHz, and data was collected for 150 ms, resulting in a total of 150,000 measurements.

Figure 2.18 illustrates the cross-correlation of the interferometric peak associated with the gold mirror based on the analysis approach detailed in [99], [142]. Over a duration of 20 milliseconds, the shapes (i.e., location and amplitude) of the sidelobes within the OCT system exhibit stochastic fluctuations over time. These fluctuations are caused by thermal and mechanical drift in the system, and this variability in the sidelobes can impact the effectiveness of conventional deconvolution methods. In other words, even minor variations in the PSF can result in substantially different estimations of the underlying structure when employing traditional deconvolution techniques.
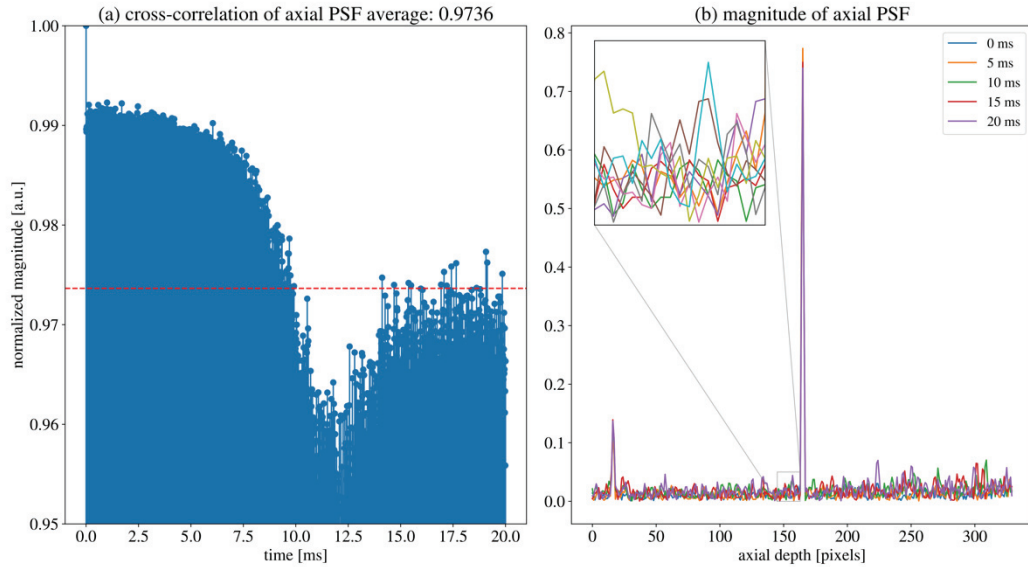
Figure 2.18: PSF stability analysis using cross-correlation on the log modulated magnitude data of the axial point spread function (PSF) with the described setup in Figure 2.16. (a) cross-correlation plot of the PSF with the PSF measured at time t=0. (b) the log-modulated magnitude data at each time point.

In FD-OCT systems, PSF degradation can be attributed not only to the characteristics of the light source but also to nonlinearities arising from limitations in the highest detectable frequency of the system [82], [143], which is influenced by the detection speed of the system and the sampling rate of the detector. For instance, despite employing a high sampling rate of 400 MHz using the master clock in the akinetic swept-source laser, sidelobes can still be observed in the acquired spectrum due to the Nyquist limitations of the acquisition [82], [99]. Consequently, these components fold back into the lower frequency range due to aliasing, leading to distortions and sidelobe artefacts in the A-line.

Chapter 3

Convolutional dictionary learning for blind deconvolution of optical coherence tomography images

Junzhe Wang,[1] Brendt Wohlberg,[2] Robert Adamson,[3, *]

[1] School of Biomedical Engineering, Dalhousie University, Halifax, NS B3H 4R2, Canada

[2] Theoretical Division, Los Alamos National Laboratory, Los Alamos, NM 87545, USA

[3] Electrical & Computer Engineering Department, Dalhousie University, Halifax, NS B3H 4R2, Canada

3.1 Author contribution statement

J. Wang and R. Adamson collaboratively developed the research methods, designed the experiments. R. Adamson further provided the rationale for clinical relevance. B. Wohlberg provided software support, contributed to the refinement of the methodologies employed, and offered constructive feedback for the manuscript drafts. J. Wang conducted the data analyses for this study and served as the primary author for the journal submission.

3.2 Preamble

This chapter is primarily based on my first peer-reviewed publication [144], with its core content remaining largely unchanged. However, to avoid redundancy, any introductory information that overlaps with Chapter 1 has been omitted or revised for the sake of brevity. I have taken the opportunity to include some unpublished experimental details and made adjustments to ensure consistency in terminology, style, and the presentation of results throughout the document.

In particular, the introductory section has been restructured to offer a clearer understanding of the motivation and novelty of the work at the time the original manuscript was submitted for peer review. This revision also highlights how the research

fits into the broader narrative of my thesis. Detailed explanations about the origins of the sidelobe and its impacts can be found in the preceding sections of the document.

3.3   Summary

In this study we demonstrate a sparsity-regularised, complex, blind deconvolution method for removing sidelobe artefacts and stochastic noise from optical coherence tomography (OCT) images. Our method estimates the complex scattering amplitude of tissue on a line-by-line basis by estimating and deconvolving the complex, one-dimensional axial point spread function (PSF) from measured OCT A-line data. We also present a strategy for employing a sparsity weighting mask to mitigate loss of speckle brightness within tissue-containing regions caused by the sparse deconvolution. Qualitative and quantitative analyses show that this approach suppresses sidelobe artefacts and background noise better than traditional spectral reshaping techniques, with negligible loss of tissue structure. The technique is particularly useful for emerging OCT applications where OCT images contain strong specular reflections at air-tissue boundaries that create large sidelobe artefacts.

3.4   Introduction

One major challenge in obtaining high-quality OCT images is the presence of sidelobe artefacts in the axial direction, which worsen image resolution and contrast [82]. These sidelobes originate from spectral non-uniformity in the OCT light source and/or spectral non-linearity [108], [113] and are further exacerbated by the presence of very strong reflections at tissue-air interfaces in the image.

The presence of sidelobe artefacts in OCT images can lead to a distorted representation of tissue structure, which may complicate the clinical interpretation of these images and increase the risk of misdiagnosis [82]. This is particularly concerning when clinical decisions are based on the morphological features revealed in the images.
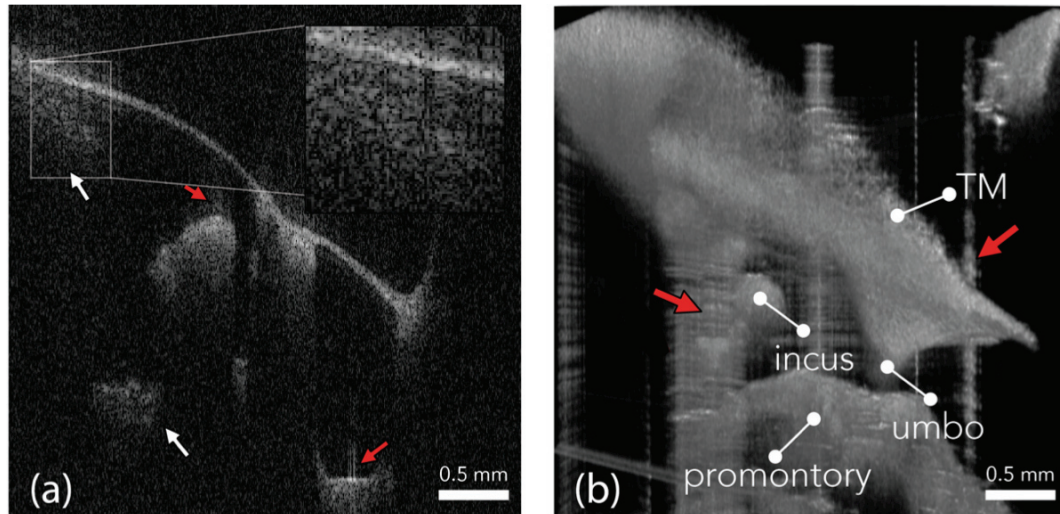
Figure 3.1: (a) 2D OCT middle ear image showing artefactual haze proximal and distal to middle ear structures (red arrows) caused by the imperfect point spread function of the OCT system and optics. (b) 3D volumetric OCT image of the same human middle ear where the effect of sidelobes artefacts is more prominent, as indicated by the red arrow. The strong sidelobe artefacts arise from bright specular reflections from the tympanic membrane which mask weaker structures such as incus.

Figure 3.1 illustrates the detrimental effect of sidelobe artefacts on image quality in both cross-sectional (2D) and three-dimensional (3D) volumetric images of the middle ear. Prominent sidelobe artefacts, extending from the tympanic membrane (TM) into the middle ear space, can obscure structures situated behind the TM and create visual clutters in both 2D and 3D images. In 2D images, sidelobe artefacts produce a hazy appearance around all structures at air-tissue boundaries, potentially causing thin structures like TM to appear thicker than their actual dimensions. These artefacts not only reduce the fidelity and contrast of the images but also challenge the ability of medical professionals to correctly identify and diagnose conditions based on the available visual data. Consequently, addressing and minimising the impact of sidelobe artefacts is crucial for enhancing the diagnostic utility of OCT images in clinical settings.

Sidelobe artefacts typically manifest as lines extending axially from bright reflectors. These artefacts not only impact middle ear OCT images but also pose significant challenges in emerging OCT applications such as dermatology [87], gastroenterology [87], lung imaging [76], imaging of the oral [89] and respiratory tract mucosa [75], and dental imaging where highly reflective air-tissue boundaries form part of the image.
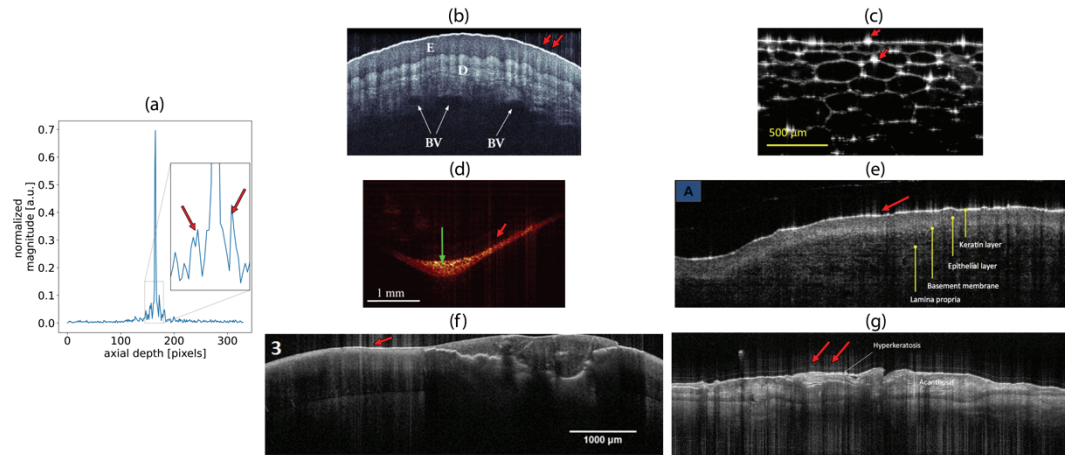
Figure 3.2: (a) Sidelobe artefacts(magnitude) and published image examples containing prominent sidelobe artefacts (indicated by red arrows). (b) OCT cross-sectional image of a human finger, taken with Thorlabs Inc. Telesto® Series OCT SD-system (Image courtesy of Thorlabs Inc.) (c) OCT cross-sectional image of an onion slice, taken with Wasatch Photonics Inc SD-system with a Cobra® 800 spectrometer (Image courtesy of Wasatch Photonics Inc.) (d) OCT cross-sectional image of human middle ear, taken with SS-OCT. (e) OCT cross-sectional image of oral squamous cell carcinoma, taken with Michelson Diagnostics EX1301 OCT Microscope V1.0. (f) OCT cross-sectional image of human tooth, taken with VivoSight® multiple-beam SS-OCT system. (g) OCT cross-section of human skin with an actinic keratosis with hyperkeratosis, taken with VivoSight® multiple-beam SS-OCT. Retrieved and modified with permission from [140].

In these applications, sidelobe artefacts are particularly troublesome due to the strong reflectors present in the images, which exacerbate the severity of artefacts and impede the accurate interpretation of OCT images as demonstrated in Figure 3.1. This, in turn, compromises the effectiveness of diagnoses and treatment decisions across various medical fields. Sidelobe artefacts are frequently observed contaminating numerous OCT images in published literature [99], [111], [145], indicating their pervasive presence in the field. Figure 3.2 displays six examples of published images that contain prominent sidelobe artefacts.

3.4.1 Conventional methods for sidelobe removal

Traditionally, sidelobe artefacts have been addressed using spectral reshaping techniques. Spectral windowing is the simplest and most widespread such technique [82], although more sophisticated windowing approaches have also been used [112]. Nonlinearities in the spectrum manifest as undesired high-frequency contents superimposed on the modulated frequency of the ideal spectrum [82].

Spectral reshaping techniques aim to numerically alter the frequency contents of the spectrum in order to suppress sidelobes while maintaining the mainlobe shape [142], [143]. One most common method for spectral reshaping is the windowing approach. In the windowing approach, exemplified in Figure 3.3, the frequency response of the source spectrum is modified by multiplying it with a window function, typically symmetric one [143]. Common window functions include Hamming, Hanning, Blackman, and Kaiser windows. Each of these functions exhibits unique properties and trade-offs, such as balancing the mainlobe width and sidelobe suppression [112].
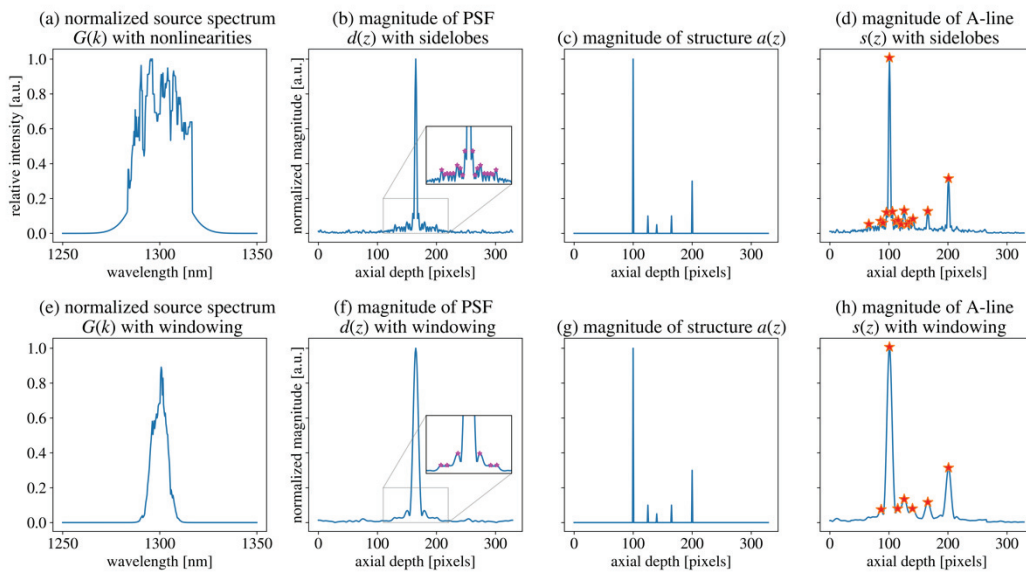
Figure 3.3: Extension of example demonstrated in Figure 2.9 where the top (i.e., from (a)-(d)) is the replica from the nonlinearity case in Figure 2.9 whereas the bottom (i.e., from (e)-(h)) shows the effect of applying spectral reshaping with Gaussian windowing to address the sidelobe artefacts.

However, spectral reshaping techniques introduce trade-offs between axial resolution and sidelobe suppression [82]. As illustrated in Figure 3.3 (f) and (h), these techniques effectively suppress sidelobes near the main peak, resulting in a cleaner and more accurate representation of the signal. However, the suppression of sidelobes occurs simultaneously with the broadening of the structure peaks. As the width of these peaks broadens, distinguishing between adjacent objects becomes increasingly difficult, leading to a reduction in achievable axial resolution. Furthermore, as linear techniques they are

limited in the degree of sidelobe suppression that they can achieve and have difficulty accurately removing artefacts from sharp image features such as tissue boundaries.

Because these sidelobe artefacts arise from convolution of the scattering amplitude with the axial PSF, deconvolution can be explored to compensate for the signal distortions introduced by the convolution.

If the PSF of an OCT system is known, deconvolution techniques such as Lucy-Richardson [148], [149], CLEAN [150], or gradual iterative subtraction (GIS) [111] can be used to suppress the artefacts by deconvolving the axial PSF from the measured A-lines, resulting in an improved image quality. In addition to suppressing sidelobes, deconvolution can also be used to achieve improvements to resolution and noise [148]. For instance, the CLEAN method [111], [150], [151], also known as orthogonal matching pursuit [152] (OMP), is an iterative deconvolution algorithm that was initially developed in the field of astronomy to reconstruct images of celestial objects from data that has been blurred by the instrument's PSF. This method is particularly advantageous in applications where the data contains a few dominant components that need to be identified and separated from background noise and artefacts [82], [150].
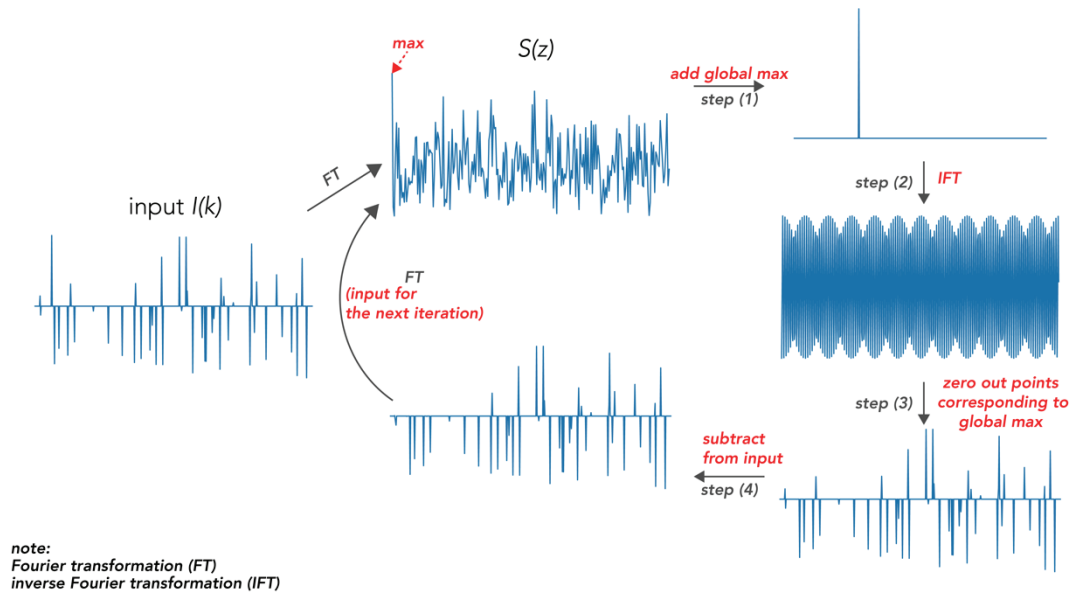
Figure 3.4: Overview of the CLEAN algorithm, summarised based on the description from [150], [151]

The general implementation of the CLEAN method is illustrated in Figure 3.4. The fundamental concept behind the CLEAN algorithm is to iteratively identify and

remove the dominant components from the local maximum found in the spectrum [150], [151], ultimately unveiling the underlying structure. The algorithm begins by initialising a sought vector (output) to zero with an original input spectrum containing the desired structures, sidelobe artefacts, and noise. In each iteration, the most significant peak (or component) in the spectrum with artefacts is identified and added to the sought vector. Subsequently, inverse Fourier transformation (IFT) of the updated sought vector is computed. The updated reconstruction is then subtracted from the original input spectrum, effectively removing the contribution of the dominant component while preserving the underlying structure. The subtracted result becomes the new input spectrum containing the remaining structures, artefacts, and noise for the next iteration. This iterative process continues until a sufficient number of iterations have been executed or a stopping criterion is satisfied. Upon completing the iterations, the resulting vector contains meaningful peaks corresponding to the structures uncontaminated by artifacts.

Other iterative approaches, such as Lucy-Richardson deconvolution [148], [151] and GIS [111] work in a similar way. However, they exhibit differences in their specific implementation techniques and stopping criteria. In the Lucy-Richardson method [148], the signal estimate is iteratively improved by minimising the discrepancy between the sidelobe-corrupted A-line and the estimated signal convolved with the PSF. Conversely, the GIS algorithm incrementally removes unwanted sidelobe components from each pixel along the A-line [111].

3.4.2 Impact of OCT noise contribution in deconvolution

The convolution theorem states that the Fourier transform of the convolution of two signals is equal to the pointwise product of their Fourier transforms [110]. This implies that a signal $\alpha(z)$ can be recovered from the convolved and sidelobe-corrupted signal $I(k)$ by inverting the convolution process, as shown in (2.9):

$$\alpha(z) = F^{-1}\left\{\frac{I(k)}{F\{\boldsymbol{d}(z)\}}\right\} \tag{3.1}$$

Naïve deconvolution, as (3.1) shows, involves dividing the Fourier transform of the convolved signal by the Fourier transform of the convolution kernel in the frequency domain. Subsequently, the original signal $\alpha(z)$ is obtained through the inverse Fourier

transform of the results. This seemingly straightforward division operation, known as the inverse problem, appears to be adequate to reconstruct a sidelobe-free $\alpha(z)$ in OCT through the deconvolution operation.

Unfortunately, though, the deconvolution problem is ill-posed due to the presence of noise during signal acquisition [151], [153], which complicates the deconvolution process. Inverse problems such as deconvolution can generally be classified as either well-posed or ill-posed [153], [154]. A well-posed inverse problem is one in which a solution exists, a unique solution can be determined, and the solution remains stable when subjected to small perturbations in the data or the model [155]–[157]. When reconstructing sidelobe-free OCT signals by the naïve deconvolution shown in (3.1), the presence of noise destabilises the deconvolution process[a] and small variations in the noise can result in significantly different estimations of the structure.

In OCT, shot noise, relative intensity noise (RIN), and thermal noise are the primary sources of noise [94], [142], [158]. To achieve optimal OCT performance, the system should operate in a shot noise-limited regime [82], [94], where shot noise is considered the dominant factor in the overall noise contribution, while other systematic noise sources are effectively suppressed through careful design and balanced detection [103], [158].

Shot noise

Shot noise originates from the quantum nature of photons interacting with the detector, and its intensity is governed by the optical power in the reference arm [82], [87], [100]. Photons from the incident light are absorbed at random, generating photoelectrons according to a Poisson probability distribution function. In fact, the SNR advantage of FD-OCT over TD-OCT can be attributed to the significant reduction in shot noise achieved by performing simultaneous axial acquisition in the Fourier domain [80], [82], [95].

---

[a] i.e., $[I(k) + I_{noise}]/[F^{-1}\{\boldsymbol{d}(z)\} \approx 0]$

Relative intensity noise (RIN)

Relative intensity noise (RIN) [80], [87], [158] characterises the unwanted amplitude fluctuations of the light source, expressed as a function of amplitude over optical frequency. If these fluctuations contain significant frequency components within the signal detection band, they can degrade the SNR and produce sidelobe artefacts.

In the case of the akinetic laser source discussed in this thesis, the akinetic laser demonstrates a remarkably flat RIN variation, attributable to the absence of mechanical tuning mechanisms within the laser [82], [99], [119]. This characteristic is considered an advantage of akinetic all-semiconductor lasers over kinetic lasers, as the frequency-dependent RIN in kinetic lasers is significantly influenced by mode hopping related to wavelength tuning and mode competition, particularly in lasers with longer cavities [82], [107].

Thermal noise

Thermal noise [85], [87], [94], another type of noise, affects the optical detector because of electronic thermal fluctuations. It is typically modelled as white Gaussian noise [94] and is independent of the optical power in the reference arm [82], [85].

Even in the ideal case where a noiseless OCT signal can be obtained, the axial PSF is considered band-limited assuming the PSF is spatially localised and approximated as a delta function. This means that the value of the PSF could be zero when the signal is also zero[a], which implies that there may be no solution for the deconvolution process in such cases.

3.4.3   Sparsity-based deconvolution method

One approach to addressing ill-posed problems involves introducing supplementary information [154], [159], known as regularisation terms, which can be derived from observations or assumptions about the signal [160], [161]. These terms aid in transforming ill-posed problems into well-posed ones by incorporating numerical constraints or penalties into the problem formulation, thereby yielding a more stable

---

[a] i.e., $[I(k) = 0]/[F^{-1}\{\boldsymbol{d}(z)\} = 0]$

result. For example, drawing a picture without any specific context can be challenging, However, if someone provides a hint that the expected picture is of a cat on a letter-sized paper, the drawing becomes more predictable and focused. Similarly, regularisation terms supply additional information that constrains ill-posed problems. These terms typically serve to constrain the solution in particular ways, such as promoting smoothness or sparsity.

In signal processing, sparsity pertains to the count of elements that are either zero or nearly zero [152], [162]. This principle carries significant relevance in the realms of signal and image processing, primarily because it facilitates efficient data representation and processing [161], [163], [164]. For example, let us consider a photograph of a cat, which can be reinterpreted as a simple line drawing. This minimalist rendering can effectively capture the key visual features, enabling straightforward identification. Thus, the line drawing represents a sparse depiction of the original image, distilling the essence while discarding less critical details, such as the texture of the fur. The sparsity of a description is a measure of its conciseness, indicating how efficiently the signal can be represented using a minimal number of significant elements. While a sparse representation can be useful for reducing the amount of data that needs to be processed, stored, or transmitted while still preserving critical information [151], [156], [164], there is often a trade-off between sparsity and reconstruction fidelity. For instance, consider the example of a cat drawn on a letter-sized paper again. A sparse description like "a cat on a piece of paper" is more concise, but it may omit details such as the position of the cat's tail, the colour of its fur, or the expression on its face. To retain these details, a more elaborate description might be necessary, even if it results in a less sparse representation. The trade-off between sparsity and reconstruction fidelity is a common challenge in sparse signal processing, necessitating careful consideration of the specific application and signal characteristics to maintain the balance between sparse representation and the preservation of essential details [151], [165], [166].

The choice of description, or basis in mathematical terms, plays a crucial role in determining the potential sparsity that can be achieved with given basis. An effective basis for sparse signal representation should the signal to be represented with a small number of non-zero coefficients, with the remaining coefficients being close to zero.

Different basis functions can be employed depending on the specific application and signal characteristics. Commonly used basis transformations that aim to generate a sparse representation include the discrete wavelet transform (DWT) [151], [167], [168], the Fourier transform (FT) [151] etc. For example, DWT, defined by a scaling function and a wavelet function, is particularly advantageous in applications of image compression, denoising, feature extraction, and edge detection as it allows for signal to be represented using a series of wavelet coefficients, which sparsely models the signal using a hierarchy of various scales and frequencies, In contrast, the Fourier Transform focuses on analysing the frequency content of signals and images and is often employed in image processing applications, including image filtering and restoration by decomposing a signal or image into a set of sinusoids, each representing the signal at different frequencies.
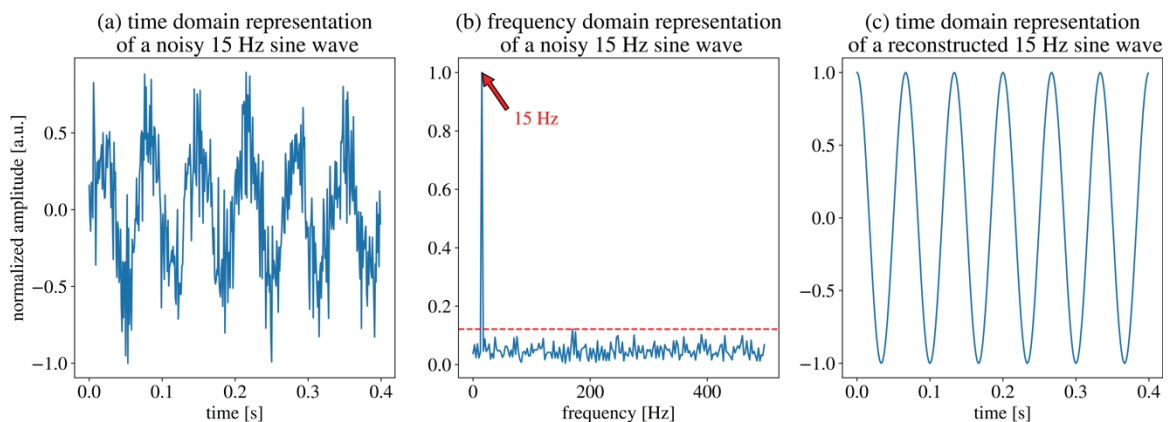
Figure 3.5: Example of sparsity and its application: (a) 15Hz sine wave with additive Gaussian noise in the time domain, (b) frequency domain representation of the 15Hz sine wave with additive Gaussian noise, where the red arrow indicates the main frequency component (15Hz) and the red dashed line represents the approximate threshold value based on the amplitude of noise across all frequency bins, (c) the reconstructed clean signal obtained by applying the threshold in the Fourier domain, where the sine wave can be sparsely represented.

Consider a 400-point, 15Hz sine wave signal with white noise as shown in Figure 3.5. In the frequency domain, this signal can be represented by just one main peak with small ripples, as opposed to the 400 non-zero coefficients needed to describe the signal in the time domain. The frequency-domain representation of the signal is sparse while the time-domain representation is not. This information can be used to compress the signal and restore a noise free signal. In the case where a signal contains noise, it can be first

expressed using its sparse basis, and then thresholding can be applied to remove the noise. As random noise does not exhibit sparsity in any domain, it is readily distinguishable and can be effectively separated from the signal of interest.

The concept of sparse representation is relevant to areas like compressed sensing (CS) [155], [163], which has been widely used in MRI imaging [155] and other biomedical imaging techniques. In these applications, the goal of CS is to recover a sparse signal from a limited set of measurements. In signal estimation problems, the goal is to obtain a high-fidelity estimate of a signal from a lower-fidelity measurement contaminated by noise. A common approach to generate this estimate involves conducting an optimisation over the signal space which is achieved by minimising a specific cost function. This cost function quantifies the fidelity of the estimate in relation to the measured signal and integrates any constraints on the signal, such as those imposed by regularisation. In such frameworks, regularisation is achieved by imposing a constraint to the cost function that includes the desirable characteristics of fidelity and sparsity expressed using various norms. The l_p-norm $||x||_p$ of a signal vector x_i is defined as

$$||x||_p = \left(\sum_{i=i}^{N} |x_i|^p \right)^{\frac{1}{p}} \tag{3.2}$$

where x_i is the i-th element in a vector x. The most common norms in signal estimation are the l_0, l_1, and l_2 norms. The l_0 norm, a direct measure of sparsity, is defined as the number of non-zero elements in the signal vector, while the l_1 norm is the sum of the absolute value of the elements. Minimising the l_1 norm promotes sparsity and is often used in practice for sparse recovery due to its computational efficiency and convexity[a]. The l_2 norm, calculates the square root of the sum of the squared coefficients but does not promote sparsity as effectively as the l_1 norm.

---

[a] A function is convex if for any two points a and b in the domain of a function f, and for any t in the range [0, 1], that $f(ta + (1 - t)b) \leq tf(a) + (1 - t)f(b)$ [154].
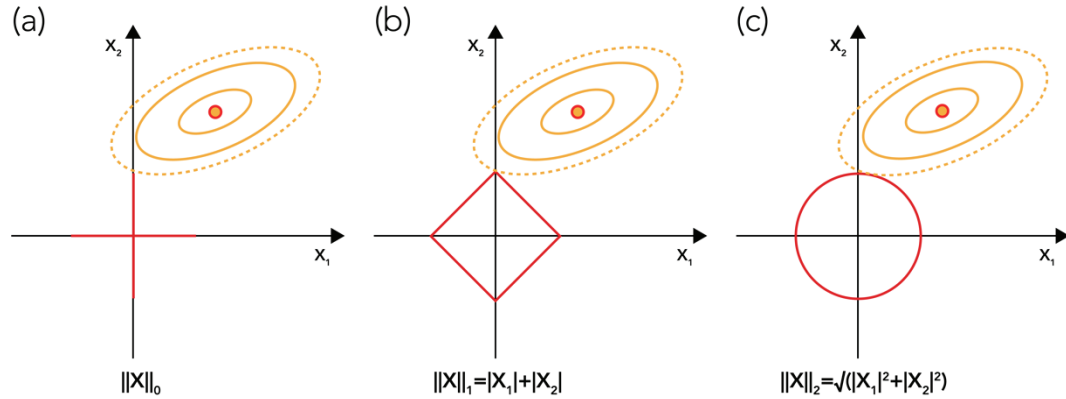
Figure 3.6: Geometrical interpretation of different norms in 2D space. (a), (b) and (c) are the unit ball representation of l_0, l_1 and l_2, respectively. The two arbitrary axes are the vertical and horizontal components of vector where the yellow contour represents a constant value of the residual error between the approximation and ground truth.

The previous discussion can be explained through visual representation with Figure 3.6 where the solid red line represents the aforementioned regularisation norms. Assume in a 2D space and for the l_0 norm, the same value lies along either the x_1 or x_2 axis, as there is only one non-zero element. The l_1 norm can be visualised with a diamond that distance between each corner to the origin equals, whereas the l_2 norm is expressed as a unit circle. Each contour represents a constant value of the error term between the estimation and the ground truth. The error is minimised at the red point and increases as the contour moves away from it. As the contour approaches the origin, it touches the constraint imposed on the solution. For the l_1 norm, the solution is found where the contour touches the diamond's corner and intersects the x_2 axis, yielding a sparse solution with one of the two coefficients (the x_1 coordinate) in the 2D vector being zero. This is the same solution that would be achieved with an l_0 norm [152]. However, minimising the l_2 norm results in a non-sparse solution, with both x_1 and x_2 components non-zero.

3.4.4   Basis pursuit denoising (BPDN)

In the 1990s, Donoho first recognised that by applying linear programming methods to minimise a cost function involving an l_1 norm, one can find an estimate of a signal within

an overcomplete signal basis dictionary[a] that maximises the sparsity of the representation [152]. This optimisation method, called the basis pursuit, was shown to have an wide applicability across many fields including image processing [171], [172], communications [166], spectral estimation [159], speech processing [166], [173], music [165], [173], medical imaging [174] and biomedical signal processing [174], [175] in which signals of interest are empirically known to be sparse in some basis.

A formulation of the problem of finding a sparse estimate of a given signal that is amenable to efficient, global optimisation using convex optimisation methods is the basis pursuit denoising (BPDN) problem. This problem has been widely applied and has been shown to be effective at reducing noise and at achieving super-resolution [170], [172] in many fields including OCT imaging. The conventional formulation of the BPDN problem is typically presented as the minimisation of a cost function, expressed as:

$$\underset{x}{\text{argmin}} \left(\frac{1}{2} \|s - Dx\|_2^2 + \lambda \|x\|_1 \right) \tag{3.3}$$

Where x is a vector on a defined, overcomplete dictionary D, s is a signal to be sparsely represented and, λ is a regularisation parameter [176]. The first term in the cost function represents the squared error between a measured signal s and its sparse representation Dx. The second term is the λ-weighted l_1 norm of the vector x. As famously shown by Donoho [152], minimising the l_1 norm of a vector maximises its sparsity and so the second term in the cost function favors solutions in which x is more sparse. The regularisation parameter λ balances the trade-off between sparsity and fidelity where a larger value of λ emphasizes sparsity [161], [176], leading to a sparser representation, but potentially sacrificing some fidelity between the estimate and the measured signal. On the other hand, a smaller value of λ prioritizes the fidelity term, resulting in an estimate that

---

[a] In signal processing, a dictionary refers to a set of elements or components that can be used to construct or reconstruct signals. A dictionary is deemed complete if it enables the reconstruction of a signal with a linear combination of the smallest number of elements. This concept is embodied in Fourier analysis, which is often regarded as a complete dictionary since it consists of sine and cosine functions at varying frequencies. On the other hand, an overcomplete dictionary possesses more elements than the essential minimum required for signal reconstruction. This surplus of elements provides an added level of flexibility in the reconstruction process, thereby offering more versatility in handling diverse or complex signals [152], [169], [170].

more closely resembles the measured signal but with a less sparse representation. An acceptable value of λ generally needs to be determined empirically on the class of signals being sparsely represented.

While capable of producing excellent sparse representations of signals, the BPDN problem is computationally intensive to solve, and its complexity increases with the size of the dictionary [164]. However, for time- or space- invariant signals that have a convolutional structure, this structure can be exploited to substantially reduce the size of the required dictionary for BPDN and hence the complexity of the optimisation problem [156]. The convolutional basis pursuit denoising problem CBPDN is a variant of BPDN that assumes a convolutional structure for the signal. Its general formulation is [176]:

$$\underset{x}{\arg\min} \left(\frac{1}{2} \left\| s - \sum_{m=1}^{M} \boldsymbol{d}_m * \boldsymbol{x}_m \right\|_2^2 + \lambda \sum_{m=1}^{M} \|\boldsymbol{x}_m\|_1 \right) \tag{3.4}$$

Where the search is conducted over multiple sparse vectors $\boldsymbol{x}_m$ and the dictionary consists of multiple convolution kernels $\boldsymbol{d}_m$ that are convolved with the $\boldsymbol{x}_m$ and summed to sparsely approximate the measured signal $\boldsymbol{s}$.

For the purposes of the present study, we make the simplification that $M = 1$ since we aim to deconvolve a single PSF from the measured signal. This simplifies equation results in (3.4) to

$$\underset{x}{\arg\min} \left\{ \frac{1}{2} \|\boldsymbol{s}(z) - \boldsymbol{d}(z) * \boldsymbol{x}(z)\|_2^2 + \lambda \|\boldsymbol{x}(z)\|_1 \right\} \tag{3.5}$$

However, these conventional deconvolution and sparsity-based methods require a priori knowledge of the PSF (i.e. of the convolution kernels $\boldsymbol{d}(z)$) from either numerical modelling [177] or experimental measurements [148]. Such methods therefore have difficulty in addressing sidelobe artefacts when the PSF varies over time due to thermal and mechanical drift [99] and they require system-specific calibration to measure the PSF, adding complexity and cost to the system design. Depending on the implementation, measuring the PSF may also entail interrupting imaging, causing a decrease in frame rate.

A preferred approach, which we demonstrate for the first time in this study, is to estimate and then deconvolve the axial PSF using only data collected as part of normal imaging, performing so-called blind deconvolution in which the axial PSF is determined

from imaging data rather than from a separate measurement. While blind deconvolution techniques are common in image processing [178] and have been previously been applied to improving lateral resolution in OCT [179], [180] to the best of our knowledge this is the first application of blind deconvolution of the complex PSF from OCT A-lines to address the problem of axial side-lobe artefacts. Our sparsity-regularised approach to blind deconvolution of OCT A-lines is model-free and requires no modification to hardware or image sequencing. The method can be applied to already-collected OCT data, so long as the complex A-line data or spectrogram data was retained.

3.4.5   Convolutional sparse coding

If a signal is known to have a convolutional structure – i.e., to consist of a PSF convolved with an unknown vector – and the unknown vector is known to be sparse, i.e., to have a significant fraction of its elements with negligibly small amplitudes, sparse representation methods can be applied to the problem of estimating the unknown vector and the PSF from measured signals [181]. While the sparsity of OCT images is application-specific, many OCT tissue images contain a large fraction of non-reflective regions that would have zero intensity in an ideal image. This makes OCT images good candidates for applying techniques that attempt to reconstruct a maximally sparse estimate of the image consistent with the data.

Over the last 20 years, sparse representation techniques that employ optimisation over an l_1 norm to find the sparsest representation of a vector within an overcomplete dictionary [182] have been widely applied across many fields of signal processing for denoising [183], compressed sensing [184], interpolation and unsupervised machine learning [185]. The general framework for sparse optimisation can be applied to the problem of deconvolution in which a measured signal is assumed to be formed as the convolution of a PSF, typically a short pattern that is repeated throughout the signal, and a sparse vector containing information about where in the signal the pattern occurs and its local amplitude [164]. In cases where the PSF is not known a priori, dictionary learning approaches can be used to estimate the PSF from examples of the measured data [164] which turns the sparse estimation into a blind deconvolution method. In recent years, such approaches have been extensively developed in the fields of image processing [166], [169], [186], analysis of neural signals [187], and in the analysis of music [188], [189].

Sparse representations have previously been used in the processing of OCT images. Compressed sensing (CS) techniques that use sparse representations have been applied to reduce the number of spectral or spatial samples needed to form OCT images [160], [190]. Sparsity-based denoising [191] and image compression [192] techniques have also been developed for processing of B-mode OCT images. Sparse estimation techniques have also been applied to A-line reconstruction [193], [194] to improve axial resolution. However, to our knowledge, sparsity-based processing approaches have not previously been applied to the deconvolution of A-line OCT data. A-line deconvolution requires the extension of sparse representation methods originally developed for real-valued signals to allow for both a complex PSF and a complex sparse vector. It also requires methods for ensuring that sparse representations correctly capture tissue speckle, which is an inherently non-sparse and essential feature of OCT imaging data.

In this study we present a novel blind deconvolution method for complex OCT A-lines based on a sparse representation that is tolerant of tissue speckle. We show that our method is effective in simultaneously suppressing sidelobe artefacts and noise from OCT images while preserving tissue speckle.

3.5 Convolutional sparse coding for A-line deconvolution

We approach the deconvolution of OCT A-lines by representing A-line estimation using the convolutional sparse coding (CSC) problem, a well-studied problem in sparse estimation theory [195]. The CSC problem is a minimisation problem over the vector $\boldsymbol{x}(z)$ expressed as

$$\operatorname*{argmin}_{x}\left\{\frac{1}{2}\|\boldsymbol{s}(z) - \boldsymbol{d}(z) * \boldsymbol{x}(z)\|_2^2 + \lambda\|\boldsymbol{x}(z)\|_1\right\} \tag{3.6}$$

where the cost function in (3.6) includes an l_2 term expressing the fidelity between an input A-line signal $\boldsymbol{s}(z)$ and the convolution between an axial PSF $\boldsymbol{d}(z)$ and an estimate of the scattering amplitude $\boldsymbol{x}(z)$ and an l_1 regularisation term that enforces the sparsity of $\boldsymbol{x}(z)$. A regularisation parameter λ determines the relative weighting between the fidelity and sparsity terms. Larger values of λ will promote the sparsity of the estimate $\boldsymbol{x}(z)$ at the expense of fidelity while smaller values will favour fidelity between $\boldsymbol{s}(z)$ and $\boldsymbol{d}(z) * \boldsymbol{x}(z)$ at the expense of sparsity. An acceptable value of λ generally needs to be

determined heuristically on the class of signals being sparsely estimated [171]. (3.6) is a simplified form of the more general CSC problem (3.4) which involves a sum over multiple convolutional terms [195]. To be more specific, when applied to OCT A-line signals with (3.4) as deconvolution method, we can assume a structure for the signals s in which there is a single convolution kernel, namely the axial point spread function. In this case we can reduce the sum over m to a single term in which we interpret the convolutional kernel d (where we have dropped the subscript m) as the PSF and the sparse vector x as a sparse estimate of the scattering amplitude $\alpha(z)$.

Because the CSC problem is designed to find a sparse estimate of each OCT A-line, its success depends on the scattering amplitude $\alpha(z)$ of the tissue actually being sparse. In many applications, OCT A-lines are macroscopically sparse [161], containing relatively few brightly reflecting structures and large regions with no reflectors. However, within tissue regions, OCT images exhibit speckle, a temporally static, spatially random texture that is not microscopically sparse [190], [196]. When sparsely regularised optimisation methods are applied to speckle-containing images, the optimisation tends to cause loss of brightness when low-intensity points within a speckle-containing region are set to zero intensity to increase the sparsity of the estimate $x(z)$. Within the CSC framework, this effect can be mitigated by using a spatially varying weighting of the l_1 term in the cost function whereby a larger weight is applied to the l_1 term in regions that are free of structure and a smaller weight is applied in regions containing structure. This weighted form of the CSC problem is given by [166]:

$$\operatorname*{argmin}_{x}\left\{\frac{1}{2}\|s(z) - d(z) * x(z)\|_2^2 + \lambda\|W(z)x(z)\|_1\right\} \tag{3.7}$$

where $W(z)$ is a depth-dependent weighting factor applied to the l_1 term.

3.5.1 Convolutional dictionary learning for axial point spread function estimation

However, applying CSC-based optimisation as a sparsity-regularised deconvolution method still requires that the PSF $d(z)$ be known a priori and provided as an input to the optimisation process. This means that as we have formulated it, CSC is a deconvolution method rather than a blind deconvolution method. To develop CSC into a blind deconvolution method, the CSC problem can be extended to also include optimisation

over the PSF $d(z)$. This enhancement is called convolutional dictionary learning (CDL) [176]. In CDL, the PSF is determined through optimisation over a set of K OCT A-lines. The CDL problem can be written as:

$$\underset{d, x_k}{\text{argmin}} \left\{ \frac{1}{2} \sum_{k=1}^{K} \|s_k(z) - d(z) * x_k(z)\|_2^2 + \lambda \sum_{k=1}^{K} \|x_k(z)\|_1 \right\} \tag{3.8}$$

$$s.t. \|d(z)\|_2 = 1$$

where the minimisation runs over both a PSF $d(z)$ and a set of K sparse A-line estimates $x_k(z)$ such that the average error between the sparse representations $d(z) * x_k(z)$ and a set of K measured A-lines $s_k(z)$ is minimised. When applied to OCT A-lines collected over a short enough period that the PSF remains stable, the $s_k(z)$ can consist of A-lines at different lateral locations within an image in which case k indexes the lateral location.

The solution to this minimisation problem consists of a set of sparse vectors $x_k(z)$ that are estimates of the scattering amplitude $\alpha_k(z)$ at each of K lateral locations and an estimate of the axial PSF $d(z)$, assumed to be independent of lateral location k[109]. In determining $d(z)$, the optimisation identifies axially shift-invariant patterns that are common across and within the measured signals $s_k(z)$ while ignoring features like background noise that are spatially random across and within A-lines. Used in this way, the CDL problem of (3.8) amounts to a sparsity-regularised blind axial deconvolution of a complex 2D OCT image.

The CDL problem can be efficiently solved by alternately optimising for the $x_k(z)$ with $d(z)$ fixed in a sparse coding step and optimising for $d(z)$ with $x_k(z)$ fixed in a dictionary update step [197]. For efficient solution of both the CSC and the CDL problems, one can use (among other options [176], [198]) the alternating direction of multipliers method (ADMM) [195].

The ADMM is a mathematical approach for solving convex optimisation problems by transforming the original cost or objective function which may not necessarily be convex—into a convex problem [154], [157], [199], [200]. This transformation is achieved through constructing an augmented Lagrangian of the original objective function, introducing dual variables, and then iteratively updating the primal and dual variables. For example, an optimisation question can be expressed in the form [154]:

$$argmin\ f(x) + g(z)\ s.t.\ Ax + Bz = c \tag{3.9}$$

where $x \in R^s$, $z \in R^n$, $A \in R^{p \times n}$, $B \in R^{p \times n}$, $c \in R^p$, that is x, z and c are real-valued vectors with s, n and p elements, respectively. And A and B are real-valued matrix with p rows and n column. The augmented Lagrangian can be constructed by defining a dual variable y, a penalty parameter $\rho > 0$ where it combines the objective function with the constraints into a single equation that can be solved for the optimisation values [154], [200]:

$$L_\rho(x, z, y) = f(x) + g(z) + y^T(Ax + Bz - c) + \frac{\rho}{2}\|Ax + Bz - c\|_2^2 \tag{3.10}$$

The result of the second term, denoted as $y^T(Ax + Bz - c)$, is a scalar value, which measures the extent of constraint violation. The last term in the Lagrangian function serves as a penalty factor imposed on the l_2 norm of the constraint violations. Denoted by ρ, this parameter controls the degree of this penalty. Higher values of ρ lead to a larger penalty for constraint violations, pushing the optimisation process more aggressively towards solutions where the constraints are satisfied. Assuming that the $f(x)$ and $g(z)$ are convex and initializing the variables x, z, and y, The ADMM then follows a three-step iterative procedure in each $k + 1$ iteration until a specified convergence criterion is satisfied [154], [200]:

1. Solve the following to update x while fixing z and y:

$$\begin{aligned}
x^{\{k+1\}} = \underset{x}{argmin}\Big\{ &f(x) + (y^k)^T(Ax + Bz^k - c) \\
&+ \left(\frac{\rho}{2}\right)\|Ax + Bz^k - c\|_2^2\Big\}
\end{aligned} \tag{3.11}$$

2. Solve the following to update z while fixing x and y:

$$\begin{aligned}
z^{\{k+1\}} = \underset{z}{argmin}\Big\{ &g(z) + (y^k)^T(Ax^{\{k+1\}} + Bz - c) \\
&+ \left(\frac{\rho}{2}\right)\|Ax^{\{k+1\}} + Bz - c\|_2^2\Big\}
\end{aligned} \tag{3.12}$$

3. Update the Lagrange multiplier y:

$$y^{\{k+1\}} = y^k + \rho(Ax^{\{k+1\}} + Bz^{\{k+1\}} - c) \tag{3.13}$$

In the framework of ADMM, the roles of primal and dual residuals, represented as r and s respectively, are twofold [157], [164]. First, they serve as stopping criteria, bringing the

iterative process to a halt upon reaching predetermined thresholds. Second, they dynamically monitor and measure the extent of constraint violations:

$$r^k = x^k - z^k \tag{3.14}$$

$$s^k = -\rho(z^k - z^{k+1}) \tag{3.15}$$

The rate of convergence in the ADMM is closely tied to the penalty parameter ρ, with the performance of ADMM dependent on its initially chosen value. Notably, a smaller value of ρ tends to favor a reduction in dual residual, possibly at the expense of a larger primal residual. Given the dynamic nature of the residuals throughout the iterative process, a static value of ρ may not always produce efficient convergence. It is therefore preferable to dynamically adjust the value of ρ with an adaptive mechanism, as it maintains a balance between the primal and dual residuals, ensuring that the algorithm converges more effectively [164].

The specific methods of updating variables x and z depends on the forms of $f(x)$ and $g(z)$. If they are differentiable, methods such as gradient descent can be used. In the case where those functions are not differentiable, alternatives such as proximal methods can be considered [154], [176], [195], [195], [200].

We describe the ADMM method as applied to the CDL problem below. ADMM solves the CSC problem in a similar way, only with a fixed, known $d(z)$ and a single measured A-line $s(z)$ and a single sparse vector $x(z)$ in lieu of the ensembles of K measured A-lines $s_k(z)$ and sparse vectors $x_k(z)$ used in CDL.

3.5.2 Convolution dictionary learning and convolutional sparse coding in the complex domain

For complex-valued $x_k(z)$ and $d(z)$, the sparse coding step in conventional CDL ADMM solvers designed for real-valued signals must be modified to work with complex vectors as originally proposed in [201]. The cost function of (3.8) can be generalised to complex $x_k(z)$ and $d(z)$ by defining the l_1 and l_2 norms on complex arguments as

$$\|x_k(z)\|_1 = \sum_{i=1}^{N} |x_k(z_i)| \tag{3.16}$$

and

$$\|s_k(z) - d(z) * x_k(z)\|_2^2 = \sum_{i=1}^{N} |s_k(z_i) - d(z_i) * x_k(z_i)|^2 \qquad (3.17)$$

where N is the number of pixels in the axial direction, $|\cdot|$ denotes the magnitude of a complex number and $s_k(z)$, $d(z)$ and $x_k(z)$ are all complex vectors.

In the ADMM method, the sparse coding step is solved by converting (3.8) to matrix form

$$\underset{X}{argmin}\left\{\frac{1}{2}\|DX - S\|_2^2 + \lambda\|X\|_1\right\} \qquad (3.18)$$

where $D \in \mathbb{C}^{N \times N}$ is the matrix form of the convolution operator with $d(z)$ such that $d(z) * x_k(z) = DX$, $S = [s_1(z), \dots, s_k(z), \dots, s_K(z)] \in \mathbb{C}^{N \times K}$ is a matrix formed from the measured A-lines $s_k(z)$, and $X = [x_1(z), \dots, x_k(z), \dots, x_K(z)] \in \mathbb{C}^{N \times K}$ is a matrix formed from the sparse vectors $x_k(z)$. DX is then the sparse estimate of S. N is the number of elements in x and s.

The problem is then transformed into a constrained optimisation problem which is solved by minimisation of an augmented Lagrangian function containing a dual variable $U \in \mathbb{C}^{N \times K}$ and an auxiliary variable $Y \in \mathbb{C}^{N \times K}$. A real, positive parameter ρ governs the rate of convergence. In this study ρ is selected using the adaptive method described in [164].

$$L_\rho(X, Y, U) = \frac{1}{2}\|DX - S\|_2^2 + \lambda\|Y\|_1 + \frac{\rho}{2}\|X - Y + U\|_2^2 \qquad (3.19)$$

3.5.3 Find X that minimises L_ρ with Y held constant

This problem can be formulated as

$$\underset{X}{argmin}\left\{\frac{1}{2}\|DX - S\|_2^2 + \frac{\rho}{2}\|X - Y + U\|_2^2\right\} \qquad (3.20)$$

This minimisation can be solved by setting the derivative of L_ρ to zero, leading to a linear equation system:

$$(D^H D + \rho I)X = D^H S + \rho(Y - U) \qquad (3.21)$$

where the H superscript denotes the Hermitian transpose. The equation system can be solved in the frequency domain by taking the discrete Fourier transform (DFT) of both sides

$$\left(\widehat{\boldsymbol{D}}^H\widehat{\boldsymbol{D}} + \rho\boldsymbol{I}\right)\widehat{\boldsymbol{X}} = \widehat{\boldsymbol{D}}^H\widehat{\boldsymbol{S}} + \rho\left(\widehat{\boldsymbol{Y}} - \widehat{\boldsymbol{U}}\right) \tag{3.22}$$

where $\widehat{\boldsymbol{A}}$ is the DFT of $\boldsymbol{A}$. The solution can then be obtained by exploiting the Sherman-Morrison formula [164].

3.5.4 Find Y that minimises L_ρ with X held constant

This problem can be written as

$$\underset{\boldsymbol{Y}}{\mathrm{argmin}}\left\{\lambda\|\boldsymbol{Y}\|_1 + \frac{\rho}{2}\|\boldsymbol{X} - \boldsymbol{Y} + \boldsymbol{U}\|^2\right\} \tag{3.23}$$

This is the step that must be modified for complex variables. When $\boldsymbol{X}, \boldsymbol{Y}$ and $\boldsymbol{U}$ are real-valued, the problem has a closed-form solution

$$Y = \mathcal{S}_{\frac{\lambda}{\rho}}(\boldsymbol{X} + \boldsymbol{U}) \tag{3.24}$$

where $\mathcal{S}(\cdot)$ is the soft thresholding operator defined for real-valued $\boldsymbol{A}$ as

$$\mathcal{S}_\gamma(\boldsymbol{A}) = \mathrm{sign}(\boldsymbol{A}) \odot \max(0, |\boldsymbol{A}| - \gamma) \tag{3.25}$$

where $\odot$ denotes element-wise multiplication and the $\mathrm{sign}(\cdot)$ and $\max(\cdot)$ functions are applied elementwise.

However, the $\mathrm{sign}(\cdot)$ operator is not defined on complex numbers. Following [201] for $\boldsymbol{A} \in \mathbb{C}$ we define a complex soft thresholding function

$$\mathcal{CS}_{\lambda/\rho}(\boldsymbol{A}) = \frac{\boldsymbol{A}}{|\boldsymbol{A}|} \odot \max(0, |\boldsymbol{A}| - \gamma) \tag{3.26}$$

which is equivalent to (3.24) when $\boldsymbol{A}$ is real. $\mathcal{CS}_{\lambda/\rho}(\boldsymbol{A})$ preserves the phase of the complex vector for $|\boldsymbol{A}| > \gamma$ and collapses vectors with $|\boldsymbol{A}| \leq \gamma$ to the origin on the complex plane. This function provides a closed form solution to (3.23) for complex vectors.

The dictionary update step in the ADMM CDL solution is unaffected by whether $\boldsymbol{d}(z)$, $\boldsymbol{x}(z)$ and $\boldsymbol{s}(z)$ are complex, and therefore does not require modification. A full

derivation of the ADMM solution to the CDL problem with complex vectors using the complex soft thresholding function can be found in [201].

In this study, we applied the CDL framework to perform blind deconvolution of complex OCT A-lines with the goal of suppressing PSF sidelobe artefacts and noise while preserving structural fidelity. All CDL and CSC processing used the open-source, Python-based SPORCO toolkit [202] which, for this study, was extended to support complex-valued sparse estimation using complex soft thresholding. SPORCO supports several solvers, but all results in this study use its CDL ADMM solver or its CSC ADMM solver. All source code and example data for the methods applied in this study can be accessed from our public GitHub repository [203].

3.6 Methods
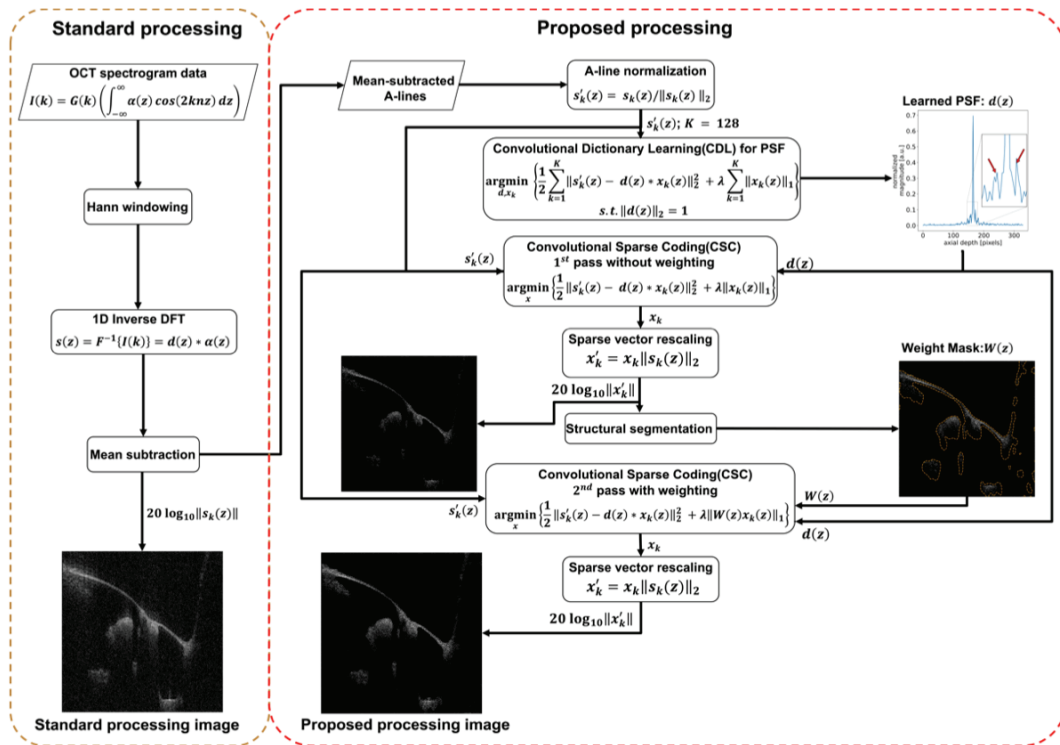
Figure 3.7: Standard and proposed OCT A-line processing methods. The proposed method uses convolutional dictionary learning for axial PSF estimation and convolutional sparse coding for sparse estimation of the tissue structure.

OCT spectrogram data was collected using a previously described [106], [135] OCT system designed around a 1550nm akinetic swept laser source (Insight Photonics

SLE-101) with a sweep bandwidth of 40nm[a], axial resolution in air of 40 μm, lateral resolution in air at the focus of 35 μm and a nominal sweep rate of 100 kHz. The beam was scanned laterally using a 2D MEMS mirror (Mirrorcle A8L2.2). The system was designed for imaging of the middle ear and by design it has lower axial and lateral resolution than typical ophthalmic OCT systems. In each image dataset, we collected 10,240 A-lines over 102.4 ms and sampled every 20th line to form a B-mode dataset with a lateral width of 512 pixels. We applied a standard set of A-line preprocessing steps to the spectrogram data [82], which we will refer to as *standard processing* in this study. Standard processing consisted of windowing with a Hann window to compensate for the source spectrum non-uniformity, inverse discrete Fourier transformation (DFT) and fixed pattern noise removal by mean subtraction [204]. The two processing methods are shown in flowchart form in Figure 3.7. In what follows, the reference images have only had these standard processing steps applied while the deconvolved images have had these steps applied before applying the proposed processing.

Because the l_1 and l_2 terms in the cost functions of (3.6) and (3.8) scale differently with $\mathbf{s}_k$, $\mathbf{s}_k$ was normalised by its l_2 norm on each line prior to performing the sparse optimisation so that the same value of λ could be used across all A-lines. That is, we rescaled $\mathbf{s}_k(z)$ to $\mathbf{s}'_k(z) = \mathbf{s}_k(z)/\|\mathbf{s}_k(z)\|_2$. Following convolutional sparse coding, we rescaled $\mathbf{x}_k$ to $\mathbf{x}'_k = \mathbf{x}_k\|\mathbf{s}_k(z)\|_2$ to restore the sparse vector signal amplitude to the level of the measured signal.

The set of normalised complex A-lines $\mathbf{s}'_k(z)$ form the input to the CDL ADMM solver. In each image, we learned the PSF $\mathbf{d}(z)$, demonstrated in Figure 3.8, using a subset of lines consisting of every fourth line out of the 512 (so that $K = 128$) using a CDL solver with λ=0.1, and then applied a CSC solver to obtain the sparse vector $\mathbf{x}'_k(z)$ of all 512 lines using the PSF from the CDL solution. It is noteworthy that CDL presupposes that the input image possesses features with a sparse convolutional structure, indicative of a repeated, spatially shift-invariant pattern. In contrast, if the input image is

---

[a] As of the time this manuscript was published [144], the sweep bandwidth was 40nm, as opposed 35.4nm mentioned in the previous chapter. This sweep bandwidth improvement from 35.4nm to 40nm was achieved through a firmware update.

non-sparse or lacks a convolution structure with repeating patterns, it makes the CDL calculation ill-posed. Although it is possible to learn the PSF starting from a random initial guess [201], we found that picking one of the normalised A-lines as the initial guess for the PSF $d(z)$ accelerated the dictionary learning process while arriving at the same PSF estimate.
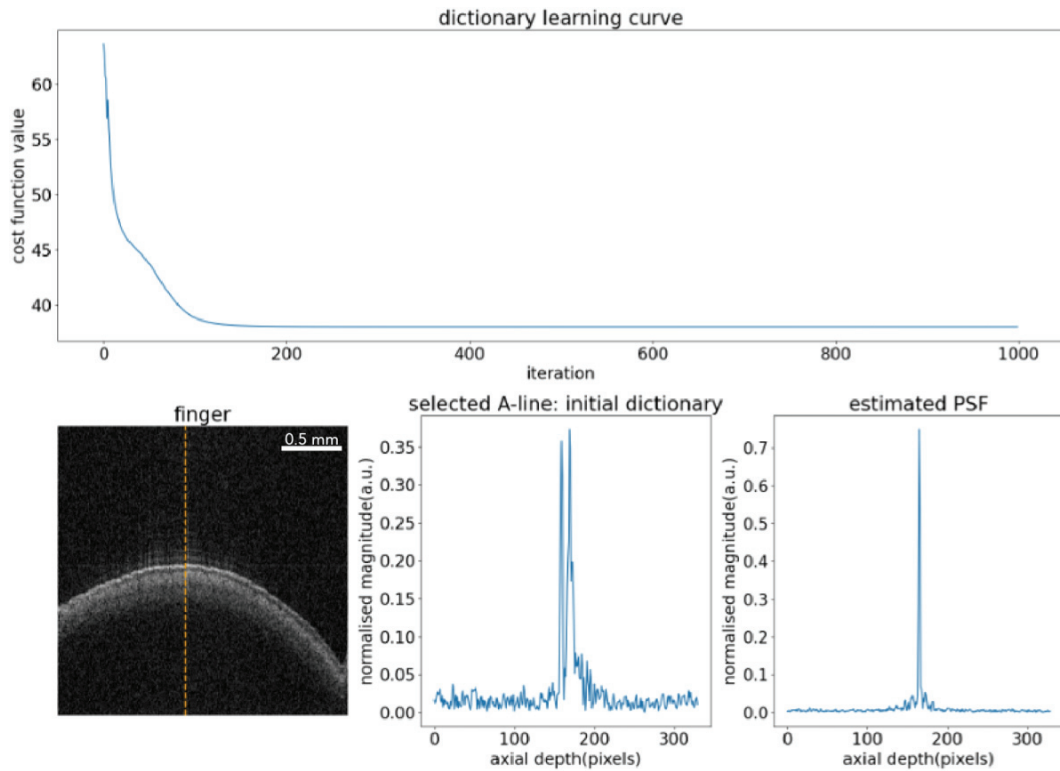
Figure 3.8: In this example of PSF estimation using OCT data, the PSF is estimated from a subset of A-lines within an OCT dataset of a finger image, with one particular A-line (indicated by a dashed orange line) serving as the initial guess[a].

Figure 3.9 illustrates a comparison between the PSF estimation from OCT data (as seen in Figure 3.8) and the PSF measured in Figure 2.16. The estimated and measured PSF were taken in different experiments performed several weeks and so exact agreement cannot be expected between them owing the variation introduced by environmental factors and differences in stitching errors across laser calibration. Despite the lack fo

---

[a] The image shows in Figure 3.8 and all images presented in this paper suffer from fan-beam distortion which mean that the scalebars used are only approximate. Although our group developed a set of correction algorithms to remove fan-beam distortion from OCT images collected with this system, these algorithms were not available at the time this work was performed [135].

detailed agreement, the general shape of the two PSFs is similar. Both the measured and learned PSFs exhibit small yet discernible sidelobes when viewed on a linear scale. These sidelobes become even more pronounced when the PSFs are presented on a logarithmic scale. The difference in the PSF-background values between them is minimal, at only 0.86 dB, while the PSF-sidelobe values show a substantial difference of 12.23 dB. Differences between the measured and estimated PSFs stem from the fact that the precise shape of the PSF changes with each laser calibration. This is largely attributed to stitching errors, which are sensitive by factors such as temperature fluctuations and other environment factor changes. Consequently, every recalibration of the laser leads to alternation in laser operational parameters. These differences emphasize the importance of learning the PSF from image data since a PSF recorded at an earlier time and using a different calibration likely doesn't provide a good representation of the current PSF and so may prove ineffective if used in deconvolution.
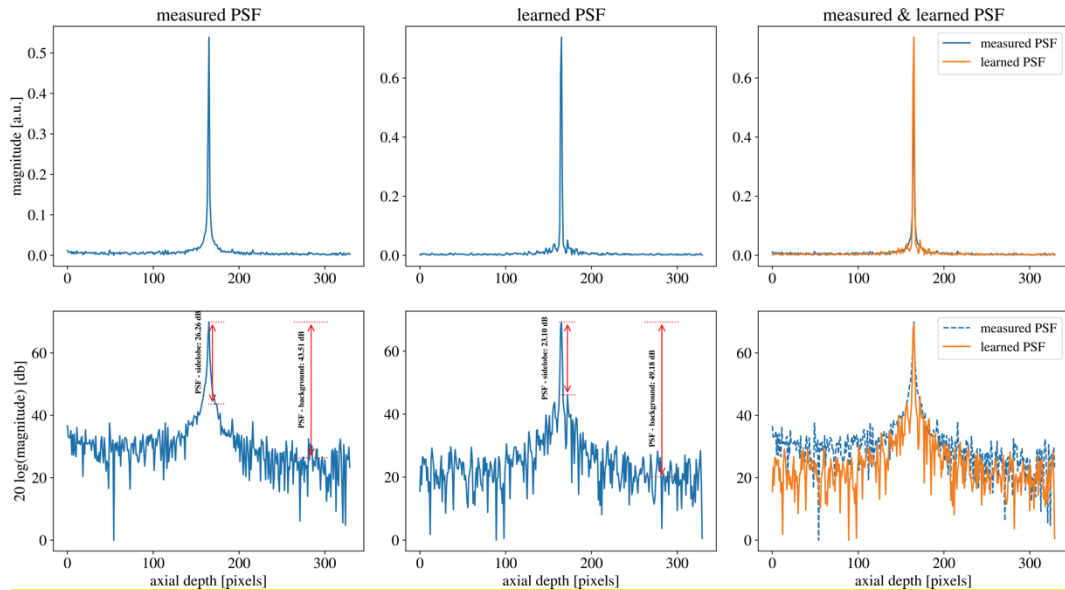
Figure 3.9: From left to right: measured PSF, learned PSF, and an overlay of the learned PSF on the Measured PSF. The top row illustrates the magnitudes of the PSFs on a linear scale, while the bottom row represents them on a logarithmic scale. The measured PSF was derived from the setup depicted in Figure 2.16. For the measured PSF, the PSF-sidelobe and PSF-background values are 26.26 dB and 43.51 dB respectively. In contrast, the learned PSF has PSF-sidelobe and PSF-background values of 23.10 dB and 49.18 dB. Notably, the PSF-background values are nearly identical, but the PSF-sidelobe values significantly differ between the two on the logarithmic plot.

In what follows we refer to $d(z) * x'(z)$ as the sparse estimate of the A-line and we construct the sparse estimate image from $20 \log_{10} \|d(z) * x'_k(z)\|$ where the lateral

location is indexed by k. We refer to $\boldsymbol{x}'(z)$ as the sparse vector estimate of $\alpha(z)$, i.e., of the complex tissue scattering amplitudes. We form the sparse vector image as $20 \log_{10} \|\boldsymbol{x}'_k(z)\|$. The sparse vector image is the final output from our proposed processing method.
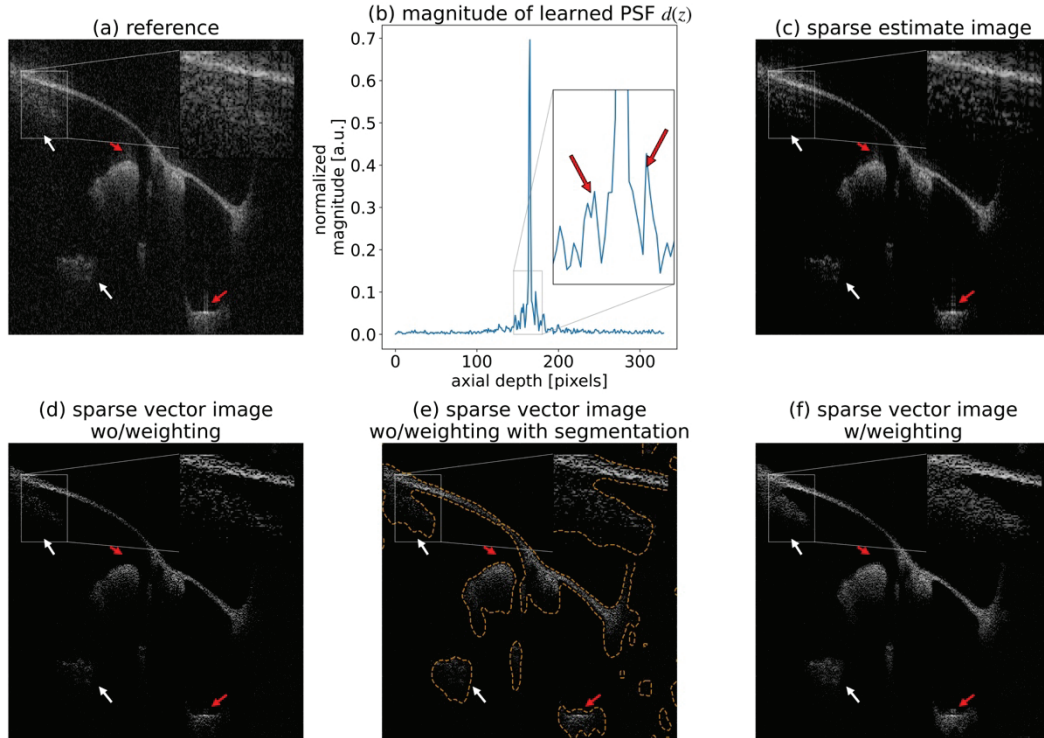
Figure 3.10: Example of applying the proposed processing to an OCT image of a human middle ear. (a) reference image with only standard OCT processing applied. (b) The magnitude of the point spread function $\boldsymbol{d}(z)$ learned over a subset of 128 lines within the 512-line image by solving the CDL minimisation problem of (3.8) with $\lambda = 0.1$. The regularisation parameter λ determines the relative weighting between the fidelity and sparsity terms, as suggested in (3.6). (c) the sparse estimate image $\boldsymbol{d}(z) * \boldsymbol{x}'(z)$ obtained by solving the weighted CSC minimisation problem of (3.7). (d) the sparse vector image obtained from CSC with $\lambda = 0.05$ and without l_1 weighting (i.e., with $W(z) = 1$ everywhere). (e) sparse vector image from (d) segmented into the tissue-containing regions using Sobel filter-based edge detection (highlighted with dashed orange overlay). (f) sparse vector image obtained by solving (3.7) with $W(z) = 0.1$ in the segmented regions of (e), and $W(z) = 1$ elsewhere with a transition from $W(z) = 0.1$ to $W(z) = 1$ taking place over 20 pixels in the regions distal to each segmented region. In all images, red arrows indicate the sidelobe artefacts and white arrows highlight tissue regions of interest.

Figure 3.10 shows an example of applying the proposed processing to an OCT image of a human middle ear. All images in this study are displayed on the same intensity scale with a 50dB dynamic range [141]. Figure 3.10 (a) shows a reference image which is

affected by sidelobe artefacts proximal to brightly reflecting middle ear structures (indicated by the red arrows) as well as background noise. White arrows show weakly reflecting structures in the image. Figure 3.10 (b) shows the learned PSF obtained by solving the CDL problem of (3.8) and highlights the sidelobes (red arrows) that contribute the artefacts in Figure 3.10 (a) and Figure 3.10 (c). The insets highlight a region of the image where these artefacts are sufficiently severe to completely obscure an empty region between the tympanic annulus and tympanic bone.

Figure 3.10 (c) shows an image generated from the sparse estimate $\boldsymbol{d}(z) * \boldsymbol{x}'(z)$ obtained from solving the CSC problem with the learned PSF. The sparse regularisation l_1 term of (3.6) drives a substantial reduction in the background noise as $\boldsymbol{x}'(z)$ is made sparse within the empty regions in the proximal and distal portions of the image. At the same time, the fit $\boldsymbol{d}(z) * \boldsymbol{x}'(z)$ achieves high fidelity with both the tissue structure and the sidelobe artefacts. Figure 3.10 (d) - (e) depict the influence of applying a spatially weighted mask on the l_1 term, as denoted in (3.7). This procedure preferentially reduces the overall contribution of the sparsity term to the cost function, while keeping the value of λ constant in regions devoid of structure. Figure 3.10 (d) shows an image constructed from the sparse vectors $\boldsymbol{x}'(z)$ without applying an l_1 weighting factor (i.e., with $W(z) = 1$) and with $\lambda = 0.05$.

In this image, the sidelobe artefacts are highly suppressed because they are contained entirely in the learned PSF $\boldsymbol{d}(z)$ and not in the sparse vectors $\boldsymbol{x}'(z)$. In the top left quadrant of the image (highlighted in the inset), the empty region that was completely obscured by these sidelobe artefacts in Figure 3.10 (a) and Figure 3.10 (c) is revealed in the sparse vector image of Figure 3.10 (d). However, in the tissue-containing regions, many pixels have been set to zero intensity by the sparse optimisation process to increase the sparsity of the solution, resulting in loss of speckle brightness in the tissue regions.

This is an example of a central problem in applying sparsity-based image processing to images that contain strong speckle, such as OCT or ultrasound images [174]. Because the speckle makes the tissue regions non-sparse, the sparsity-based optimisation will tend to set low intensity pixels in the speckle to zero intensity in the sparse vectors $\boldsymbol{x}'_k(z)$, potentially causing a loss of diagnostically useful information. While it would be possible to apply despeckling prior to deconvolution, the non-linear

nature of the despeckling process would destroy the convolutional structure of the OCT image resulting in a lower fidelity deconvolution.

An alternate approach to mitigating the loss of speckle brightness is to apply a spatially dependent weighting factor $W(z)$ to the l_1 term in (3.7) that determines how heavily sparsity will be weighted in different regions of the image. If coarse image segmentation is applied to the image to roughly determine the extent of speckle-containing tissue regions, then this segmentation can be used to weight sparsity less heavily in regions containing tissue as compared to regions that do not contain tissue.

To apply this approach, we first obtained sparse vectors $\boldsymbol{x}_k'(z)$ at a fixed $\lambda = 0.05$. These sparse vectors were nearly free of sidelobe artefacts due to the deconvolution of the PSF. However, they also suffered from loss of speckle brightness. We then segmented the sparse vector image for tissue structure by performing opening (erosion followed by dilation), median filtering and Sobel filter-based edge detection [151]. Other common segmentation approaches would serve equally well. The resulting segmentation contours can be seen in orange overlay in Figure 3.10 (e). We defined a hard step in the weight map $W(z)$ at the proximal interface of each structure with a value of $W(z) = 1$ proximal to the interface and $W(z) = 0.1$ distal to the interface. Because in middle ear OCT images, the distal boundary of structures is not well defined, a tapered weight was used at the distal interface of each structure. From the distal interface obtained from Sobel-filter segmentation, the weight $W(z)$ was increased linearly over 20 pixels until it equaled 1.

Figure 3.10 (f) shows the result of performing a second pass of the CSC optimisation (i.e., solving (3.7)) with this weighting mask(orange overlay seen in Figure 3.10 (e)) In this final image, the artefacts remain well-suppressed, but without the loss of tissue brightness seen in Figure 3.10 (d).
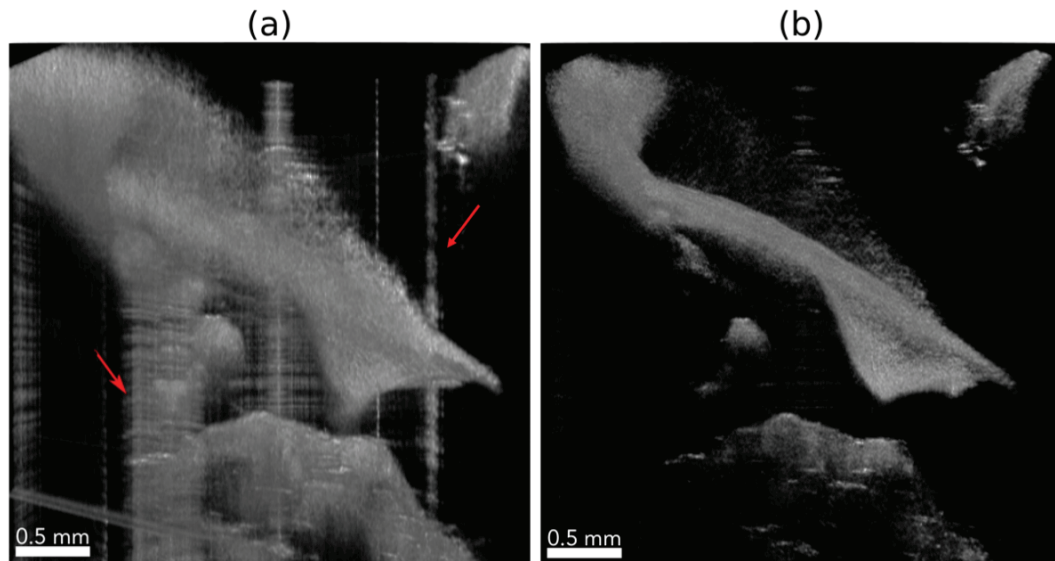
Figure 3.11: (a) 3D volumetric OCT image of a human middle ear processed using the standard processing of Figure 3.7. The red arrows indicate strong sidelobe artefacts arising from bright specular reflections from the tympanic membrane. (b) The same volume processed using the proposed processing on a slice-by-slice basis displayed with the same dynamic range. Sidelobe artefacts are well suppressed. The shown scalar bar might not be geometrically accurate at the time of this manuscript's publication.

Figure 3.11 shows the results of applying this process to a full volumetric dataset of a human middle ear. Processing the data using standard processing (Figure 3.11 (a)) results in prominent sidelobe artefacts wherever strong, specular reflections occur (red arrows) which obscure structures behind the artefact and clutter the image. More subtly, sidelobe artefacts introduce a haze around all structures at air-tissue boundaries and make thin structures like the tympanic membrane (TM) appear thicker than they are. Figure 3.11 (b) shows the results of applying the proposed blind deconvolution method on a frame-by-frame basis within the volume. The sidelobe artefacts are well suppressed and previously obscured structures become visible. The TM appears thinner because it is no longer being axially smeared out by the PSF. Figure 3.11 is a still frame of a 3D volumetric OCT of a healthy volunteer which shows the standard-processed and deconvolved volumetric datasets being rotated.

3.7   Performance assessment

A wide range of image quality metrics have been used in evaluating OCT image processing algorithms, particularly despeckling algorithms. The structure similarity index

measure (SSIM) [205] measures similarity between a gold standard image and a processed image to determine similarity. It is not an effective measure of the quality of deconvolved images because there is no gold standard image to compare the sparse vector image to. Edge preservation index (EPI) [168] measures the edge distortion and equivalent number of looks (ENL) [206] is a measure of the smoothness of an image within a region of interest (ROI). While useful in evaluating despeckling algorithms, these metrics are of little use in evaluating deconvolution algorithms since deconvolution tends to decrease smoothness by making features better defined, by increasing the apparent resolution of structures [148], [150] and by increasing speckle variance [148]. As a result, EPI and ENL scores will nearly always be worse for sparsely deconvolved images, even when these images are perceptually better at capturing the underlying tissue reflectance than the original image.

Given the limitations of these image quality metrics for our use case, we opted to quantitatively assess the performance of our CDL processing pipeline using three simple metrics that have previously been used to evaluate deconvolution algorithms for OCT and/or ultrasound imaging, the SNR [148] the contrast (C) [207] and the generalised contrast-to-noise ratio (gCNR) [208]. In applying these metrics, we compare the image produced using the proposed CDL-based sparse deconvolution and a standard-processed reference image.

SNR is defined as the ratio of mean intensity in a ROI containing structure to the standard deviation of intensity in a background region free from structure or sidelobe artefacts:

$$SNR = 10 \log_{10} \frac{\mu_h}{\sigma_b} \tag{3.27}$$

where μ_h and σ_b represent the mean intensity (in linear units) of a tissue-containing region and standard deviation of intensity in a background region.

Contrast measures the ratio of mean image intensity between two ROIs within the image (e.g., regions H_1 and H_2 in Figure 3.16):

$$C = 10 \log_{10} \frac{\mu_{r_1}}{\mu_{r_2}} \tag{3.28}$$

$gCNR$ is a bounded metric ranging from 0 to 1 that quantifies distinguishability in terms of the Bayesian probability of correctly assigning a given pixel to one of two defined regions using a threshold-based binary classifier [209]. gCNR is insensitive to changes in speckle statistics and to the image's dynamic range. To a good approximation, gCNR is a simple function of the overlap integral between the greyscale intensity histograms of two ROIs. A gCNR close to unity indicates that two ROIs can be distinguished with a high confidence and that their intensity histograms are nearly non-overlapping while two regions with gCNR close to zero are nearly indistinguishable and have highly overlapping intensity histograms. Because of its basis in an operational, Bayesian definition of distinguishability, gCNR offers a valid way of assessing change to distinguishability between two regions that is free of any assumptions about the speckle statistics [209]. $gCNR$ is given by:

$$gCNR = 1 - \sum_{k=0}^{N-1} \min\left(r_1(x_k),\, r_2(x_k)\right) \tag{3.29}$$

where $r_1(x_k)$ and $r_2(x_k)$ are normalised log-intensity histograms on the $N = 256$ greyscale levels x_k of the pixels within the 50dB display dynamic range in the regions 1 and 2.

3.8   Results and discussions

Figure 3.12 shows the results of applying the proposed processing to in vivo OCT images of a human middle ear, the palmar aspect of a fingertip, the side aspect of a fingertip, and an onion. All images were processed with a fixed $\lambda = 0.1$ for the CDL step, followed by the two-pass CSC processing method shown in Figure 3.7 with a value of λ selected heuristically for each image to achieve the best perceptual image quality. The top row shows the reference images, processed using the standard processing method. The bottom row shows the results of applying our proposed processing method.

The values of the regularisation parameter λ and weighting factor $W(z)$ are given above each image. Qualitatively, in all images, both the sidelobe artefacts (indicated by white arrows) and the background noise level are substantially reduced in the sparse vector images while the contrast of speckle and tissue boundaries is enhanced. These

improvements are achieved without noticeable loss of anatomical structure, even for structures that are weak in the reference images.
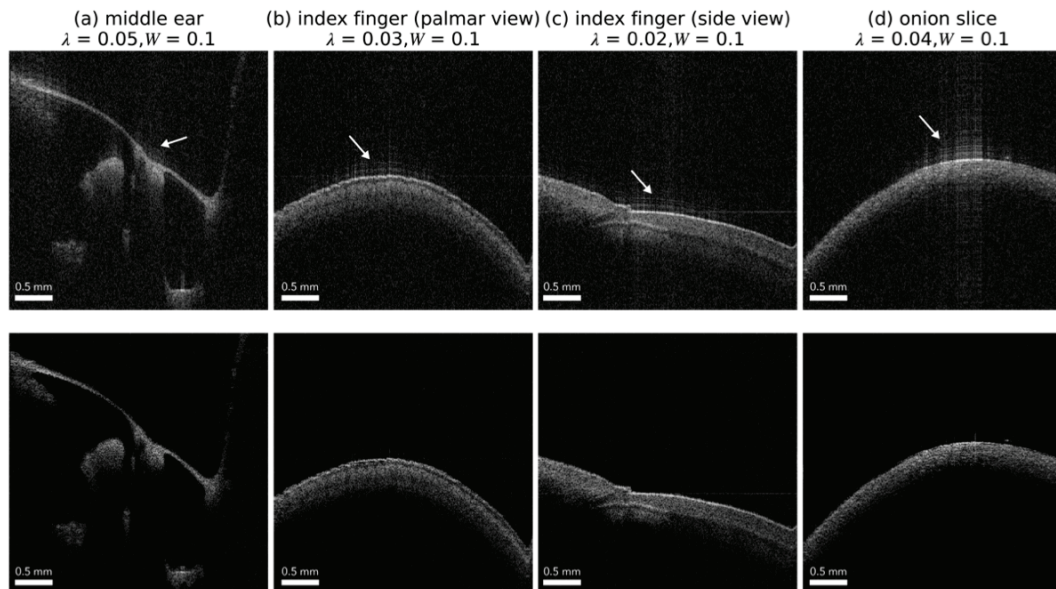
Figure 3.12: From left to right: OCT images of a middle ear, index finger (palmar view), index finger (side view), and onion slice. The top row shows the reference image with only standard processing applied while the bottom row shows the corresponding sparse vector images obtained from the proposed two-pass sparse processing shown in Figure 3.7. The white arrow indicates the sidelobe artefacts caused by the PSF. The shown scalar bar might not be geometrically accurate at the time of this manuscript's publication [144]. The images, as presented, do not accurately portray the true geometric dimensions. This distortion mainly originates from the incorrect mapping of spherically acquired data into Cartesian display space. By the time this thesis was prepared, this geometric distortion had been appropriately addressed [135].

For a $512(w) \times 330(d)$ pixel image, the CDL solver took 750 iterations and 18 seconds to estimate the PSF from 128 A-lines on a 2019 MacBook Pro with a 2.4-GHz Intel i9-9980HK processor and 32-GB of 2400 MHz DDR4 memory. Following dictionary learning of the PSF, the CSC problem was solved using the learned PSF to estimate all 512 image lines on the same computer in a total time of 1.28 seconds. Given the fundamental parallelism of line-by-line based image deconvolution, the computation time of both CDL and CSC could be improved substantially by using parallel processing employing graphics processing unit (GPU) acceleration [202], although that was not explored in this study.

3.8.1 Selection of regularisation parameter and l_1 weighting

Within the proposed processing method, the regularisation parameter λ controls the relative weighting of sparsity and fidelity in the CSC and CDL cost functions while the weighting factor $W(z)$ controls the amount of structure loss in regions identified as structure-containing during segmentation of the sparse vector image from the first CSC pass. While an appropriate value of λ can be selected empirically, this process is subjective and labour intensive and so an automatic method for narrowing down the range of λ is preferrable. We chose λ by identifying a region of the image that was known to be free of structure (e.g., the dashed portion of the orange line in Figure 3.13) and then performed a grid search over a logarithmically spaced grid on $\lambda \in [10^{-5}, 10^2]$.
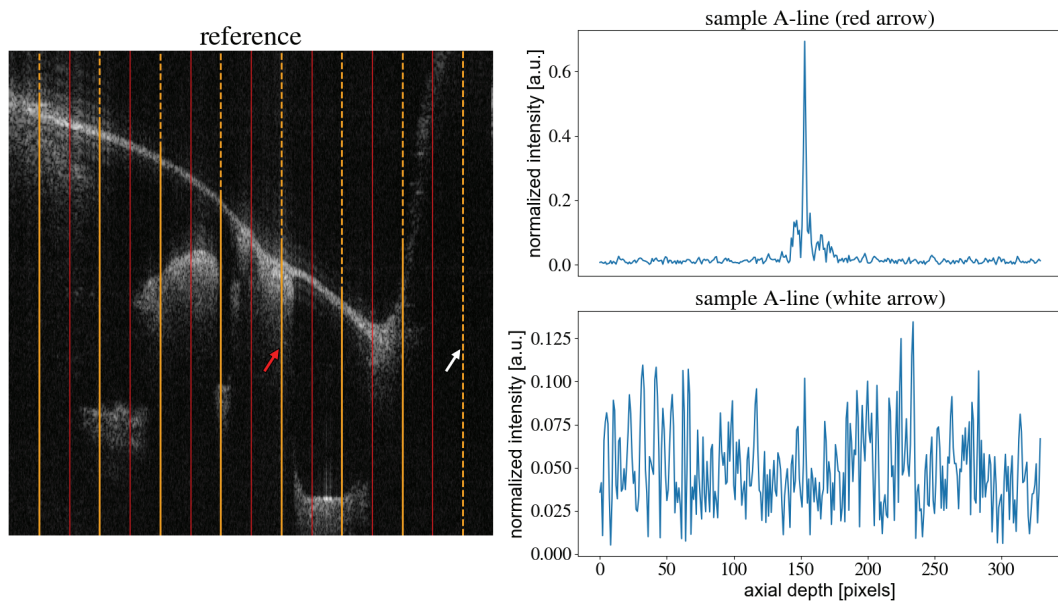
Figure 3.13: Eight λ were approximated by setting structure-free region (dashed portion of the orange line) to be zero. The red arrow indicates where the minimum λ (0.035) was found, and the white arrow indicates where the maximum λ was found (0.40).

We selected the smallest λ for which all points with the structure-free region of the sparsely estimated line were zero. Here we separated the A-line data horizontally into eight evenly spaced patches (e.g., red solid lines), and chose the center line from each patch as the signal A-line for performing a λ grid search. Sparsity is a property of the class of A-lines being analysed [161]. Because of this, even within an image there may be different optimal values of λ for different A-lines. For example, in Figure 3.13 we found that our method gave a value of $\lambda = 0.035$ at the A-line indicated by the red arrow

containing bright discrete structures. In contrast, a value of $\lambda = 0.40$ was found by this method at the location indicated by the white arrow where the A-line contains mostly noise. In principle, a different value of λ could be used to deconvolve A-lines at different lateral locations within the image, although in this study we generally applied the same value of λ across all image lines. An optimal starting point for the λ range across all 10,240 A-lines was established by computing the average of λ values derived from a representative sample of eight chosen A-lines with even spacing in the lateral direction.

Heuristically, we found that λ between 0.01 and 0.05 and $W = 0.1$ gave good qualitative results across the images we investigated, but we also varied both parameters to investigate the trade-offs from using different values in each image set.
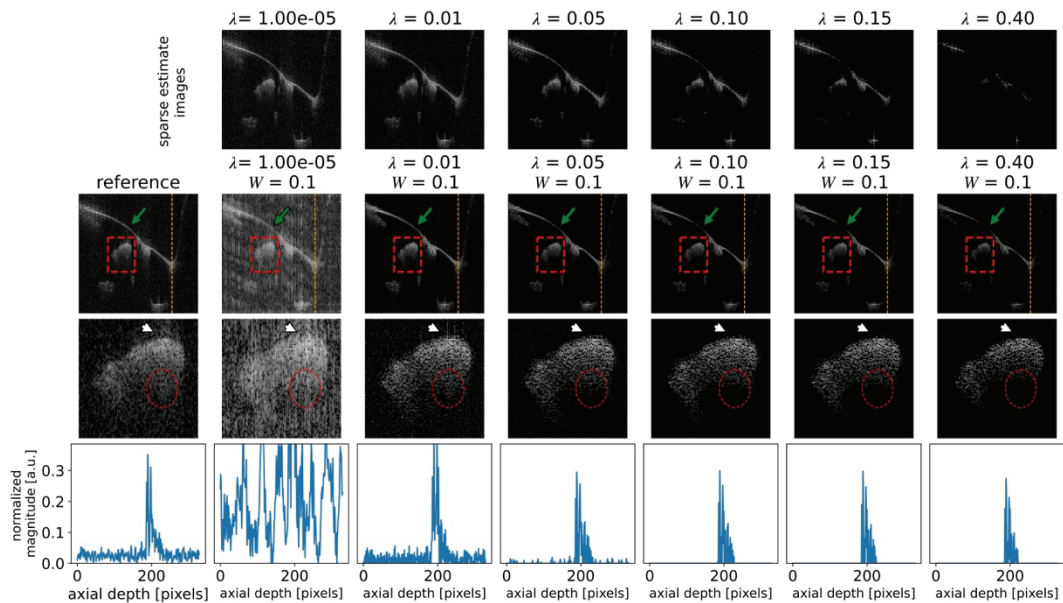
Figure 3.14: Sparse reconstructions of an OCT middle ear image using the same learned PSF for various values of the regularisation parameter λ. The top row shows the sparse estimate images. The second row shows the sparse vector images with the weighting mask applied. The red box highlights a bony tissue ROI (lenticular process of the incus) which is zoomed in the third row. The white arrow indicates the location of sidelobe artefacts appearing in the reference image and suppressed in the sparse images. The dashed red circle highlights a weakly reflecting speckle region at the distal side of the ROI where a loss of structure can be seen as the value of λ increases. The green arrow highlights a region of the tympanic membrane that is completely eroded away in the high λ images. The bottom plots show the A-line magnitude along a selected line in the image (orange line in the second-row images) for each value of λ.

Figure 3.14 shows the effects of varying λ from 10^{-5} to 0.40 with $W(z) = 0.1$ for the middle ear image. A tissue structure ROI (red) was selected around the lenticular

process of the incus and zoomed in on in the third row. In the case where $\lambda = 10^{-5}$ the problem of (3.8) is ill-posed. The sparse estimate overfits the reference image and the sparse vector image is a very poor estimate of the underlying structure. In the range $\lambda \in [0.01, 0.15]$ the problem is well-posed, and the solution finds a balance between fidelity and sparsity that results in a good estimate of the underlying structure with sidelobe artefacts suppressed. At $\lambda = 0.01$, some of the sidelobe artefacts (white arrow) and noise from the reference image are retained in the sparse vector image whereas when $\lambda = 0.05$ the sidelobe artefact and noise have been completely removed from the empty regions without noticeable tissue loss relative to the reference images. For $\lambda \geq 0.15$ the algorithm over-weights sparsity causing a loss of tissue speckle brightness (dashed red circle). In one region (green arrow) this loss creates an apparent discontinuity in the tympanic membrane.
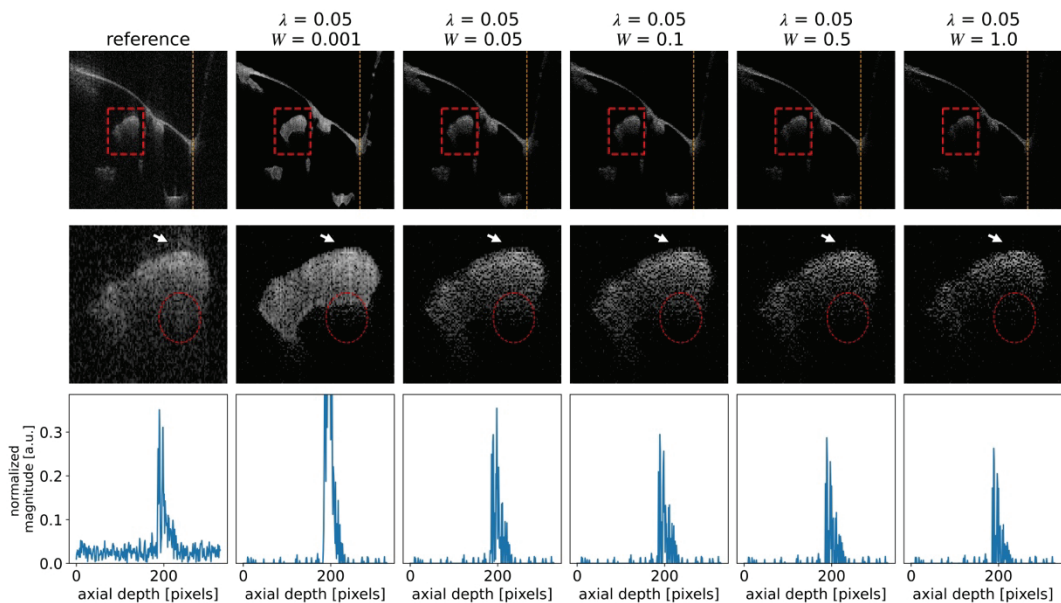
Figure 3.15: Sparse reconstructions of the OCT middle ear image of Figure 3.14 for various values of the weighting factor W at fixed $\lambda = 0.05$. Top row: reference and sparse vector images. A ROI at the lenticular process of the incus is highlighted in the red box. Middle row: zoomed in image of the ROI from the top images. Bottom row: sparse vector A-line estimate along the orange line in the top row images.

Figure 3.15 demonstrates the effect of applying various values of the weighting factors $W(z)$ in the segmented tissue regions with λ fixed at 0.05. Increasing $W(z)$ in the tissue region is equivalent to locally increasing λ and so it also causes progressive loss of

signal intensity and a higher fraction of zero intensity pixels in the tissue region indicated by the dashed red circles.

3.8.2   Sparse optimisation performance

In Figure 3.16, we identified a ROI that contained no structure (cyan, labeled B for background), a ROI that contained no structure but that was contaminated by sidelobe artefacts from a nearby surface (green, labeled A for artefact) and two ROIs that contain tissue speckle (red), a brightly reflecting ROI H_1 and a weakly reflecting ROI H_2.

Our proposed processing improved the SNR of H_2 relative to the background ROI by 2.2 dB and improved the contrast between H_2 and background ROI by 5.8 dB. The processing generally preserved the contrast between tissue regions, with the contrast between H_1 and H_2 changing by only 0.3 dB following processing. gCNR between region H_2 and the background improved modestly from 0.53 to 0.59 and gCNR between region H_2 and the region contaminated by sidelobe artefacts improved substantially from 0.28 to 0.65. However, the sparse processing also caused a substantial decrease in gCNR between H_1 and H_2 from 0.80 to 0.60.

The decrease in gCNR between H_1 and H_2 can be explained almost entirely by an increase in the number of pixels in H_1 with greyscale intensity zero created by the sparse optimisation as can be seen in the intensity histograms in the second row of Figure 3.16. Because in the sparse representation both H_1 and H_2 have a large fraction of zero-intensity pixels, the histograms have substantial overlap (i.e., orange shading) and the resulting gCNR is low. Because the observed decrease in gCNR is due to the zero-intensity pixels, further processing steps that fill in zero-intensity pixels with non-zero intensity (i.e., despeckling operations) can mitigate the decrease. For example, applying a 2D median filter with a 3×3 square kernel to the sparse vector image fills in most of the zero-intensity pixels in the tissue regions and results in a substantial increase in the gCNR between H_1 and H_2 from 0.60 to 0.87 due to the decrement in the number of zero intensity pixels. It therefore appears that a processing sequence consisting of sparse deconvolution followed by despeckling can result in removal of sidelobe artefacts and suppression of background noise without compromising tissue distinguishability.
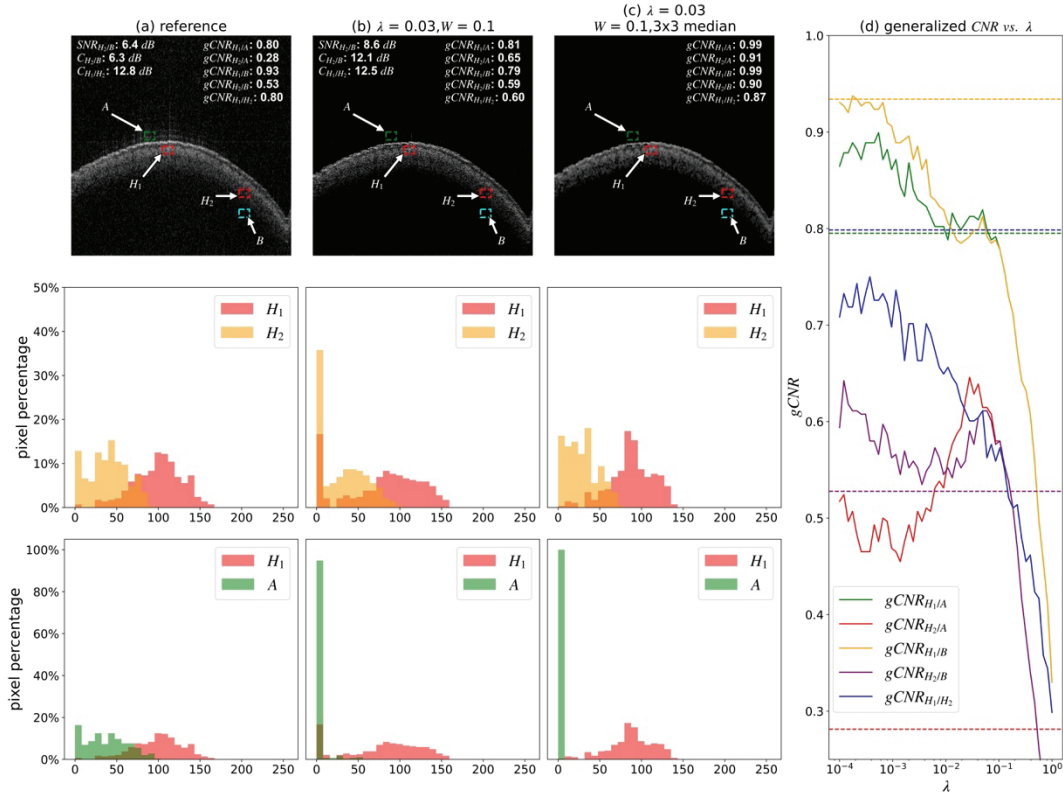
Figure 3.16: Index finger (palmar aspect) images with $\lambda = 0.03$ and $W = 0.1$. The performance of the sparse processing algorithm is assessed within three classes of region of interest (ROIs): background region B (cyan) where there is no anatomical structure, region A (green) containing sidelobe artefacts, a brightly reflective tissue speckle region H_1 (red) and a weakly reflective tissue speckle region H_2 (red). OCT 2D images are shown in the top row and corresponding intensity histograms in the bottom two rows. (a) reference image (b) image after proposed processing (c) image after proposed processing and median filtering with a 3x3 kernel (d) plot of gCNR between the ROIs as a function of the regularisation parameter λ. The dashed lines show the gCNR values calculated for the reference image and the solid lines show gCNR for the sparse vector image as a function of λ, with W held fixed at 0.1.

To study how the gCNR between image regions is affected by the regularisation parameter λ, we applied λ values from 0.0001 to 1 to the index finger (palmar view) image of Figure 3.16 and calculated the gCNR between regions at each λ. For $\lambda < 0.0001$ the regularisation provided by the sparsity term in (3.8) is inadequate and the problem is effectively ill-posed leading to solutions like the one seen in the second column of Figure 3.14. Starting at around $\lambda = 0.0001$, the problem becomes well-posed and the sparse vector image exhibits comparable or improved distinguishability compared to the reference image between the tissue regions, and the background and artefact

regions as measured by $gCNR_{H_1/B}, gCNR_{H_2/B}, gCNR_{H_1/A}$ and $gCNR_{H_2/A}$. As λ increases, all regions become sparser with a greater fraction of their pixels in the zero-intensity histogram bin. The effect of this change on $gCNR$ depends on the regions involved. $gCNR_{H_2/A}$ is improved while $gCNR_{H_1/A}$ and $gCNR_{H_1/H_2}$ decrease due to the overlap of the zero-intensity bin. $gCNR_{H_2/B}$ and $gCNR_{H_2/A}$ both reach their peak at around $\lambda = 0.03$. At around $\lambda = 0.08$, all $gCNR$ values begin to roll off as all regions begin to contain a large fraction of zero-intensity pixels, making them less distinguishable from each other by the gCNR metric. Figure 3.16 (d) supports the heuristic selection of λ in the range 0.01 to 0.05 since, according to the plot, this range offers good artefact suppression while keeping the loss of distinguishability between the two tissue regions due to zero-intensity pixels to an acceptable level.

Traditionally, the main method of addressing sidelobe artefacts in the absence of an independent measurement of the PSF has been through the application of spectral windowing [112] prior to inverse discrete Fourier transformation of the spectral interferogram. While simple to implement and computationally efficient, spectral windowing incurs a trade-off between axial resolution and sidelobe suppression that limits its effectiveness [82].

We compared our proposed method to spectral windowing with two frequently used window functions, the Gaussian window, and the Hann window and to processing without windowing. Figure 3.17 (a)-(c) show images produced with, respectively, no spectral windowing, a Gaussian window with the same length as the raw spectrogram and a standard deviation of 10% of the spectrogram width and a Hann window. The Gaussian window was made narrow to highlight the degradation in axial resolution from windowing. While windowing does reduce the severity of sidelobe artefacts relative to no windowing close to the main lobe, the proposed method, shown in Figure 3.17 (d), significantly outperforms windowing, particularly for artefacts lying 20 pixels or more from the main lobe. The inability of traditional windowing to suppress these artefacts is also highlighted in Figure 3.17 (e) which shows the directly measured axial PSF from a mirror reflector, calculated with various windows applied. While windowing successfully reduces the sidelobes directly adjacent to the main lobes, other lobes, presumably arising from to source spectrum imperfections and/or sweep non-linearity are not suppressed by

windowing. Figure 3.17 (f) shows the spectrogram corresponding to the three PSFs in Figure 3.17 (e).
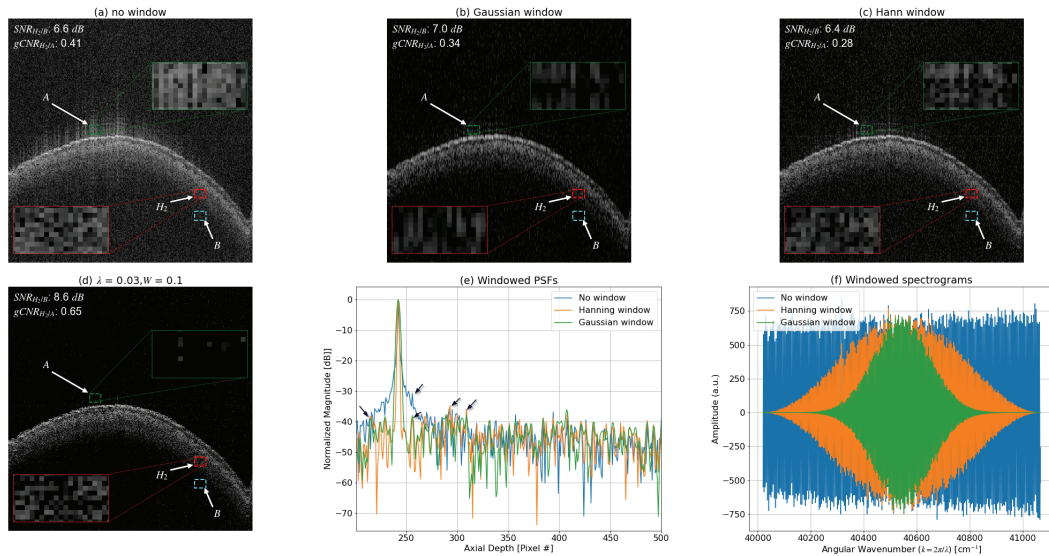
Figure 3.17: Comparison of spectral windowing with CSC for sidelobe artefact suppression for the index finger (palmar aspect) image. Windows are applied on the full 1460 sample spectrograms then truncated to 330 pixels following inverse discrete Fourier transformation. Separately, a mirror reflector was imaged to provide direct measurements of the PSF and corresponding spectrogram. The insets show pixel intensities in regions H_2 and A. (a) image with no spectral windowing applied. (b) Image with Gaussian windowing ($\sigma = 0.10$ of spectrogram width). (c) Image with Hann windowing. (d) proposed convolutional sparse coding method with a PSF learned from the image. (e) Measured PSF from a mirror reflector with no window, Hann window and Gaussian window ($\sigma = 0.10$ of spectrogram width) applied. The arrows indicate features that contribute to the sidelobe artefacts and that are not suppressed by windowing. (f) Spectrogram with no window, Hann window and Gaussian windows applied. The plotted spectrogram is the average over 15,000 laser sweeps. The PSFs in (e) are obtained by inverse Fourier transformation of the spectrograms in (f).

The superior artefact suppression of the proposed method allows it to achieve higher gCNR between the weak tissue ROI H_2 and sidelobe artefact ROI A, and a larger SNR improvement between the weak tissue ROI H_2 and background region B than the windowing methods without noticeable degradation in axial resolution relative to the no-window case. The counterintuitive drop in $gCNR_{H_2/A}$ between Figure 3.17 (a) and Figure 3.17 (b)-(c) can be attributed to the artefact region being brighter than H_2 in Figure 3.17 (a) which makes the two regions more distinguishable than in Figure 3.17 (b)-(c) where they have similar intensities. Figure 3.17 (b) shows the degradation in axial resolution that comes from the use of a narrow Gaussian window. Despite incurring a significant

degradation in axial resolution, the image of Figure 3.17 (b) still shows visible sidelobe artefacts demonstrating the limitations of windowing as a sidelobe suppression technique.

3.9   Conclusion

Blind deconvolution using convolutional sparse coding with dictionary learning is a promising approach for reducing artefacts and noise and for enhancing contrast in OCT images containing bright reflectors where contrast is limited by sidelobe artefacts from the PSF. For a fingertip image, we demonstrated an SNR improvement of 2.2 dB and a contrast improvement of 5.8 dB within a region affected by PSF sidelobes while only incurring a 0.3 dB contrast change between a brightly reflecting and a weakly reflecting tissue region. The proposed processing also improved the generalised contrast-to-noise ratio between tissue and background, and between tissue and artefact regions, but reduced gCNR between the bright and weak tissue regions due to the introduction of zero-intensity pixels into the speckle in the bright tissue region. We showed that this effect can be largely mitigated by applying a despeckling step (e.g., median filtering) after deconvolution.

We believe this to be the first demonstration of blind deconvolution of complex OCT A-lines. Unlike previously described deconvolution methods for OCT, the improvements in image quality we obtain do not require us to obtain an independent measurement or model-based estimate of the PSF. Rather, a complex valued, axial PSF is learned from the complex OCT A-lines acquired during imaging. This makes the method particularly well-suited to OCT systems in which the PSF changes with time because dictionary learning can continuously update its estimate of the PSF from OCT imaging data without requiring any additional calibration steps. The stability of the PSF will depend on the details of the source and interferometer design of each OCT system. In our swept-source system we found that the PSF estimate could be used to effectively suppress sidelobe artefacts over a period of tens of seconds before requiring updating. It also makes the method applicable to previously collected image data, so long as the complex line data or the spectrogram data was retained.

Our current CSC processing rate of 2.5ms/line (1.28s for a 512-line image) is suitable for many near-real-time image post-processing applications such as post-

rendering for 3D visualisation, image segmentation and feature extraction. Further improvements to speed using GPU accelerated algorithms could plausibly make the method compatible with real-time, video-rate 2D processing for OCT images of typical size. While CDL is a slower step (18s for 128 lines) than CSC, it only needs to be performed periodically and so it may also be compatible with real-time processing rates with GPU acceleration. For real-time processing, a modified form of the CDL problem that performs continuous and efficient updating of the PSF estimate called online CDL may be applied [210].

Effective use of convolutional sparse coding requires the appropriate selection of the regularisation parameter λ and l_1 weighting factor W. While this optimisation was done heuristically in this study, performance was only weakly dependent on the exact values chosen and values of λ in the range of 0.01 to 0.05 and $W = 0.1$ worked well across the various images we tested.

The removal of sidelobe artefacts and noise from OCT images containing bright reflectors is an important step for allowing advanced visualisation and analysis steps including 3D volumetric visualisation, automated segmentation, and automated diagnostics. Blind deconvolution through convolutional sparse coding with dictionary learning could prove to be an important image processing technique for many OCT applications.

3.10 Data available statement

Data and computer source code used to generate the results presented in this chapter are available in [203].

Chapter 4

Optical clearing agents for optical imaging through cartilage tympanoplasties: a preclinical feasibility study

Junzhe Wang,[1] Gaurav Chawdhary,[2] Xiaojie Yang,[1,3] Francis Morin,[4] Mamoona Khalid-Raja,[5] Joshua Farrell,[1] Dan MacDougall,[1] Fangyi Chen,[3] David P Morris,[6] Robert B A Adamson[1,6,7]

[1] School of Biomedical Engineering, Dalhousie University, Halifax, Nova Scotia

[2] Department of Otolaryngology, Royal Hallamshire Hospital, Sheffield, United Kingdom

[3] Department of Biomedical Engineering, Southern University of Science and Technology, Shenzhen, Guangdong, China

[4] Family Medicine, McGill University, Montreal, Quebec

[5] Stepping Hill Hospital, Stockport NHS Foundation Trust, Great Manchester, England

[6] Division of Otolaryngology Head & Neck Surgery, Department of Surgery, Dalhousie University, Halifax, Nova Scotia

[7] Electrical and Computer Engineering Department, Dalhousie University.

4.1   Author contribution statement

J. Wang and R. Adamson worked together to develop the research methods and design the experiments for this study, with R. Adamson offering additional support in drafting the manuscript. G. Chawdhary and D. Morris contributed by establishing the clinical relevance of the study and preparing cadaver specimens for the imaging sessions. X. Yang provided support for the experimental work.

F. Morin and M. Khalid-Raja were involved in the early stages of verification and research method development, while J. Farrell assisted with the development of 3D rendering software. D. MacDougall played a key role in designing the OCT image system. F. Chen offered financial support for the project. All authors provided valuable feedback during the manuscript drafting process.

J. Wang was responsible for carrying out the experiments, conducting the data analyses, and serving as the lead author for the journal submission.

4.2 Preamble

This chapter is primarily based on my second peer-reviewed publication [131], with its core content remaining largely unchanged. However, to avoid redundancy, any introductory information that overlaps with Chapter 1 has been omitted or revised for the sake of brevity. I have taken the opportunity to include some unpublished experimental details and made adjustments to ensure consistency in terminology, style, and the presentation of results throughout the document.

In particular, the introductory section has been restructured to offer a clearer understanding of the motivation and novelty of the work at the time the original manuscript was submitted for peer review. This revision also highlights how the research fits into the broader narrative of my thesis. Detailed explanations about the origins of the sidelobe and its impacts can be found in the preceding sections of the document. These modifications serve to enhance the overall coherence and flow of the chapter, providing readers with a comprehensive and self-contained account of the research.

4.3 Summary

Hypothesis: Optical clearing agents (OCAs) can render cartilage tympanoplasty grafts sufficiently transparent to permit visualisation of middle ear structures in the operated ear with optical coherence tomography imaging.

Background: Optical coherence tomography (OCT) is an emerging technology with potential clinical relevance to middle ear imaging. A significant application for middle ear OCT is in the assessment of middle ear reconstructions after surgical tympanoplasty. However, the optical opacity of autologous graft materials used in tympanoplasty creates challenges for OCT and other optical imaging modalities in visualising the middle ear space.

Optical clearing agents (OCAs) are biocompatible agents that can reduce optical scattering in tissue and increase its transparency. In this study we investigate the use of

glycerol as an OCA to reduce the opacity of cartilage grafts to allow OCT visualisation of middle ear structures following cartilage tympanoplasty.

Methods: We cut $N = 5$, $400\mu m$-thick pieces of human tragal cartilage, like those used in tympanoplasty, and treated them with anhydrous glycerol, a commonly used optical clearing agent. A reference reflector was imaged through the tympanoplasty as it cleared at 1 minute time intervals using an OCT imaging system centered at 1550nm. The signal reflected from the reference reflector was measured as the tympanoplasty optically cleared over the course of 7 minutes. The reversibility of clearing and the dimensional changes associated with glycerol absorption were also measured in these samples. In a separate experiment, a human cadaveric temporal bone was prepared to simulate an ossiculoplasty surgery with cartilage replacement of the tympanic membrane. The tympanic membrane and incus were removed, and a partial ossicular replacement prosthesis (PORP) was implanted onto the stapes superstructure. A $400\mu m$ cartilage graft was placed over the prosthesis. The preparation was imaged before and after treating the cartilage graft with glycerol and the visibility of the prosthesis head under OCT imaging was assessed.

Main Outcome Measure: In the in vitro experiment we report the rate of decrease in optical attenuation of the cartilage graft over 7 minutes, the time taken to reach maximal optical transparency and the total decrease in attenuation. We also report on the change in cartilage sample dimensions as measured under microscopy due to glycerol absorption and on the reversibility of dimensional and optical effects of glycerol absorption following washout in saline. For the cadaveric preparation we report the increase in SNR and contrast between the prosthesis head and the background and show 2D and 3D images of the prosthesis through the graft before and after optical clearing.

Results: Following treatment with glycerol, the reflectance of the reference reflector seen through the cartilage graft increased linearly at a rate of 2.3($\pm$ 1.1) dB/min to reach its maximum signal increase of 13.6($\pm$5.9) dB after 7.2($\pm$2) minutes. Following washout of the cleared graft in a saline bath for 10 minutes, the reference reflector signal intensity returned to baseline, confirming that the clearing effect induced by glycerol is reversible.

Glycerol absorption caused a 31($\pm$ 6) % reduction in cartilage sample area which was also reversible following saline washout. In the human cadaveric temporal bone preparation, treatment of the cartilage graft with glycerol resulted in a 13 dB increase in signal-to-noise ratio and a 13 dB increase in contrast. This improvement in visibility was clinically significant as it allowed clear visualisation of a middle ear prosthesis through the graft which could potentially be used to assess postsurgical prosthesis migration or fixation.

Conclusions: Our results demonstrate that optical clearing agents offer a potential pathway towards optical coherence tomography imaging of the middle ear in post-surgical ears with cartilage grafts. The degree of optical clearing achieved in <10 minutes is adequate to enable visualisation of middle ear structures that were not clearly visible prior to clearing. The treatment time needed to achieve transparency was short enough to be compatible with clinical applications. The reversibility of the technique and the observed level of shrinkage appear consistent with safe use in patients.

4.4   Introduction

One of the most promising applications of ME-OCT is in postsurgical assessments of middle ear function following tympanoplasty, with or without middle ear reconstruction. In many procedures that involve tympanoplasty there is a risk of postsurgical complication or of poor outcomes. For example, in ossiculoplasty, which usually involves tympanoplasty as a final step, only 72% of patients obtain a postsurgical air-bone gap less than 20dB [211]. When hearing is assessed postoperatively, clinicians are keen to know whether any persisting hearing loss is due to implant displacement, poor contact, or the effects of fluid or scarring. This information is useful as it impacts the likelihood of success with revision surgery [212]. Computed tomography (CT) is of limited use in evaluating such cases because of its poor contrast for soft tissue and fluid and because of artefacts caused by the presence of implants in reconstructed ears.

4.4.1 OCT imaging with tympanoplasty

When a perforation in the TM occurs, its integrity becomes compromised, leading to an increased risk of chronic otitis media (COM) [128] and impaired sound transmission, as pathogens can enter the middle ear through the external auditory canal. In these situations, reconstructing the TM through procedures such as myringoplasty or tympanoplasty offers two significant benefits: restoring hearing by repairing the perforated TM and preventing recurrent infections.

Myringoplasty [77], [213], a relatively simple procedure often performed in clinics, involves placing a graft, fat, or a temporary seal over the perforation to promote the natural healing processes of the remnant TM. This technique is typically effective for small perforations. In contrast, tympanoplasty is regarded as a more invasive procedure [61], [214], [215], often requiring the lifting of the tympanomeatal flap. Over the years, various surgical techniques have been developed, such as lateral graft tympanoplasty and butterfly tympanoplasty. Moreover, tympanoplasty frequently serves as the final step in middle ear reconstructions that necessitate the replacement or reinforcement of the TM to avoid prosthesis extrusion.

There is a wide variety of graft materials used in myringoplasty or tympanoplasty procedures, ranging from autologous materials [216], which are often harvested from the patient during surgery, to semi-synthetic materials [215]. The most commonly utilised autologous grafts includes temporalis fascia, tragal cartilage, perichondrium, periosteum, fat, or skin [61], [216]. Choosing the appropriate graft material and surgical technique is crucial for ensuring successful outcomes for patients with TM perforations [61]. The differences in material properties may impact the conductive pathway of hearing [61], [216], potentially resulting in extended healing times and an increased likelihood of requiring surgical revisions.

Autologous cartilage is a robust and widely used material for tympanoplasty. Cartilage offers lower rates of retraction and resorption without compromising hearing outcomes as compared with more traditional graft materials like fascia [214], [216]. Cartilage is usually harvested from the patient's tragus or cymba concha and is cut and carved to the desired dimensions and thickness in the operating room (OR).

In cases where tympanoplasty results are sub-optimal, optical coherence tomography's high soft tissue contrast, high resolution, and ability to detect sound-induced motion could be very helpful in investigating the issue. Unfortunately, the optical opacity of autologous graft materials, particularly cartilage, prevents us from obtaining OCT images of structures medial to the graft.
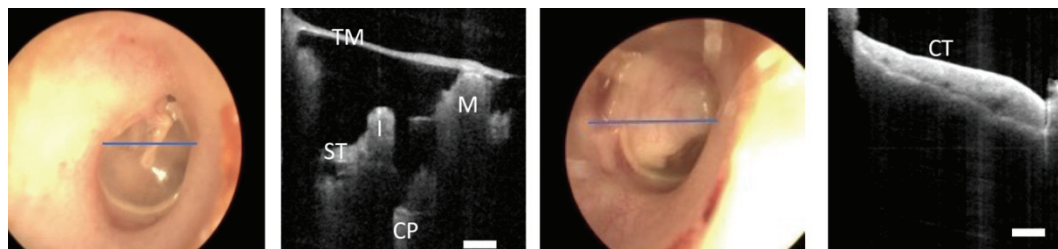
Figure 4.1: From left to right, (a) microscopic image of a normal tympanic membrane. The blue line indicates the plane of optical coherence tomography (OCT) image (b) OCT image of a normal middle ear showing the tympanic membrane (TM), malleus (M), incus (I), stapedius tendon (ST), and cochlear promontory (CP) (c) microscopic image of a cartilage tympanoplasty, (d) optical coherence tomography image of a cartilage tympanoplasty (CT). Scale bars are 1 mm.

Figure 4.1 illustrates this problem. Figure 4.1 (a) and (b) show, respectively a microscope image of a normal tympanic membrane and an optical coherence tomography B- mode image of the middle ear seen through it. The malleus, incus, and cochlear promontory are all clearly visible and accessible to OCT-based vibrometric measurements to assess mobility [106]. Figure 4.1 (c) and (d) show, respectively a microscope image of an ear with a cartilage tympanoplasty and the OCT image of the ear. In the OCT image the cartilage graft and its medial mucosalised surface can be visualised, but the opacity of the graft precludes visualisation of any middle ear structures medial to the tympanic membrane (TM) due to the cartilage graft's thickness and high optical scattering cross-section.

4.4.2 Optical clearing agents (OCAs)

Tissue scattering is a complex phenomenon influenced by many factors, including refractive index mismatch among different cellular tissue components, as well as the size, shape, and refractive indices of these components, all of which contribute to scattering. One approach to improving the quality of ME-OCT images, especially in cases of thickened TM resulting from tympanoplasties, is to improve the transparency of these

grafts, allowing for better observation of medial middle ear structures by reducing the amount of light scattering. One technique that can achieve this goal is the use of optical clearing agents (OCAs), which originated in optical microscopy research. OCAs have been found to be effective in improving image quality by extending the imaging depth of optical microscopy through reducing the amount of light scattering.

OCAs are a class of biocompatible chemicals which are applied to turbid tissue to reduce its optical scattering coefficient and increase its transparency [217]. They function by altering the optical properties of tissue, primarily by homogenising the refractive indices of different tissue components. This process minimises the refractive index mismatch between these components, which in turn reduces scattering and permits deeper light penetration into the tissue. There are several types of OCAs that have been developed, that achieve optical clearing in a variety of ways [218]–[221]. Chemical methods, such as delipidation [219], remove lipid contents to reduce refractive index mismatch. Physical optical clearing methods [217], [219], on the other hand, use refractive index matching solutions like glycerol, propylene glycol, and glucose to increase the refractive index of interstitial spaces to better match those of cells.

Cartilage grafts consist of collagen fibers that exhibit complex self-assembled structures and serve as major scattering centers in the tissue [219]. By utilising a high concentration of hyperosmotic agents, such as glycerol ($n = 1.47$, [222], [223]), with a refractive index similar to that of collagen fibers ($n = 1.47 - 1.51$ [222], [223]), it is possible to enhance graft transparency. As glycerol diffuses into the tissue, it displaces water molecules ($n = 1.33$, [223]), which in turn reduces light scattering and increases the tissue's optical transparency. Another approach is mechanical compression [224], which is achieved by applying high compressive mechanical stress to displace local interstitial water. This displacement causes a more uniform distribution of tissue components and a reduction in refractive index mismatch, resulting in decreased scattering and improved tissue transparency.

Each of these methods has its unique advantages and limitations [219], which should be considered accordingly when selecting the most appropriate agent or technique for a given application. In this study, we focus on the application of OCAs using physical optical clearing methods, as delipidation and mechanical approaches can alter the tissue

structure and present challenges for potential in vivo applications with ME-OCT [217], [219], [220].

4.4.3   Application of OCAs in OCT imaging

Most physical optical clearing based OCAs improve tissue transparency through three physical mechanisms [220]. First, they cause osmotic dehydration of tissue resulting in more densely packed tissue. Second, OCAs infiltrate the interstitial space and dehydrate both the interstitial space and intracellular fluids, elevating the index of refraction of tissue and improving index matching to fibrous and lipid microstructures. Third, in collagen-containing tissues like cartilage, OCAs cause partial dissociation of collagen fibrils into microfibrils, thereby achieving reduced scattering through a smaller mean scatterer size [220]. For in-vivo applications, in addition to achieving good optical clearing, OCAs must achieve high levels of biocompatibility, must be reversible and must be capable of being resorbed and excreted from the body. The most commonly used in-vivo optical clearing agents are aqueous solutions of glycerol, polyethylene glycol (PEG), glucose, fructose and other sugars, polypropylene glycol (PPG), and acetic acid or various mixtures of these agents [223]. Most in-vivo use of optical clearing agents has focused on clearing of the skin [220], although a recent study of possible relevance to the present work examined optical clearing of articular cartilage using the low-osmolality CT contrast agent iohexol [221].

Table 4.1 summarizes some applications of OCAs in OCT imaging [225]–[227], where glycerol in various concentration is often the preferred choice. In the context of optical clearing in tissue, glycerol passively diffuses from loosely arranged outer layers (e.g., epithelial) into the intercellular space [223], [228], [229]. The diffusion rate of glycerol in the tissue is slower than the migration rate of water out of the tissue, as glycerol has a higher osmolarity and larger molecular size compared to water.

reference	[225]	[225]	[226]	[226]	[227]	[227]
imaging system characteristics	$\lambda_o = 1300\ nm$ $\Delta\lambda = 52\ nm$	$\lambda_o = 1300\ nm$ $\Delta = 52\ nm$	$\lambda_o = 1300\ nm$ $\Delta\lambda = 52\ nm$	$\lambda_o = 1300\ nm$ $\Delta\lambda = 52\ nm$	$\lambda_o = 820\ nm$ $\Delta\lambda = 25\ nm$	$\lambda_o = 820\ nm$ $\Delta\lambda = 25\ nm$
OCAs	50% dimethyl sulfoxide	50% glycerol	50% glycerol	80% glycerol	70% glycerol	80% propylene glycol
Tissue type	porcine stomach tissue	porcine stomach tissue	porcine skin tissue	porcine skin tissue	rat skin	rat skin
application method	topical application	topical application	topical application	topical application	topical application	topical application
time	Immediate	50 min	60 min	60 min	40 min	40 min
optical attenuation improvement	22 dB/mm	18 dB/mm	11 dB/mm	21 dB/mm	20 dB/mm	X
tissue shrinkage percentage	8% at T=50 min	8% at T=50min	not significant	X	X	X
Note	λ_o and $\Delta\lambda$ refers to the center wavelength and bandwidth of the OCT light sources, respectively. And X indicates no reporting or not quantifiable measurements were performed.					

Table 4.1: Overview of optical clearing agents (OCAs) utilization in OCT imaging

As glycerol penetrates the tissue, it draws intercellular fluids out and pulls interstitial water further away from cells and fibres, creating a refractive index-matching environment while increasing the tissue density. Consequently, water displacement from the tissue is expected in the initial stage of optical clearing, leading to tissue dehydration. The clearing performance is believed to increase in parallel with the dehydration effect. Once glycerol fully permeates the tissue during the later stages of clearing (i.e., after 20 minutes [229], [230]), it draws water back into the cells due to its high affinity for water since glycerol is hydrophilic and has excellent solubility in water. As a result, tissue rehydration may occur, and swelling could take place due to the rearrangement of collagen fibres [228].

For the present study we selected glycerol for optical clearing as glycerol is a widely used component of commercially marketed eardrops for softening and dispersing cerumen [231], is used at 1,000mg/mL concentration to treat acute otitis media [232], and is a component in nasal sprays [233]. The long and widespread use of glycerol in these applications gives some confidence in glycerol's general safety and capacity to be tolerated when used in the external ear canal. To our knowledge, while OCAs have previous been used for increasing the transparency of the TM to improve infrared otoscopy [6], OCAs have not previously been used to aid middle ear OCT imaging. We envision a scenario where an OCA would be administered topically to the post-tympanoplasty TM in clinic as an eardrop. Patients would wait for the clearing effect to occur, and OCT imaging would be conducted. Following imaging, the OCA would be rinsed off or resorbed to return the TM and graft to their original state.

In the present preclinical feasibility study, we focus on assessing the rate of clearing and the degree of clearing that can be achieved in tragal cartilage (which is used for autologous grafts in our institution) in vitro. We also focus on demonstrating the potential clinical utility of OCAs in combination with OCT imaging in a cadaveric model as a first step toward clinical studies. The experimental outcomes relevant to this assessment are the amount and rate of clearing achieved, the time needed to achieve full clearing and the improvement in OCT image quality that results from the clearing. As an initial assessment of safety of the approach, we also investigate the amount of tissue shrinkage caused by glycerol absorption [225] and the reversibility of the clearing process [220].

4.5   Methods

Tragal cartilage samples were obtained from excess material harvested from consenting patients during cartilage tympanoplasty surgery ($N = 5$). All human tissues were collected in accordance with a protocol approved by the Nova Scotia Health Authority Research Ethics Board (REB FILE# 1022981) and with the Helsinki Declaration (JAMA 2000; 284:3043 – 3049). Samples were cut into $5\ mm \times 5\ mm$ sections, refrigerated, and kept in 0.9% saline until used. Subcutaneous fat and pericondrium were removed from the samples to expose only the cartilage. To measure the reversibility of glycerol absorption, $N = 7$ pieces of excess cartilage obtained from trimming the samples were treated with undiluted glycerol for 90 minutes and washed in saline for 10 minutes. Samples were imaged under white-light microscopy before and after treatment. ImageJ [234] was used for estimating the surface area of the samples. Following preparation, the samples were cut to 400 μm thickness using a Kurz precise cartilage knife [235].

4.5.1   OCT imaging set-up

Measurements of cartilage opacity were made using a custom swept-source OCT system designed for in vivo imaging of the human middle ear operating at a center wavelength of 1550 nm with a sweep range of 40nm, a sweep rate of 100 kHz and a maximum output power of 9.3mW. The system achieved a lateral resolution of 50μm and an axial

resolution in air of $40\mu m$[a] and a sensitivity of 105dB and could image over a depth range of 15mm, allowing it to image the full depth of the middle ear in 2D (512×330 pixels) at 20 frames per second or 3D ($512 \times 512 \times 330$ voxels) at one volume per 5s. The system also has vibrometric measurements capabilities [1], but these were not used in this study. The system is a more advanced prototype of the system described in detail in a previous publication from our group [1] with the same system architecture and similar performance.
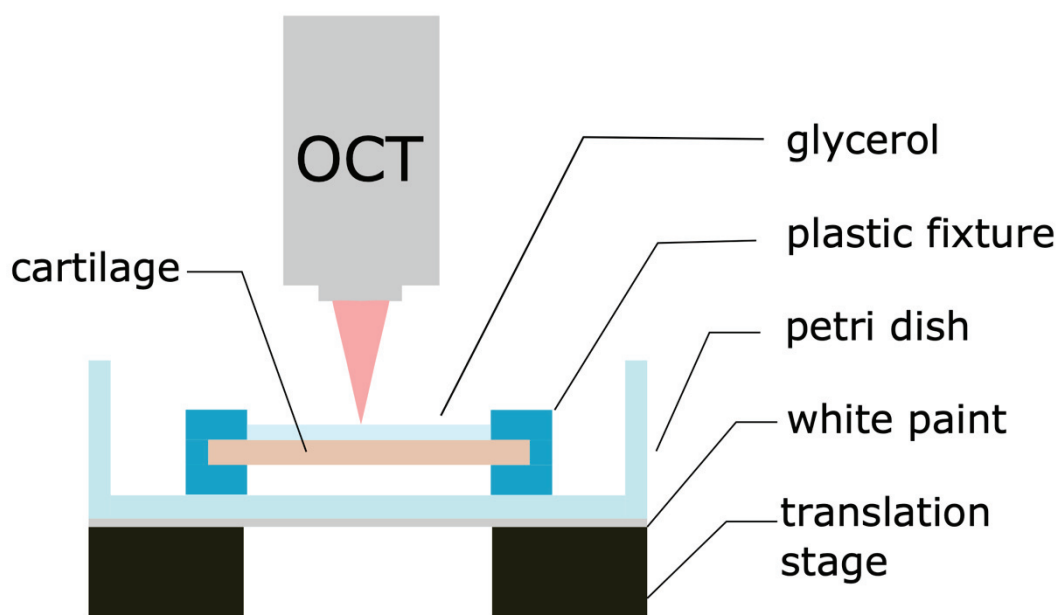
Figure 4.2: Experimental setup for measuring the reflectance of a reference reflector through cartilage samples.

A reference reflector consisting of a glass petri dish whose bottom was painted white was used as a reference target as shown in Figure 4.2. The reflector was imaged through the cartilage samples as they cleared. At each time point, the cartilage samples were treated topically with anhydrous glycerol and the glycerol was allowed to diffuse into the cartilage for 60 seconds. The glycerol was then wiped off the sample with a swab and an OCT B-mode scan of the sample and target was collected. This produced a set of

---

[a] At the time of this manuscript's publication, the documented lateral and axial resolutions stand at 50μm and 40μm in air, respectively. These resolutions are marginally inferior to those reported in previous chapters, primarily attributed to the use of a different laser equipped with an earlier version of firmware.

OCT images taken at the same location at intervals of one minute. The process was repeated until no further significant increase in transparency was observed.

4.5.2   Glycerol concentration

Previous studies have suggested that the concentration of OCAs influences the degree of clearing achievable for specific tissue types. This is due to the varying osmolarity of different concentrations [222], which affects the rate of water efflux and OCA influx. Tissues also differ in structure, thickness, and density, further complicating the clearing process [219], [236]. While higher OCA concentrations generally result in enhanced tissue transparency, they may require longer diffusion times for optimal clearing [236]. Additionally, high concentrations of standard OCAs (e.g. ethanol, CLARITY) can be toxic to living tissues or cells [219], limiting their use in in vivo imaging. Therefore, selecting the appropriate OCA as well as a suitable concentration is essential for maximising clearing efficacy while preserving tissue integrity and minimising potential toxicity for in-vivo application [227].

Glycerol is commonly regarded as a preferred optical clearing agent for in vivo applications [222], [223] due to its high refractive index [220], [223], high osmolarity [225], low toxicity [223], [237], [238], and reversible dissociation of collagen [223]. Concentrations typically range between 50% and 100% for both immersion and topical applications [220], [222], [227], [228], [230]. However, determining the optimal glycerol concentration for optical clearing remains a subject of ongoing debate as selecting the appropriate concentration involves considering factors such as tissue type, imaging modality, and desired transparency while considering potential tissue shrinkage [222] or swelling effects [228].
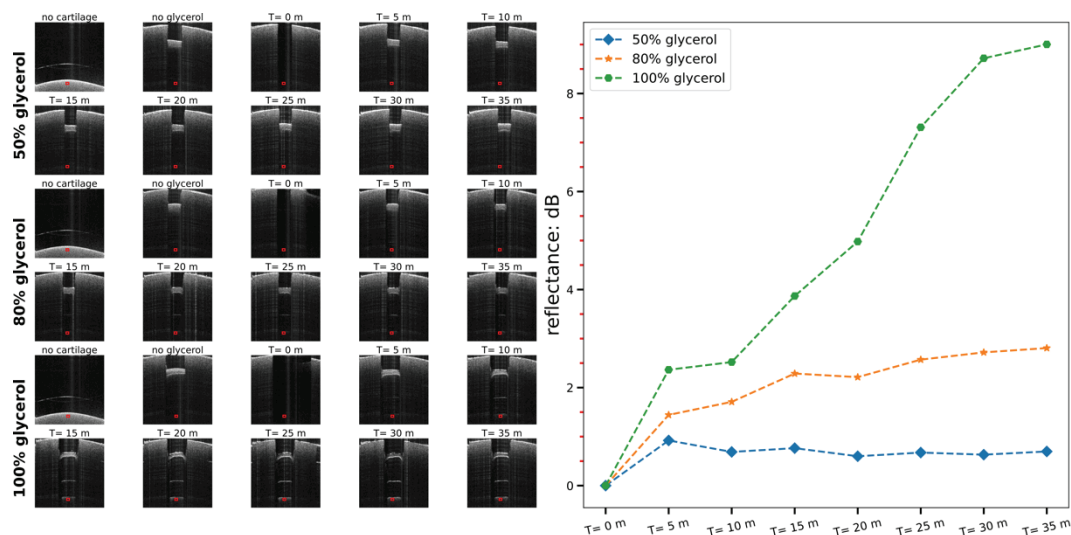
Figure 4.3: A series of OCT B-mode images of porcine ear cartilage with a white paint reference reflector distal to it taken at 5-minute intervals during optical clearing with 50%, 80% and 100 % of the glycerol concentration using the experimental setup shown in Figure 4.2. The red box highlights a region of interest (ROI) of 20×20 pixels in the reference reflector. The graph on the left depicts the reflectance of the reference reflector during the clearing process at 5-minute intervals, extending up to 35 minutes. At $T = 0$ min, the moment when glycerol was applied to the cartilage samples, the cartilage's apparent disappearance in the presented OCT B-mode images can be observed. This phenomenon can be attributed to glycerol's high absorption at 1550 nm [239], which effectively absorbs the incident light, diminishing the OCT signal reflected from the cartilage. The blue, orange, and green lines represent 50%, 80%, and 100% glycerol concentrations, respectively. The presented images of the flat reference reflector appear curved due to fan-beam distortion. By the time this thesis was prepared, the system software was capable of correcting for this distortion[135], but this correction was not available at this time this study was conducted.

In vitro pilot studies were conducted using a porcine concha cartilage model to identify the optimal glycerol concentrations for enhancing optical transparency. The experiment involved topically applying glycerol at concentrations of 50%, 80%, and 100%, as depicted in Figure 4.2, to a set of porcine pinna cartilage samples harvested from fresh-frozen porcine ears. Each cartilage sample was prepared by removing the perichondrium from both sides and thinning it to 0.4mm. Glycerol was applied topically for 35 minutes, with measurements taken at 5-minute intervals. We assessed the time-dependent two-way optical transmission using optical coherence tomography (OCT) imaging of a reflector positioned distal to the cartilage. The clearing performance was estimated by averaging the pixel intensity within the ROI in Figure 4.3, as denoted by the red box. The reflectance-over-time graph shown on the right side of Figure 4.3 illustrates that 100% glycerol outperforms both the 50% and 80% glycerol groups, achieving

maximum clearing level of 9.01 dB (22dB/mm) in reflectance at the 35-minute point. In addition, each group exhibits a varying degree of porcine pinna cartilage clearing, showing a consistent increase over time. Furthermore, the 80% glycerol group exhibits a marginally higher degree of optical clearing performance than the 50% glycerol group that the 80% glycerol group achieving 2.80 dB (7.0dB/mm) at 35 minutes and the 50% glycerol group only reaching 0.69 dB (1.7dB) in the same timeframe, $T = 35$ min. The clearing effect of the 100% glycerol group was threefold that of the 80% glycerol group and 13 times that of the 50% glycerol group, indicating that higher glycerol concentrations are more effective in improving tissue transparency. This observation is in line with findings from previous studies, further supporting the notion that increased glycerol concentrations lead to higher tissue clearing efficacy [222], [228], [230].

4.6   Results
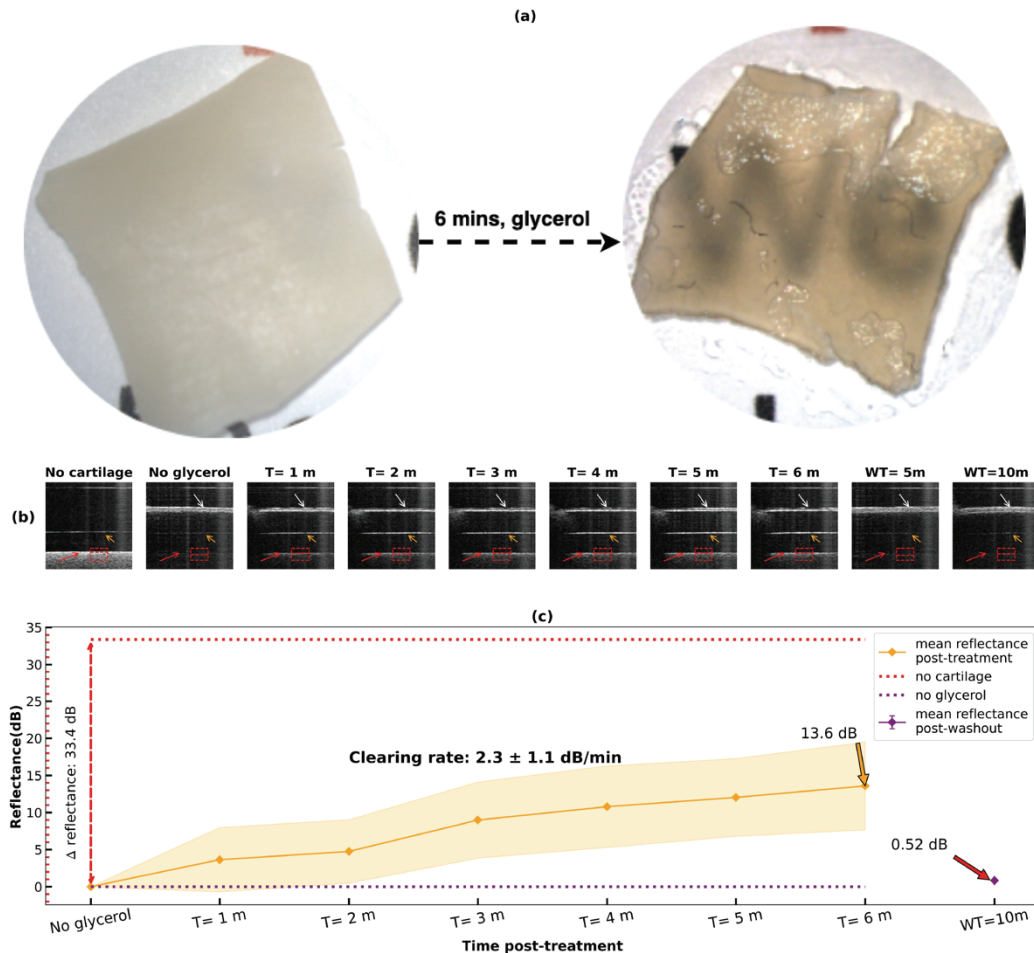
Figure 4.4: (a) Photograph of cartilage graft pre- and post-optical clearing with 100% glycerol. (b) A series of OCT B-mode images (zoomed in to highlight the optical clearing performance) of cartilage with a white paint reference reflector distal to it taken at 1-minute intervals during optical clearing and at 5-minute intervals following washout in saline. The white, orange, and red arrows indicate the proximal side of the graft, the distal side of the graft, and the reference reflector. The red box indicates an ROI of 50×50 pixels in the reference reflector and a dotted red line traces out the top surface of the petri dish (b) plot of reference reflector reflectance during clearing. The red dotted line indicates the reflectance observed in the absence of the graft, and the purple dotted line indicates the baseline reflectance before glycerol treatment. The solid purple line indicates the reflectance after washout. The mean reflectance is represented by the orange line, with the shaded yellow area illustrating the range within one standard deviation.

Figure 4.4 (a) shows a typical tragal cartilage graft harvest from a patient undergoing surgery lying on a printed paper sheet before and after an immersion in glycerol for 6 minutes. The increased transparency of the cartilage and the increased contrast of the text behind it is readily apparent in the photograph. Figure 4.4 (b) shows a

sequence of OCT B-mode images of the reference target taken at one-minute intervals in the clearing process for one of the samples. In each OCT B-mode image, the white arrow indicates the location of a harvested tragal cartilage graft where both the proximal and distal sides of the graft can be easily identified. The orange arrow points out the top glass surface of the petri dish and the red arrow shows the painted bottom surface of petri dish. The brightness of the target (indicated by the red arrow) progressively increases as the cartilage clears over time. Figure 4.4 (c) displays the degree of optical clearing with 100% glycerol within the region of interest (ROI), denoted by the red box in the B-mode images, captured at one-minute intervals. The mean reflectance is represented by the orange line, with the shaded yellow area illustrating the range within one standard deviation. The red dashed line indicates the baseline ROI mean intensity when the target is imaged directly with no cartilage between it and the OCT optics. The purple dashed line indicates the ROI mean intensity observed before glycerol is applied to the cartilage sample.

Following treatment with glycerol, the intensity of the ROI increased roughly linearly at $2.3(\pm 1.1)$ dB/min and reached saturation in less than 7 mins, with a mean reflectance increase of $13.6(\pm 5.9)$dB. Following clearing, the samples were bathed in saline for 10 minutes and the reflectance remeasured and found to be $0.52(\pm 0.50$dB) consistent with a return to baseline transparency with no significant difference in mean intensity before treatment and after washout ($p > 0.5$). This demonstrates that the optical clearing caused by glycerol can be reversed.
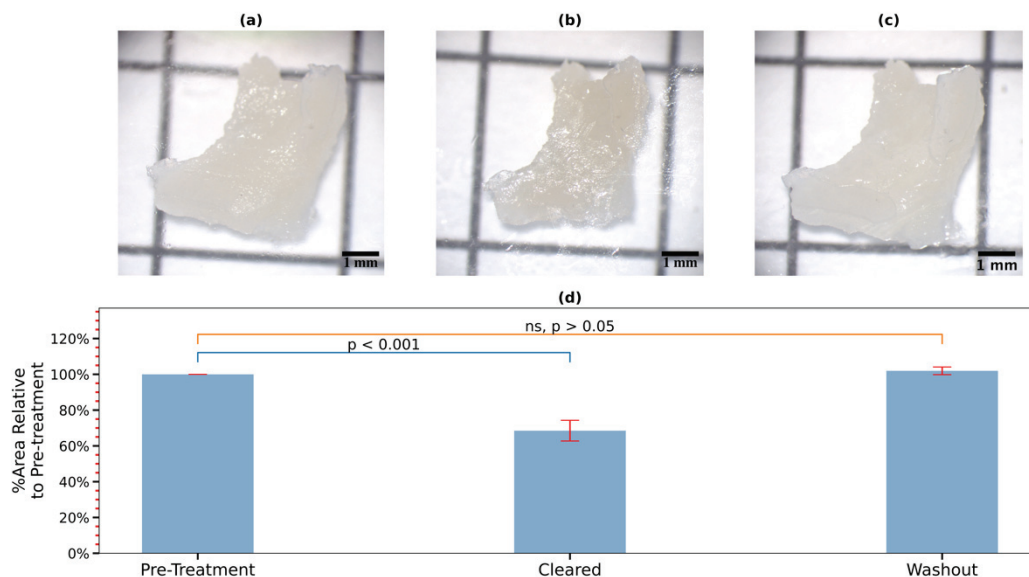
Figure 4.5: Photograph of cartilage graft overlaying a 5×5 mm grid reference sheet. (a) Cartilage graft before treatment with glycerol (b) after treatment with glycerol with reduced area (c) after saline washout for 10 minutes (d) surface area changes for (a), (b), and (c) for $n = 7$ samples. NS denotes nonsignificant for a two-tailed t test.

Figure 4.5 shows the results of investigation into glycerol-induced shrinkage of the cartilage samples. $N = 7$ small cartilage samples trimmed from the cartilage harvested from patients were immersed in undiluted glycerol for 90 mins to achieve full glycerol absorption. A mean reduction in sample area of $31(\pm 6)$ % was observed under optical microscopy, presumably due to hyperosmotic dehydration. Following immersion in a saline bath for 10 minutes, the samples returned to $102(\pm 2)$ % of the original area indicating that the dimensional changes associated with optical clearing are also reversible.

4.6.1 OCA application in ossiculoplasty
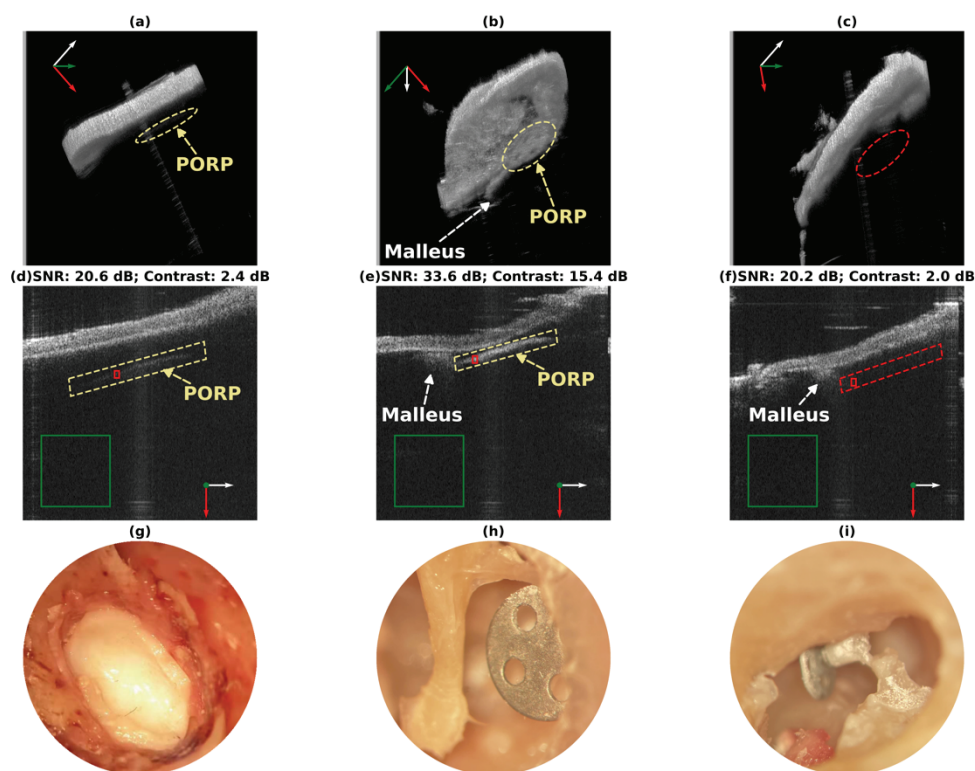
Figure 4.6: Imaging of a simulated ossiculoplasty model. (a), (d), and (g): 3D OCT image, B-mode image and microscopic image of the untreated cartilage graft overlaying the PORP; (b), (e), and (h): 3D OCT image and B-mode image of middle ear through cleared cartilage and transcanal microscopic photo with cartilage graft removed to show orientation of PORP; (c), (f), and (i): 3D OCT image and B-mode image through cleared cartilage graft of the middle ear after PORP was deliberately dislodged and otoscopic photo of the middle ear taken through a posterior tympanotomy showing the dislodged PORP. The PORP was not visible in transcanal microscopy after it was dislodged. The 3D images have been oriented so as to highlight the location of the PORP with a different orientation used in each image. A set of cartesian axes are provided to show the orientation. The red arrow points laterally in the direction of the ear canal, the white arrow points superiorly and the green arrow points anteriorly. The yellow ellipse/box in (a), (b)/(d), (e) highlight the location of the PORP whereas the red ellipse/box in (c)/(f) indicates the original position of the PORP before its simulated dislodging in 2D and 3D images. PORP indicates partial ossicular replacement prosthesis.

Figure 4.6 shows the result of a preclinical validation of the use of optical clearing for post-operative visualisation of the middle ear in a cadaveric temporal bone model. A cadaveric temporal bone was prepared by removing the pinna and cartilaginous ear canal to improve access. The incudostapedial joint (ISJ) was disarticulated and the tympanic membrane and incus were removed through the canal. A partial ossicular replacement prosthesis (PORP) was placed on the stapes superstructure and covered with a tragal

cartilage graft harvested from the same cadaveric temporal bone, prepared in the same way as in the in vitro experiment and cut to fit the dimensions of the tympanic annulus. 3D OCT images, 2D OCT images and microscopic photos of the middle ear were obtained through the untreated cartilage. In the 2D OCT image, two ROIs were selected in the PORP (solid red boxes), and in the empty background region (solid green box).

SNR and contrast between the PORP and background were used to assess the improvement of visibility in the simulated ossiculoplasty model. It is important to highlight, as demonstrated by (2.1) and (2.4), that OCT quantifies the intensity of light, which is proportional to the square of the electric field. SNR is defined as [85], [240]:

$$SNR = 10 \log_{10} \frac{\mu_s}{\sigma_b} \qquad (4.1)$$

Where μ_s is the mean intensity in the PORP (signal) ROI and σ_b is the standard deviation of the intensity in the background ROI. Contrast is defined as [85], [240]:

$$C = 10 \log_{10} \frac{\mu_s}{\mu_b} \qquad (4.2)$$

Where μ_b is the mean intensity in the background region. Both SNR and contrast are expressed in decibels. However, in instances where the objective is to measure field quantities, an alternative definition of SNR and contract may be more suitable [85], [240], [241].

After obtaining baseline images with uncleared cartilage (Figure 4.6 (a), (d), (g)), the cartilage was removed and placed in a glycerol bath for 10 minutes to achieve full optical clearing, wiped clean of glycerol with a swab and placed onto the annulus. Figure 4.6 (h) shows the PORP and handle of the malleus with the cartilage removed. In the OCT images of Figure 4.6 (a) and (d), prior to glycerol treatment, the PORP (indicated with a yellow arrow) is barely visible in the 2D and 3D OCT images. Following treatment, the PORP with its distinctive circular plate with holes is readily visible. The improvement in SNR between Figure 4.6 (d) pre-treatment and (e) pos-treatment was 13 dB. In particular, the contrast of PORP saw a significant improvement, from practically imperceptible 2.4 dB to a readily discernable 15.4 dB. To demonstrate that clinically significant changes could be observed with this technique, the shaft of PORP was detached from the stapes footplate to simulate the postoperative dislocation of the PORP

as seen in Figure 4.6 (i). The middle ear was again re-imaged through the cleared cartilage graft using OCT from the ear canal. In both 2D and 3D OCT images, the PORP is no longer visible at its original location (indicated by the dashed red ellipse for 2D and box in 3D images).

4.7 Discussion

While optical clearing of skin has been extensively studied, to our knowledge there has only been one previous study examining optical clearing of cartilage. In this study, a 0.90 mm thick sample of bovine articular cartilage was cleared with iohexol and the OCT loss slope was found to decrease by 30dB/mm within 50 minutes after treatment [221], this degree of clearing is consistent with the clearing observed in this study of 34 dB/mm following 7 minutes of clearing in a 0.40 mm sample. Other studies also confirmed the similar improvement in contrast with various combination of tissues and OCAs [225], [227].

In a laser Doppler vibrometry study examining the effect of varying cartilage tympanoplasty thickness on acoustic vibration, it was found that thinner tympanoplasties exhibit improved low-frequency sound transmission performance down to $400\mu m$ thickness [242]. In practice, the improved acoustic performance from thinner grafts must be weighed against the increased difficulty in handling them during surgery due to the tendency of thin grafts to curl, but $400\mu m$ grafts are generally manageable. The present study offers a second reason to use thinner grafts, namely, to enable improved post-surgical follow-up through OCT-based visualisation of the middle ear.

The degree to which cartilage is thinned and whether perichondrium is preserved on one, both or neither surface of the graft is a matter of personal choice and varies between surgeons. Some surgeons augment the lateral surface of their cartilage reconstruction with fascia to facilitate the re-epithelialization of the lateral surface of the graft from the tympanic membrane remnant or deep canal skin. The medial aspect of the cartilage graft usually becomes mucosalised with time.

The present study does not account for the interposition of these additional layers in the reconstruction. As the epithelial covering lateral to an established cartilage repair and the medial mucosal layer are much thinner than the graft itself, it seems likely that

they would have little direct optical effect. However, the lateral epithelium may prevent the diffusion of the OCA into the cartilage from the ear canal thereby slowing the optical clearing effects. In a clinical scenario, we imagine an optical clearing agent being applied to the tympanic membrane of a patient followed by a 20-to-30-minute wait for the clearing to take effect. Whether this is feasible can only be established in an in vivo model in which the graft is epithelialized.

Three important issues relevant to the safety of using OCAs are graft shrinkage, ototoxicity, and reversibility. In our experiments we observed $31(\pm 6)$ % areal tissue shrinkage corresponding to a 14% change in linear dimensions. While it is reassuring to see that the cartilage shrinkage seen after treatment with the OCA is reversible, shrinkage can be expected to create stress on the surrounding tympanic membrane tissue that may have safety implications. Given the natural compliance of cartilage and the elasticity of any residual rim of native tympanic membrane, we do not anticipate that the observed degree of shrinkage would cause any permanent damage to the tympanic membrane repair. However, careful in vivo studies on well-established, robust, in situ, cartilage tympanoplasty grafts are required in animals or humans to verify this point.

Should shrinkage prove to present risk to patients, OCAs with lower osmolality than glycerol are available that may exhibit lower shrinkage, although the ototoxicity of any candidate OCAs would have be closely evaluated [226]. Glycerol can also be diluted with water in order to decreases its ability to dehydrate and shrink tissue, but dilution also decreases its effectiveness as an optical clearing agent [226].

While we are not aware of any formal studies of the ototoxicity of glycerol, its widespread use in eardrops [231] and nasal sprays argue that it is it is safe to use in the outer and middle ear. Glycerol is produced endogenously by sebaceous glands and is a naturally occurring component in blood plasma where it plays a role in maintaining epithelial hydration levels [243]. As a result, the body is capable of transporting and metabolising glycerol, although the local uptake rate and mechanisms for glycerol in the tympanic membrane specifically has not previously been investigated. On this basis it appears likely that glycerol used in optical clearing of cartilage grafts would be resorbed naturally by the body, although it is not clear how long this process would take. In our study, the effects of glycerol clearing on the optical and mechanical properties of

cartilage grafts appear to be fully reversible following rinsing with saline which provides reason to expect that glycerol absorption would be reversible in vivo.

While this study has focused on the visualisation of the middle ear through autologous cartilage tympanoplasties, many other graft materials are available and have been used in this application. Autologous graft materials used for tympanoplasty grafts include fascia, perichondrium, periosteum, vein, fat, and skin [61] with cartilage and fascia being the most common in modern practice. Additionally, new graft biomaterials for tympanic membrane grafts remains an active area of research, with grafts having been demonstrated made from polylactic acid [215], polydimethylsiloxane [215], polycaprolactone [215], and decellularized porcine tissue [244] among other materials [245]. The optical clearing techniques we demonstrated in this study for cartilage may be applied to these other materials as well, and some of these materials may have sufficient innate transparency as to permit acceptable middle ear imaging without the need for optical clearing. As middle ear OCT gains adoption, optical transparency (whether innate or induced with OCAs) may become an increasingly important consideration in the selection of graft materials alongside traditional considerations of acoustic performance, biocompatibility, and mechanical strength.

Finally, while the present study focused on the ability of optical clearing agents to improve visualisation with OCT, our results apply equally well to other optical imaging modalities including traditional optical modalities like optical microscopy/otoscopy and more advanced methods like Raman spectroscopy. And while this study focused on the clearing of tympanoplasties, the same techniques could potentially be used to clear thickened, scarred, calcified or fibrotic TMs which can also make visualisation of the middle ear space difficult.

4.8   Conclusion

We have measured the optical attenuation of a cartilage tympanoplasty model using optical coherence tomography before and after application of glycerol as an optical clearing agent. We observed a mean reduction in attenuation in cartilage grafts of $13.6(\pm 5.9)$ dB at an estimated linear rate of clearing of $2.3(\pm 1.1)$ dB/min following topical application of glycerol. We also showed that this degree of clearing was clinically

significant for imaging of post-ossiculoplasty ears and that it generated SNR and contrast improvements of 13dB and 13dB in imaging a prosthesis. The process of glycerol absorption appears reversible, at least in terms of the optical clearing and the dimensional changes that it generates. The amount of clearing achieved, and the rate of clearing appear consistent with the clinical application of this technique to facilitate visualisation in post-operative ears and provide strong motivation for the extension of this work to in vivo studies in patients.

Chapter 5

Conclusions and future direction

This final chapter summarizes the research conducted, synthesizing the key findings and highlighting their significance within the broader context of the study area. Furthermore, we outline promising directions for future investigations that may expand the utilities of ME-OCT in clinical otology.

5.1   Conclusion

New medical imaging technologies have the potential to improve the diagnosis and clinical management of diseases [143], while also contributing to a better understanding of their pathogenesis and the development of novel therapies [82]. One such technology is ME-OCT, which aims to extract diagnostically relevant information from acquired images and present easily interpretable images to clinicians [82], [94]. However, the clinical translation of ME-OCT can be impeded by suboptimal image quality, resulting in image artefacts and limitations that restrict imaging depth due to optical loss as well as to imperfections in the light source and optics that can result in undesired sidelobes in the axial point spread function (PSF). These limitations can ultimately limit the diagnostic utility of ME-OCT and even lead to misinterpretation of images or incorrect diagnoses when spurious structural information is present. As ME-OCT gains popularity in clinical otology, there is an increasing need to improve image quality to facilitate more accurate diagnoses which motivated the development of this thesis.

Chapter 3 of this work presents an innovative approach by applying convolutional basis pursuit denoising with dictionary learning to complex OCT A-line data. This method produces OCT images in which anatomical structures are retained with high fidelity, while axial sidelobe artefacts and stochastic noise are highly suppressed. The application of this processing technique offers additional advantages such as enhanced image contrast at tissue boundaries and an increase in the SNR, attributable to the

substantial reduction of both sidelobe artifacts and background noise. Dictionary learning is particularly well-suited to OCT systems in which the PSF drifts with time because it can provide continuously updated estimates of the PSF from imaging data without requiring any additional calibration steps. Convolutional basis pursuit denoising is substantially less computationally demanding than conventional basis pursuit methods that have previously been applied to OCT image analysis. While real-time processing was not demonstrated in this study, our processing rate of 1.28s/frame on consumer grade hardware, without using GPU-based acceleration makes it seem feasible that, with further optimisations and integration, CSC could be performed at video rates.

Admittedly, learning the PSF is a slower step in comparison, but it only needs to be done periodically, on the order of once per frame or less and so it may also be compatible with real-time processing rates. Even at non-real-time rates, the proposed technique is still a useful post-processing step that can be applied to images intended for storage or post-rendering, such as in volumetric data acquisition. For instance, this method has significantly enhanced the interpretation of ME-OCT images collected in our studies [130], [131], [135], demonstrating its utility and practical benefit within our research group.

The results of Chapter 3 demonstrate that sparsity-based deconvolution can effectively suppress sidelobe artefacts and enhance the image quality of ME-OCT. In particular, the described technique ensures good preservation of anatomical structures, a key aspect for the appreciation and exploration of the middle ear space in ME visualisations with OCT. Furthermore, although, this method was initially conceived to enhance the image quality of ME-OCT, it has also demonstrated promising outcomes in diverse applications. Notably, it has been successful in improving the quality of OCT images of index fingers and onion slices, signifying a possible broader utility beyond the field of otology.

One significant hurdle in ME-OCT visualisation stems from signal attenuation caused by the scattering of light. As light traverses through the TM, multiple scattering of light occurs. In instances where the overall thickness of the TM alters due to pathologies or the use of grafts, the thickened TM can preclude the visualisation of the middle ear space with OCT. Chapter 4 delves into the application of optical clearing agents (OCAs),

which improves the effective penetration depth of light when imaging through highly scattering tissue (i.e., TM), as a potential method to enhance the imaging quality of ME-OCT. More specifically, the study conducted an ex-vivo experiment using both animal and cadaveric models and focused on a common clinical scenario: TM thickness increase as a result of cartilage tympanoplasties. In middle ear surgery for CHL, patients could receive a TM graft made from a sheet of autologous cartilage taken from the patient's tragus. Given that this graft is optically opaque, the presence of the graft hampers OCT's ability to visualise post-operative middle ear structures.

Chapter 4 highlights the potential of anhydrous glycerol, a hyperosmotic and non-toxic compound, in its role as an effective optical clearing agent (OCA) to reduce the optical scattering coefficient of cartilage over less than 10 minutes. The level of clearing demonstrated in that study significantly improved the ability to visualise the middle ear with OCT. These results are promising for the eventual clinical use of optical clearing agents to allow OCT-based visualisation of the post-surgical middle ear. Moreover, the reversible nature of this technique, in combination with a consistent level of observed tissue shrinkage, argues for the method's safety for patient use.

5.2   Future direction

Chapter 3 and Chapter 4 detail two distinct methods aimed at enhancing the image quality of ME-OCT. The first approach is computational, employing signal processing techniques, while the second involves physically altering the imaging tissue's properties using a biocompatible and osmotically active chemical. These techniques enable improved visualisation of middle ear pathologies using ME-OCT, leading to a more precise interpretation of ME-OCT images.

One potential avenue for further exploration involves the in-vivo application of glycerol as an optical clearing agent (OCA) for visualising the middle ear. An unanswered question is whether the same degree of clearing, sufficient for clinical utility in OCT visualisation and measurement within the middle ear, can be achieved in vivo.

More specifically, the study presented in Chapter 4 did not assess the ability of glycerol to increase the transparency of cartilage grafts that have fully healed and undergone epithelialization. It also did not investigate the efficacy of glycerol in clearing

fibrotic, tympanosclerotic, or otherwise thickened TM for which appropriate cadaveric models do not exist. One intermediate strategy involves applying optical clearing agents (OCAs) to healthy, normal tissues. This will allow us to establish a baseline against which we can compare and assess the effectiveness as well as possible address possible adverse effects of the OCAs that was not present in the ex-vivo studies.

5.2.1 In vivo application of OCAs in healthy normal

Prior in-vitro studies on cartilage grafts have demonstrated that the topical application of glycerol can increase optical transparency by 13 dB, enabling structural imaging of middle ear structures through the graft. However, it remains uncertain whether the same degree of clearing can be achieved in vivo with thickened eardrums due to tympanoplasties or CHL pathologies.
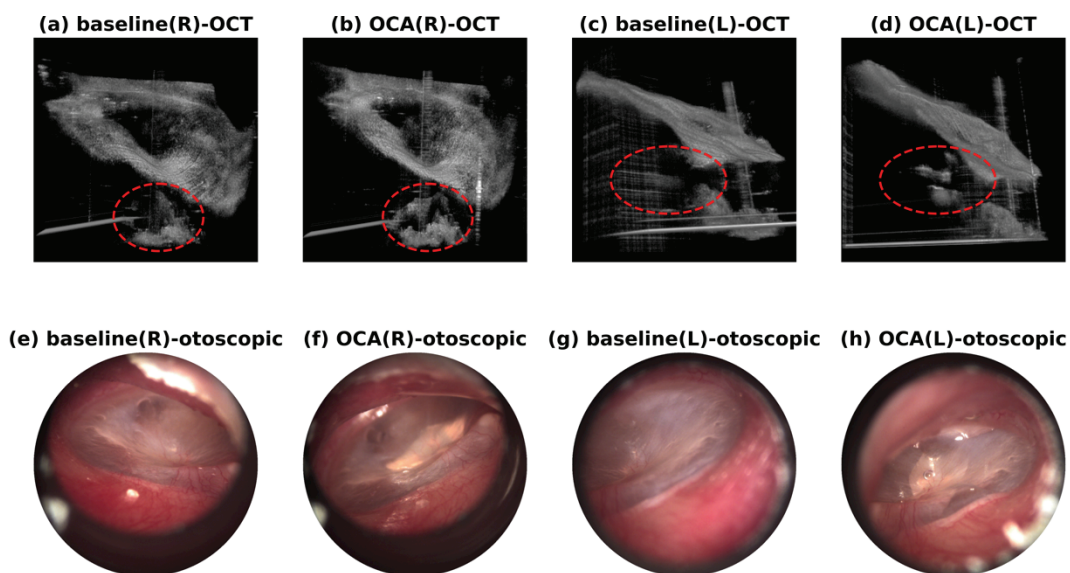
Figure 5.1: In vivo application of OCAs was performed on the author with the over-the-counter eardrops for ear cerumen removal that contain anhydrous glycerol [246]. The top rows are the 3D-OCT still images of the baseline (i.e., without glycerol) and the OCA application of both right (denoted as R) and left (L) ears. The bottom rows are the otoscopic images (Macroview ® basic otoscope, Welch Allyn).

To develop a clinical protocol for applying the OCA on patients with tympanoplasties or calcified or fibrosed eardrums, we administered an eardrop containing anhydrous glycerol, a commercially available solution for ear cerumen removal [246], to a healthy individual. The contact of the eardrop with the eardrum was confirmed through otoscopic examination, and the TM was evaluated for any signs of inflammation,

damage, or permanent changes. After leaving the clearing agent on the ear for 10 minutes, it was removed using a cotton swab, and the eardrum was subsequently re-examined with OCT where still 3D images were captured. The images obtained were compared to a control image taken in the same ear prior to the eardrop administration in the same display range. Throughout the process, the volunteer reported no discomfort and did not experience any sensations of irritation which was previously suggested in literature [227].

Although only a qualitative assessment was performed, Figure 5.1 (b) demonstrates that the increased optical transparency allows for an improvement in image SNR. The increase transparency manifests as a higher brightness of a visible portion of the cochlear promontory (CP) when compared to the baseline in Figure 5.1 (a) for the right ear. For the left ear, the partial incus in the before image becomes brighter following treatment as does the cochlear promontory. Furthermore, when comparing Figure 5.1 (h) and (i), the TM becomes less bright following treatment, an indication that it is generating less optical scattering. The TM also appeared more transparent under otoscopy post-treatment as compared to pre-treatment. These results provide some preliminary findings that glycerol can increase TM transparency in vivo without generating adverse events, an important step in investigating this approach in patients.

In summary, this thesis presents a cohesive body of work highlighting the author's contributions to enhancing the imaging quality of middle ear OCT. While still an emerging clinical technology, OCT could potentially be used as a non-invasive, ionizing radiation-free imaging technique to diagnose ME disorders. The improvement of middle ear OCT image quality holds clinical significance, as diagnosing conditions based on morphological changes in structures can benefit from artefact-suppressed images with an extended effective imaging depth. When combined with future research and validation, the work presented here could pave the way for the eventual clinical adoption of OCT as a standard diagnostic tool for otology.

Reference

[1]   D. MacDougall, L. Morrison, C. Morrison, D. P. Morris, M. Bance, and R. B. A. Adamson, "Optical Coherence Tomography Doppler Vibrometry Measurement of Stapes Vibration in Patients With Stapes Fixation and Normal Controls," *Otol. Neurotol.*, vol. 40, no. 4, pp. e349–e355, Apr. 2019, doi: 10.1097/MAO.0000000000002193.

[2]   H. E. I. Tan *et al.*, "Optical Coherence Tomography of the Tympanic Membrane and Middle Ear: A Review," *Otolaryngol. Neck Surg.*, vol. 159, no. 3, pp. 424–438, Sep. 2018, doi: 10.1177/0194599818775711.

[3]   C. Pitris, K. T. Saunders, J. G. Fujimoto, and M. E. Brezinski, "High-resolution imaging of the middle ear with optical coherence tomography: a feasibility study," *Arch. Otolaryngol. Head Neck Surg.*, vol. 127, no. 6, pp. 637–642, 2001, doi: 10.1001/ARCHOTOL.127.6.637.

[4]   D. MacDougall, J. Rainsbury, J. Brown, M. Bance, and R. Adamson, "Optical coherence tomography system requirements for clinical diagnostic middle ear imaging," *J. Biomed. Opt.*, vol. 20, no. 5, p. 056008, May 2015, doi: 10.1117/1.JBO.20.5.056008.

[5]   A. Burkhardt, L. Kirsten, M. Bornitz, T. Zahnert, and E. Koch, "Investigation of the human tympanic membrane oscillation *ex vivo* by Doppler optical coherence tomography: Investigation of the human tympanic membrane oscillation," *J. Biophotonics*, vol. 7, no. 6, pp. 434–441, Jun. 2014, doi: 10.1002/jbio.201200186.

[6]   S.-J. Oh, I.-W. Lee, S.-G. Wang, S.-K. Kong, H.-K. Kim, and E.-K. Goh, "Extratympanic Observation of Middle and Inner Ear Structures in Rodents Using Optical Coherence Tomography," *Clin. Exp. Otorhinolaryngol.*, vol. 13, no. 2, pp. 106–112, May 2020, doi: 10.21053/ceo.2019.00766.

[7]   B. E. Applegate, R. L. Shelton, S. S. Gao, and J. S. Oghalai, "Imaging high-frequency periodic motion in the mouse ear with coherently interleaved optical coherence tomography," *Opt. Lett.*, vol. 36, no. 23, p. 4716, Dec. 2011, doi: 10.1364/OL.36.004716.

[8]   T. J. Matthews and R. Adamson, "Optical coherence tomography: current and future clinical applications in otology," *Curr. Opin. Otolaryngol. Head Neck Surg.*, vol. 28, no. 5, pp. 296–301, Oct. 2020, doi: 10.1097/MOO.0000000000000654.

[9]   K. Park *et al.*, "Optical assessment of the in vivo tympanic membrane status using a handheld optical coherence tomography-based otoscope," *Acta Otolaryngol. (Stockh.)*, vol. 138, no. 4, pp. 367–374, Apr. 2018, doi: 10.1080/00016489.2017.1395515.

[10]   S. Mansour Jacques Magnan Hassan Haidar Ahmad Karen Nicolas Stéphane Louryan, "Comprehensive and Clinical Anatomy of the Middle Ear."

[11]   B. M. Carlson, "Special Senses—Vision and Hearing," in *The Human Body*, Elsevier, 2019, pp. 177–207. doi: 10.1016/B978-0-12-804254-0.00007-7.

[12]   S. E. Voss, N. J. Horton, K. E. Fairbank, L. Xia, L. R. K. Tinglin, and K. D. Girardin, "Measurements of ear-canal cross-sectional areas from live human ears with implications for wideband acoustic immittance measurements," *J. Acoust. Soc. Am.*, vol. 148, no. 5, p. 3042, Nov. 2020, doi: 10.1121/10.0002358.

[13]   O. Beger *et al.*, "Comparison of fetal and adult tympanic membrane sizes: a cadaveric study," *Surg. Radiol. Anat.*, vol. 43, no. 2, pp. 161–167, Feb. 2021, doi: 10.1007/s00276-020-02593-6.

[14]   S. Steuer *et al.*, "In vivo microstructural investigation of the human tympanic membrane by endoscopic polarization-sensitive optical coherence tomography," *J. Biomed. Opt.*, vol. 28, no. 12, Mar. 2023, doi: 10.1117/1.JBO.28.12.121203.

[15]   S. Van der Jeught, J. J. J. Dirckx, J. R. M. Aerts, A. Bradu, A. G. Podoleanu, and J. A. N. Buytaert, "Full-Field Thickness Distribution of Human Tympanic Membrane Obtained with Optical Coherence Tomography," *J. Assoc. Res. Otolaryngol.*, vol. 14, no. 4, pp. 483–494, Aug. 2013, doi: 10.1007/s10162-013-0394-z.

[16]   N. H. Cho, J. H. Jang, W. Jung, and J. Kim, "In vivo imaging of middle-ear and inner-ear microstructures of a mouse guided by SD-OCT combined with a surgical microscope.," *Opt. Express*, vol. 22, no. 8, pp. 8985–95, Apr. 2014, doi: 10.1364/OE.22.008985.

[17]   W. Kim, S. Kim, S. Huang, J. S. Oghalai, and B. E. Applegate, "Picometer scale vibrometry in the human middle ear using a surgical microscope based optical coherence tomography and vibrometry system," *Biomed. Opt. Express*, vol. 10, no. 9, p. 4395, Sep. 2019, doi: 10.1364/BOE.10.004395.

[18]   J. Won *et al.*, "Handheld Briefcase Optical Coherence Tomography with Real-Time Machine Learning Classifier for Middle Ear Infections," *Biosensors*, vol. 11, no. 5, May 2021, doi: 10.3390/BIOS11050143.

[19]   H. M. Subhash, A. Nguyen-Huynh, R. K. Wang, S. L. Jacques, N. Choudhury, and A. L. Nuttall, "Feasibility of spectral-domain phase-sensitive optical coherence tomography for middle ear vibrometry," *J. Biomed. Opt.*, vol. 17, no. 6, p. 060505, 2012, doi: 10.1117/1.JBO.17.6.060505.

[20]   E. M. Picou *et al.*, "Hearing, Emotion, Amplification, Research, and Training Workshop: Current Understanding of Hearing Loss and Emotion Perception and Priorities for Future Research," *Trends Hear.*, vol. 22, Jan. 2018, doi: 10.1177/2331216518803215.

[21]   U. Lemke and S. Scherpiet, "Oral communication in individuals with hearing impairment—considerations regarding attentional, cognitive and social resources," *Front. Psychol.*, vol. 6, p. 1, Jul. 2015, doi: 10.3389/FPSYG.2015.00998.

[22]   B. Yueh, N. Shapiro, C. H. MacLean, and P. G. Shekelle, "Screening and management of adult hearing loss in primary care: Scientific review," *JAMA*, vol. 289, no. 15, pp. 1976–1985, Apr. 2003, doi: 10.1001/JAMA.289.15.1976.

[23] "Quick statistics about hearing | NIDCD." https://www.nidcd.nih.gov/health/statistics/quick-statistics-hearing (accessed Mar. 21, 2023).

[24] A. S. Niskar, S. M. Kieszak, A. E. Holmes, E. Esteban, C. Rubin, and D. J. Brody, "Estimated prevalence of noise-induced hearing threshold shifts among children 6 to 19 years of age: the third national health and nutrition examination survey, 1988-1994, United States," *Pediatrics*, vol. 108, no. 1, pp. 40–43, 2001, doi: 10.1542/PEDS.108.1.40.

[25] T. C. Michels, M. T. Duffy, and D. J. Rogers, "Hearing Loss in Adults: Differential Diagnosis and Treatment," *Am. Fam. Physician*, vol. 100, no. 2, pp. 98–108, Jul. 2019, doi: 10.26616/NIOSHPUB2018124.

[26] H. J. Hoffman, R. A. Dobie, K. G. Losonczy, C. L. Themann, and G. A. Flamme, "Declining Prevalence of Hearing Loss in US Adults Aged 20 to 69 Years," *JAMA Otolaryngol. Neck Surg.*, vol. 143, no. 3, pp. 274–285, Mar. 2017, doi: 10.1001/JAMAOTO.2016.3527.

[27] F. R. Lin, J. K. Niparko, and L. Ferrucci, "Hearing Loss Prevalence in the United States," *Arch. Intern. Med.*, vol. 171, no. 20, pp. 1851–1853, Nov. 2011, doi: 10.1001/ARCHINTERNMED.2011.506.

[28] K. Feder, D. Michaud, P. Ramage-Morin, J. McNamee, and Y. Beauregard, "Prevalence of hearing loss among Canadians aged 20 to 79: Audiometric results from the 2012/2013 Canadian Health Measures Survey.," *Health Rep.*, vol. 26, no. 7, pp. 18–25, Jul. 2015.

[29] C. L. Nieman and E. S. Oh, "Hearing loss," *Ann. Intern. Med.*, vol. 173, no. 11, pp. ITC81–ITC96, Dec. 2020, doi: 10.7326/AITC202012010.

[30] K. E. Bainbridge and M. I. Wallhagen, "Hearing loss in an aging American population: extent, impact, and management," *Annu. Rev. Public Health*, vol. 35, pp. 139–152, 2014, doi: 10.1146/ANNUREV-PUBLHEALTH-032013-182510.

[31] J. M. Lasak, P. Allen, T. McVay, and D. Lewis, "Hearing loss: Diagnosis and management," *Prim. Care - Clin. Off. Pract.*, vol. 41, no. 1, pp. 19–31, Mar. 2014, doi: 10.1016/j.pop.2013.10.003.

[32] World Health Organization, "World report on hearing," 2021. Accessed: Mar. 21, 2023. [Online]. Available: https://www.who.int/publications/i/item/9789240020481

[33] F. H. Bess, J. Dodd-Murphy, and R. A. Parker, "Children with minimal sensorineural hearing loss: prevalence, educational performance, and functional status," *Ear Hear.*, vol. 19, no. 5, pp. 339–354, Oct. 1998, doi: 10.1097/00003446-199810000-00001.

[34] D. McDaid, A. L. Park, and S. Chadha, "Estimating the global costs of hearing loss," *Int. J. Audiol.*, vol. 60, no. 3, pp. 162–170, 2021, doi: 10.1080/14992027.2021.1883197.

[35] N. R. C. (US) C. on D. D. for I. with H. Impairments, R. A. Dobie, and S. V. Hemel, *Hearing Loss*. Washington, D.C.: National Academies Press, 2004. doi: 10.17226/11099.

[36] S. Chadha, K. Kamenov, and A. Cieza, "The world report on hearing, 2021," *Bull. World Health Organ.*, vol. 99, no. 4, p. 242, Apr. 2021, doi: 10.2471/BLT.21.285643.

[37] A. Orji, K. Kamenov, M. Dirac, A. Davis, S. Chadha, and T. Vos, "Global and regional needs, unmet needs and access to hearing aids," *Int. J. Audiol.*, vol. 59, no. 3, pp. 166–172, Mar. 2020, doi: 10.1080/14992027.2020.1721577.

[38] A. McCormack and H. Fortnum, "Why do people fitted with hearing aids not wear them?," *Int. J. Audiol.*, vol. 52, no. 5, pp. 360–368, May 2013, doi: 10.3109/14992027.2013.769066.

[39] B. O. Olusanya, "Screening for neonatal deafness in resource-poor countries: challenges and solutions," *Res. Rep. Neonatol.*, vol. 5, pp. 51–64, May 2015, doi: 10.2147/RRN.S61862.

[40] A. A. Adeyemo, "Knowledge of caregivers on the risk factors of otitis media," *Indian J. Otol.*, vol. 18, no. 4, p. 184, Oct. 2012, doi: 10.4103/0971-7749.104795.

[41] C. M. McMahon *et al.*, "The need for improved detection and management of adult-onset hearing loss in Australia," *Int. J. Otolaryngol.*, vol. 2013, pp. 1–7, 2013, doi: 10.1155/2013/308509.

[42] K. Kamenov, R. Martinez, T. Kunjumen, and S. Chadha, "Ear and hearing care workforce: current status and its implications," *Ear Hear.*, vol. 42, no. 2, pp. 249–257, Mar. 2021, doi: 10.1097/AUD.0000000000001007.

[43] B. A. Stach and V. Ramachandran, "Clinical audiology : An introduction," Plural Publishing, San Diego, CA, 2022.

[44] S. Hoth and I. Baljić, "Current audiological diagnostics," *GMS Curr. Top. Otorhinolaryngol. - Head Neck Surg.*, vol. 16, p. Doc09, Dec. 2017, doi: 10.3205/cto000148.

[45] The American Academy of Audiology, "Noise-induced hearing loss." https://www.audiology.org/consumers-and-patients/hearing-and-balance/hearing-induced-hearing-loss/ (accessed Mar. 21, 2023).

[46] C. Gralapp, "Coronal perspective of the anatomy of the ear." https://otosurgeryatlas.stanford.edu/otologic-surgery-atlas/surgical-anatomy-of-the-ear/overview-of-temporal-bone/#iLightbox[gallery_image_1]/0 (accessed Mar. 22, 2023).

[47] M. Gaihede and B. Koefoed-Nielsen, "Mechanics of the middle ear system: age-related changes in viscoelastic properties," *Audiol. Neurootol.*, vol. 5, no. 2, pp. 53–58, 2000, doi: 10.1159/000013867.

[48] N. Deep, E. Dowling, D. Jethanamest, and M. Carlson, "Cochlear Implantation: An Overview," *J. Neurol. Surg. Part B Skull Base*, vol. 80, no. 02, pp. 169–177, Apr. 2019, doi: 10.1055/s-0038-1669411.

[49] P. J. Yoon, "Pediatric cochlear implantation," *Curr. Opin. Pediatr.*, vol. 23, no. 3, pp. 346–350, Jun. 2011, doi: 10.1097/MOP.0b013e32834618ec.

[50] K. J. Cruickshanks *et al.*, "The 5-Year Incidence and Progression of Hearing Loss: The Epidemiology of Hearing Loss Study," *Arch. Otolaryngol. Neck Surg.*, vol. 129, no. 10, pp. 1041–1046, Oct. 2003, doi: 10.1001/ARCHOTOL.129.10.1041.

[51] M. Khairi Md Daud, R. M. Noor, N. A. Rahman, D. S. Sidek, and A. Mohamad, "The effect of mild hearing loss on academic performance in primary school children," *Int. J. Pediatr. Otorhinolaryngol.*, vol. 74, no. 1, pp. 67–70, Jan. 2010, doi: 10.1016/J.IJPORL.2009.10.013.

[52] E. M. Fitzpatrick *et al.*, "Hearing loss prevalence and hearing health among school-aged children in the Canadian Arctic," *Int. J. Audiol.*, vol. 60, no. 7, pp. 521–531, 2021, doi: 10.1080/14992027.2020.1731616.

[53] S. Asiri, A. Hasham, F. Al Anazy, S. Zakzouk, and A. Banjar, "Tympanosclerosis: review of literature and incidence among patients with middle-ear infection," *J. Laryngol. Otol.*, vol. 113, no. 12, pp. 1076–1080, 1999, doi: 10.1017/S0022215100157937.

[54] H. R. Djalilian *et al.*, "Optical Coherence Tomography of Cholesteatoma," *Otol. Neurotol.*, vol. 31, no. 6, pp. 932–935, Aug. 2010, doi: 10.1097/MAO.0b013e3181e711b8.

[55] F. Felici *et al.*, "Improved Assessment of Middle Ear Recurrent Cholesteatomas Using a Fusion of Conventional CT and Non-EPI-DWI MRI," *Am. J. Neuroradiol.*, vol. 40, no. 9, pp. 1546–1551, Aug. 2019, doi: 10.3174/ajnr.A6141.

[56] A. E. Moroco, R. A. Saadi, A. R. Baker, J. Zhu, and H. Isildak, "Usage Patterns of CT and MRI in the Evaluation of Otologic Disease," *Otol. Neurotol.*, vol. 42, no. 6, pp. e698–e708, Jul. 2021, doi: 10.1097/MAO.0000000000003095.

[57] L. Kirsten *et al.*, "Doppler optical coherence tomography as a promising tool for detecting fluid in the human middle ear," *Curr. Dir. Biomed. Eng.*, vol. 2, no. 1, pp. 443–447, Sep. 2016, doi: 10.1515/cdbme-2016-0098.

[58] J. Morgenstern *et al.*, "Endoscopic Optical Coherence Tomography for Evaluation of Success of Tympanoplasty," *Otol. Neurotol.*, vol. 41, no. 7, pp. e901–e905, Aug. 2020, doi: 10.1097/MAO.0000000000002486.

[59] I. Plouin-Gaudon, D. Bossard, S. Ayari-Khalfallah, and P. Froehlich, "Fusion of MRIs and CT Scans for Surgical Treatment of Cholesteatoma of the Middle Ear in Children," *Arch. Otolaryngol. Neck Surg.*, vol. 136, no. 9, p. 878, Sep. 2010, doi: 10.1001/archoto.2010.151.

[60] A. Kusak, O. Rosiak, M. Durko, P. Grzelak, and W. Pietruszewska, "Diagnostic imaging in chronic otitis media: does CT and MRI fusion aid therapeutic decision making? – a pilot study," *Otolaryngol. Pol.*, vol. 72, no. 5, pp. 1–5, Oct. 2018, doi: 10.5604/01.3001.0012.5423.

[61] A. Bayram, N. Bayar Muluk, C. Cingi, and S. A. Bafaqeeh, "Success rates for various graft materials in tympanoplasty - A review," *J. Otol.*, vol. 15, no. 3, pp. 107–111, Sep. 2020, doi: 10.1016/J.JOTO.2020.01.001.

[62] M. Tomasoni *et al.*, "Exploratory tympanotomy in conductive hearing loss with normal pre-operative investigations," *ACTA Otorhinolaryngol. Ital.*, vol. 42, no. 6, pp. 569–581, Dec. 2022, doi: 10.14639/0392-100X-N1933.

[63] R. Trevethan, "Sensitivity, Specificity, and Predictive Values: Foundations, Pliabilities, and Pitfalls in Research and Practice," *Front. Public Health*, vol. 5, p. 307, Nov. 2017, doi: 10.3389/FPUBH.2017.00307/BIBTEX.

[64] T. Frank and D. R. Petersen, "Accuracy of a 40 dB HL Audioscope and audiometer screening for adults," *Ear Hear.*, vol. 8, no. 3, pp. 180–183, 1987, doi: 10.1097/00003446-198706000-00009.

[65] R. CARHART, "Clinical application of bone conduction audiometry," *Arch. Otolaryngol.*, vol. 51, no. 6, pp. 798–808, 1950, doi: 10.1001/ARCHOTOL.1950.00700020824003.

[66] J. J. Rosowski *et al.*, "Ear-canal reflectance, umbo velocity, and tympanometry in normal-hearing adults," *Ear Hear.*, vol. 33, no. 1, pp. 19–34, Jan. 2012, doi: 10.1097/AUD.0B013E31822CCB76.

[67] C. A. Sanford, T. Schooling, and T. Frymark, "Determining the presence or absence of middle ear disorders: an evidence-based systematic review on the diagnostic accuracy of selected assessment instruments," *Am. J. Audiol.*, vol. 21, no. 2, pp. 251–268, 2012, doi: 10.1044/1059-0889(2012/11-0029).

[68] S. H. Bartling *et al.*, "Registration and Fusion of CT and MRI of the Temporal Bone," *J. Comput. Assist. Tomogr.*, vol. 29, no. 3, pp. 305–310, May 2005, doi: 10.1097/01.rct.0000160425.63884.5b.

[69] S. Manik, Y. Dabholkar, S. Bhalekar, H. Velankar, N. Chordia, and A. Saberwal, "Sensitivity and Specificity of High-Resolution Computed Tomography (HRCT) of Temporal Bone in Diagnosing Cholesteatoma and Its Correlation with Intraoperative Findings," *Indian J. Otolaryngol. Head Neck Surg.*, vol. 73, no. 1, p. 25, Mar. 2021, doi: 10.1007/S12070-020-01892-Z.

[70] C. L. Thukral, A. Singh, S. Singh, A. S. Sood, and K. Singh, "Role of High Resolution Computed Tomography in Evaluation of Pathologies of Temporal Bone," *J. Clin. Diagn. Res. JCDR*, vol. 9, no. 9, p. TC07, Sep. 2015, doi: 10.7860/JCDR/2015/12268.6508.

[71] H. S. Park, Y. E. Chung, and J. K. Seo, "Computed tomographic beam-hardening artefacts: mathematical characterization and analysis," *Philos. Transact. A Math. Phys. Eng. Sci.*, vol. 373, no. 2043, Jun. 2015, doi: 10.1098/RSTA.2014.0388.

[72] K. Yamashita *et al.*, "High-resolution three-dimensional diffusion-weighted MRI/CT image data fusion for cholesteatoma surgical planning: a feasibility study," *Eur. Arch. Otorhinolaryngol.*, vol. 272, no. 12, pp. 3821–3824, Dec. 2015, doi: 10.1007/s00405-014-3467-7.

[73] F. Zhao *et al.*, "Magnetic susceptibility artefact on MRI mimicking lymphadenopathy: description of a nasopharyngeal carcinoma patient," *Transl. Cancer Res.*, vol. 6, no. 6, pp. 1156–1161, Dec. 2017, doi: 10.21037/TCR.2017.09.16.

[74] H. A. Edmonson, M. L. Carlson, A. C. Patton, and R. E. Watson, "MR imaging and cochlear implants with retained internal magnets: Reducing artifacts near highly inhomogeneous magnetic fields," *Radiographics*, vol. 38, no. 1, pp. 94–106, Jan. 2018, doi: 10.1148/RG.2018170135/ASSET/IMAGES/LARGE/RG.2018170135.FIG10D.JPEG.

[75] J. J. Rosowski, H. H. Nakajima, and S. N. Merchant, "Clinical utility of laser-Doppler vibrometer measurements in live normal and pathologic human ears," *Ear Hear.*, vol. 29, no. 1, pp. 3–19, Jan. 2008, doi: 10.1097/AUD.0B013E31815D63A5.

[76] G. Robertson and R. Mills, "Findings at exploratory tympanotomy for conductive hearing loss," *J. Laryngol. Otol.*, vol. 123, no. 10, pp. 1087–1089, Oct. 2009, doi: 10.1017/S0022215109005696.

[77] B. C. A. van Stekelenburg and M. C. J. Aarts, "Determinants influencing success rates of myringoplasty in daily practice: a retrospective analysis," *Eur. Arch. Oto-Rhino-Laryngol. Off. J. Eur. Fed. Oto-Rhino-Laryngol. Soc. EUFOS Affil. Ger. Soc. Oto-Rhino-Laryngol. - Head Neck Surg.*, vol. 276, no. 11, pp. 3081–3087, Nov. 2019, doi: 10.1007/S00405-019-05611-5.

[78] U. Fisch, G. Ö. Acar, and A. M. Huber, "Malleostapedotomy in revision surgery for otosclerosis," *Otol. Neurotol. Off. Publ. Am. Otol. Soc. Am. Neurotol. Soc. Eur. Acad. Otol. Neurotol.*, vol. 22, no. 6, pp. 776–785, 2001, doi: 10.1097/00129492-200111000-00011.

[79] K. Nateghifard *et al.*, "Cone beam CT for perioperative imaging in hearing preservation Cochlear implantation - A human cadaveric study," *J. Otolaryngol. - Head Neck Surg.*, vol. 48, no. 1, pp. 1–8, Nov. 2019, doi: 10.1186/S40463-019-0388-X/TABLES/3.

[80] M. Wojtkowski, "High-speed optical coherence tomography: basics and applications," *Appl. Opt.*, vol. 49, no. 16, p. D30, Jun. 2010, doi: 10.1364/AO.49.000D30.

[81] W. Drexler and J. G. Fujimoto, *Optical Coherence Tomography Technology and Applications*, 2nd ed. Switzerland: Springer, Cham, 2015. [Online]. Available: https://doi.org/10.1007/978-3-319-06419-2

[82] W. Drexler and J. G. Fujimoto, Eds., *Optical Coherence Tomography: Technology and Applications*. Cham: Springer International Publishing, 2015. doi: 10.1007/978-3-319-06419-2.

[83] A. Gh. Podoleanu, "Optical coherence tomography," *J. Microsc.*, vol. 247, no. 3, pp. 209–219, Sep. 2012, doi: 10.1111/j.1365-2818.2012.03619.x.

[84] R. K. Wang, "Resolution improved optical coherence-gated tomography for imaging through biological tissues," *J. Mod. Opt.*, vol. 46, no. 13, pp. 1905–1912, 1999, doi: 10.1080/09500349908231380.

[85] B. Liu and M. E. Brezinski, "Theoretical and practical considerations on detection performance of time domain, Fourier domain, and swept source optical coherence tomography," *J. Biomed. Opt.*, vol. 12, no. 4, p. 044007, 2007, doi: 10.1117/1.2753410.

[86] J. Fujimoto and E. Swanson, "The Development, Commercialization, and Impact of Optical Coherence Tomography," *Invest. Ophthalmol. Vis. Sci.*, vol. 57, no. 9, p. OCT1, 2016, doi: 10.1167/IOVS.16-19963.

[87] A. F. Fercher, W. Drexler, C. K. Hitzenberger, and T. Lasser, "Optical coherence tomography - principles and applications," *Rep. Prog. Phys.*, vol. 66, no. 2, pp. 239–303, Feb. 2003, doi: 10.1088/0034-4885/66/2/204.

[88] B. C. Quirk, R. A. McLaughlin, A. Curatolo, R. W. Kirk, P. B. Noble, and D. D. Sampson, "In situ imaging of lung alveoli with an optical coherence tomography needle probe," *J. Biomed. Opt.*, vol. 16, no. 3, p. 036009, 2011, doi: 10.1117/1.3556719.

[89] Z. Hamdoon, W. Jerjes, R. Al-Delayme, G. McKenzie, A. Jay, and C. Hopper, "Structural validation of oral mucosal tissue using optical coherence tomography," *Head Neck Oncol.*, vol. 4, no. 1, p. 29, Dec. 2012, doi: 10.1186/1758-3284-4-29.

[90] J. A. Burns, "Optical coherence tomography: Imaging the larynx," *Curr. Opin. Otolaryngol. Head Neck Surg.*, vol. 20, no. 6, pp. 477–481, Dec. 2012, doi: 10.1097/MOO.0b013e3283582d7d.

[91] M. Machoy, J. Seeliger, L. Szyszka-Sommerfeld, R. Koprowski, T. Gedrange, and K. Woźniak, "The use of optical coherence tomography in dental diagnostics: A state-of-the-art review," *J. Healthc. Eng.*, vol. 2017, pp. 1–31, 2017, doi: 10.1155/2017/7560645.

[92] M. E. Brezinski, *Optical coherence tomography: principles and applications*. Amsterdam ; Boston: Academic Press, 2006.

[93] A. V. Arecchi, R. J. Koshel, and T. Messadi, *Field guide to illumination*. in SPIE field guides, no. FG11. Bellingham, Wash: SPIE, 2007.

[94] D. P. Popescu *et al.*, "Optical coherence tomography: fundamental principles, instrumental designs and biomedical applications," *Biophys. Rev.*, vol. 3, no. 3, pp. 155–169, Sep. 2011, doi: 10.1007/s12551-011-0054-7.

[95] M. Choma, M. Sarunic, C. Yang, and J. Izatt, "Sensitivity advantage of swept source and Fourier domain optical coherence tomography," *Opt. Express*, vol. 11, no. 18, p. 2183, Sep. 2003, doi: 10.1364/OE.11.002183.

[96] R. Leitgeb, A. F. Fercher, and C. K. Hitzenberger, "Performance of fourier domain vs. time domain optical coherence tomography," *Opt. Express Vol 11 Issue 8 Pp 889-894*, vol. 11, no. 8, pp. 889–894, Apr. 2003, doi: 10.1364/OE.11.000889.

[97] P. H. Tomlins and R. K. Wang, "Theory, developments and applications of optical coherence tomography," *J. Phys. Appl. Phys.*, vol. 38, no. 15, pp. 2519–2535, Aug. 2005, doi: 10.1088/0022-3727/38/15/002.

[98] F. L. Pedrotti, L. M. Pedrotti, and L. S. Pedrotti, *Introduction to Optics:*, 3rd ed. Cambridge University Press, 2017. doi: 10.1017/9781108552493.

[99] M. Bonesi *et al.*, "Akinetic all-semiconductor programmable swept-source at 1550 nm and 1310 nm with centimeters coherence length," *Opt. Express*, vol. 22, no. 3, p. 2632, Feb. 2014, doi: 10.1364/OE.22.002632.

[100] J. Kalkman, "Fourier-domain optical coherence tomography signal analysis and numerical modeling," *Int. J. Opt.*, vol. 2017, pp. 1–16, 2017, doi: 10.1155/2017/9586067.

[101] R. K. Wang and L. An, "Doppler optical micro-angiography for volumetric imaging of vascular perfusion in vivo," *Opt. Express Vol 17 Issue 11 Pp 8926-8940*, vol. 17, no. 11, pp. 8926–8940, May 2009, doi: 10.1364/OE.17.008926.

[102] B. C. Quirk, L. Scolaro, D. D. Sampson, D. Lorenser, R. W. Kirk, and R. A. McLaughlin, "High-sensitivity anastigmatic imaging needle for optical coherence tomography," *Opt. Lett. Vol 37 Issue 24 Pp 5247-5249*, vol. 37, no. 24, pp. 5247–5249, Dec. 2012, doi: 10.1364/OL.37.005247.

[103] W.-C. Kuo *et al.*, "Balanced detection for spectral domain optical coherence tomography," *Opt. Express Vol 21 Issue 16 Pp 19280-19291*, vol. 21, no. 16, pp. 19280–19291, Aug. 2013, doi: 10.1364/OE.21.019280.

[104] C. S. Seelamantula, M. L. Villiger, M. Unser, and R. A. Leitgeb, "Exact and efficient signal reconstruction in frequency-domain optical-coherence tomography," *JOSA Vol 25 Issue 7 Pp 1762-1771*, vol. 25, no. 7, pp. 1762–1771, Jul. 2008, doi: 10.1364/JOSAA.25.001762.

[105] S. R. Chinn, E. A. Swanson, and J. G. Fujimoto, "Optical coherence tomography using a frequency-tunable optical source," *Opt. Lett.*, vol. 22, no. 5, p. 340, Mar. 1997, doi: 10.1364/OL.22.000340.

[106] D. MacDougall, J. Farrell, J. Brown, M. Bance, and R. Adamson, "Long-range, wide-field swept-source optical coherence tomography with GPU accelerated digital lock-in Doppler vibrography for real-time, in vivo middle ear diagnostics," *Biomed. Opt. Express*, vol. 7, no. 11, p. 4621, Nov. 2016, doi: 10.1364/BOE.7.004621.

[107] T. Klein and R. Huber, "High-speed OCT light sources and systems [Invited]," *Biomed. Opt. Express*, vol. 8, no. 2, p. 828, Feb. 2017, doi: 10.1364/BOE.8.000828.

[108] E. Bousi and C. Pitris, "Axial resolution improvement by modulated deconvolution in Fourier domain optical coherence tomography," *J. Biomed. Opt.*, vol. 17, no. 7, p. 071307, May 2012, doi: 10.1117/1.JBO.17.7.071307.

[109] D. Piao, Q. Zhu, N. K. Dutta, S. Yan, and L. L. Otis, "Cancellation of coherent artifacts in optical coherence tomography imaging," *Appl. Opt.*, vol. 40, no. 28, p. 5124, Oct. 2001, doi: 10.1364/AO.40.005124.

[110] A. V. Oppenheim, *Discrete-time signal processing*. Prentice Hall Press, 2010.

[111] Y. Wang, Y. Liang, and K. Xu, "Signal processing for sidelobe suppression in optical coherence tomography images," *J. Opt. Soc. Am. A*, vol. 27, no. 3, p. 415, Mar. 2010, doi: 10.1364/JOSAA.27.000415.

[112] Y. Chen, J. Fingler, and S. E. Fraser, "Multi-shaping technique reduces sidelobe magnitude in optical coherence tomography," *Biomed. Opt. Express*, vol. 8, no. 11, p. 5267, Nov. 2017, doi: 10.1364/BOE.8.005267.

[113] X. Yu, X. Liu, J. Gu, D. Cui, J. Wu, and L. Liu, "Depth extension and sidelobe suppression in optical coherence tomography using pupil filters," *Opt. Express*, vol. 22, no. 22, p. 26956, Nov. 2014, doi: 10.1364/OE.22.026956.

[114] S. Song, J. Xu, and R. K. Wang, "Long-range and wide field of view optical coherence tomography for in vivo 3D imaging of large volume object based on akinetic programmable swept source," *Biomed. Opt. Express*, vol. 7, no. 11, p. 4734, Nov. 2016, doi: 10.1364/BOE.7.004734.

[115] K. F. Renk, *Basics of Laser Physics*. in Graduate Texts in Physics. Berlin, Heidelberg: Springer Berlin Heidelberg, 2012. doi: 10.1007/978-3-642-23565-8.

[116] B. E. A. Saleh and M. C. Teich, *Fundamentals of Photonics*. in Wiley Series in Pure and Applied Optics. New York, USA: John Wiley & Sons, Inc., 1991. doi: 10.1002/0471213748.

[117] V. R. Shidlovski, "Superluminescent diode light sources for OCT," *Opt. Coherence Tomogr. Technol. Appl. Second Ed.*, pp. 505–526, Jan. 2015, doi: 10.1007/978-3-319-06419-2_18/COVER.

[118] V. Jayaraman *et al.*, "VCSEL Swept Light Sources," in *Optical Coherence Tomography*, Cham: Springer International Publishing, 2015, pp. 659–686. doi: 10.1007/978-3-319-06419-2_23.

[119] M. P. Minneman, J. Ensher, M. Crawford, and D. Derickson, "All-semiconductor high-speed akinetic swept-source for OCT," in *Optics InfoBase Conference Papers*, J. Popp, Ed., Nov. 2011, p. 831116. doi: 10.1117/12.912119.

[120] T. A. Heumier and J. L. Carlsten, "Mode Hopping in Semiconductor Lasers."

[121] J. Ensher *et al.*, "Long coherence length and linear sweep without an external optical k-clock in a monolithic semiconductor laser for inexpensive optical coherence tomography," in *Optical Coherence Tomography and Coherence Domain Optical Methods in Biomedicine XVI*, J. A. Izatt, J. G. Fujimoto, and V. V. Tuchin, Eds., SPIE, Feb. 2012, p. 82130T. doi: 10.1117/12.911477.

[122] S. Moon and Z. Chen, "Phase-stability optimization of swept-source optical coherence tomography," *Biomed. Opt. Express*, vol. 9, no. 11, p. 5280, Nov. 2018, doi: 10.1364/BOE.9.005280.

[123] B. E. Applegate *et al.*, "In vivo functional imaging of the human middle ear with a hand-held optical coherence tomography device," *Biomed. Opt. Express Vol 12 Issue 8 Pp 5196-5213*, vol. 12, no. 8, pp. 5196–5213, Aug. 2021, doi: 10.1364/BOE.430935.

[124] >Hans Wilhelm Pau, E. Lankenau, T. Just, D. Behrend, and G. Hüttmann, "Optical coherence tomography as an orientation guide in cochlear implant surgery?," *Acta Otolaryngol. (Stockh.)*, vol. 127, no. 9, pp. 907–913, Jan. 2007, doi: 10.1080/00016480601089408.

[125] C. T. Nguyen *et al.*, "Noninvasive in vivo optical detection of biofilm in the human middle ear," *Proc. Natl. Acad. Sci.*, vol. 109, no. 24, pp. 9529–9534, Jun. 2012, doi: 10.1073/pnas.1201592109.

[126] N. H. Cho, S. H. Lee, W. Jung, J. H. Jang, and J. Kim, "Optical Coherence Tomography for the Diagnosis and Evaluation of Human Otitis Media," *J. Korean Med. Sci.*, vol. 30, no. 3, p. 328, 2015, doi: 10.3346/jkms.2015.30.3.328.

[127] G. L. Monroy *et al.*, "Noninvasive depth-resolved optical measurements of the tympanic membrane and middle ear for differentiating otitis media: Differentiation of Otitis Media Using OCT," *The Laryngoscope*, vol. 125, no. 8, pp. E276–E282, Aug. 2015, doi: 10.1002/lary.25141.

[128] D. Preciado *et al.*, "Otitis Media Middle Ear Effusion Identification and Characterization Using an Optical Coherence Tomography Otoscope," *Otolaryngol. Neck Surg.*, vol. 162, no. 3, pp. 367–374, Mar. 2020, doi: 10.1177/0194599819900762.

[129] J. Lee *et al.*, "Clinical Utility of Intraoperative Tympanomastoidectomy Assessment Using a Surgical Microscope Integrated with an Optical Coherence Tomography," *Sci. Rep.*, vol. 8, no. 1, p. 17432, Nov. 2018, doi: 10.1038/s41598-018-35563-5.

[130] J. Wang *et al.*, "Transtympanic Visualization of Cochlear Implant Placement With Optical Coherence Tomography: A Pilot Study," *Otol. Neurotol.*, vol. 43, no. 8, pp. e824–e828, Sep. 2022, doi: 10.1097/MAO.0000000000003635.

[131] J. Wang *et al.*, "Optical Clearing Agents for Optical Imaging Through Cartilage Tympanoplasties: A Preclinical Feasibility Study," *Otol. Neurotol.*, vol. 43, no. 4, pp. e467–e474, Apr. 2022, doi: 10.1097/MAO.0000000000003502.

[132] M. E. Pawlowski, S. Shrestha, J. Park, B. E. Applegate, J. S. Oghalai, and T. S. Tkaczyk, "Miniature, minimally invasive, tunable endoscope for investigation of the middle ear," *Biomed. Opt. Express*, vol. 6, no. 6, p. 2246, Jun. 2015, doi: 10.1364/BOE.6.002246.

[133] J. Won *et al.*, "Longitudinal optical coherence tomography to visualize the in vivo response of middle ear biofilms to antibiotic therapy," *Sci. Rep. 2021 111*, vol. 11, no. 1, pp. 1–13, Mar. 2021, doi: 10.1038/s41598-021-84543-9.

[134] D. R. Macdougall, "Optical Coherence Tomography for Clinical Otology," Dalhousie University, 2020.

[135] J. D. Farrell *et al.*, "Geometrically accurate real-time volumetric visualization of the middle ear using optical coherence tomography," *Biomed. Opt. Express*, vol. 14, no. 7, p. 3152, Jul. 2023, doi: 10.1364/BOE.488845.

[136] P. A. Shilyagin, A. A. Novozhilov, T. E. Abubakirov, G. V. Gelikonov, A. V. Shakhov, and V. M. Gelikonov, "Optical coherence tomography in otitis media with effusion diagnosing," in *Optical Coherence Imaging Techniques and Imaging in Scattering Media III*, S. A. Boppart, M. Wojtkowski, and W.-Y. Oh, Eds., SPIE, Jul. 2019, p. 26. doi: 10.1117/12.2527147.

[137] L. Kerkhofs, A. Starovoyt, J. Wouters, T. Putzeys, and N. Verhaert, "Optical Coherence Tomography-Based Atlas of the Human Cochlear Hook Region," *J. Clin. Med.*, vol. 12, no. 1, p. 238, Dec. 2022, doi: 10.3390/jcm12010238.

[138] H. Debrégeas, "Widely tunable laser diodes," in *Springer Series in Optical Sciences*, Springer Verlag, 2017, pp. 209–248. doi: 10.1007/978-3-319-42367-8_5/COVER.

[139] Thorlabs Inc, "Protected Gold Mirrors." https://www.thorlabs.com (accessed Jun. 15, 2023).

[140] Edmund Optics, "UV-VIS Neutral Density (ND) Filters." https://www.edmundoptics.com/f/uv-vis-neutral-density-nd-filters/12715/

[141] Insight Photonic Solutions, Inc., "Clean Optical Performance." https://www.sweptlaser.com/clean-optical-performance

[142] S. Kim, J. S. Oghalai, and B. E. Applegate, "Noise and sensitivity in optical coherence tomography based vibrometry," *Opt. Express*, vol. 27, no. 23, p. 33333, Nov. 2019, doi: 10.1364/OE.27.033333.

[143] T. H. Ko *et al.*, "Ultrahigh resolution optical coherence tomography imaging with a broadband superluminescent diode light source," *Opt. Express Vol 12 Issue 10 Pp 2112-2119*, vol. 12, no. 10, pp. 2112–2119, May 2004, doi: 10.1364/OPEX.12.002112.

[144] J. Wang, B. Wohlberg, and R. B. A. Adamson, "Convolutional dictionary learning for blind deconvolution of optical coherence tomography images," *Biomed. Opt. Express*, vol. 13, no. 4, p. 1834, Apr. 2022, doi: 10.1364/BOE.447394.

[145] C. Pitris *et al.*, "In vivo ultrahigh-resolution optical coherence tomography," *Opt. Lett. Vol 24 Issue 17 Pp 1221-1223*, vol. 24, no. 17, pp. 1221–1223, Sep. 1999, doi: 10.1364/OL.24.001221.

[146] A. C. Akcay, J. P. Rolland, and J. M. Eichenholz, "Spectral shaping to improve the point spread function in optical coherence tomography," *Opt. Lett.*, vol. 28, no. 20, p. 1921, Oct. 2003, doi: 10.1364/OL.28.001921.

[147] R. Tripathi, N. Nassif, J. S. Nelson, B. H. Park, and J. F. de Boer, "Spectral shaping for non-Gaussian source spectra in optical coherence tomography," *Opt. Lett.*, vol. 27, no. 6, p. 406, Mar. 2002, doi: 10.1364/OL.27.000406.

[148] S. A. Hojjatoleslami, M. R. N. Avanaki, and A. G. Podoleanu, "Image quality improvement in optical coherence tomography using Lucy–Richardson deconvolution algorithm," *Appl. Opt.*, vol. 52, no. 23, p. 5663, Aug. 2013, doi: 10.1364/AO.52.005663.

[149] P. D. Woolliams, R. A. Ferguson, C. Hart, A. Grimwood, and P. H. Tomlins, "Spatially deconvolved optical coherence tomography," *Appl. Opt.*, vol. 49, no. 11, p. 2014, Apr. 2010, doi: 10.1364/AO.49.002014.

[150] J. M. Schmitt, "Restoration of optical coherence images of living tissue using the CLEAN algorithm," *J. Biomed. Opt.*, vol. 3, no. 1, p. 66, Jan. 1998, doi: 10.1117/1.429863.

[151] R. C. Gonzalez and R. E. Woods, "Digital Image Processing, Global Edition," in *Digital Image Processing, Global Edition*, 2017, p. 1024.

[152] S. S. Chen, D. L. Donoho, and M. A. Saunders, "Atomic decomposition by basis pursuit," *SIAM Rev.*, vol. 43, no. 1, pp. 129–159, Jan. 2001, doi: 10.1137/S003614450037906X.

[153] H. Hindi, "A tutorial on convex optimization," in *Proceedings of the 2004 American Control Conference*, Boston, MA, USA: IEEE, 2004, pp. 3252–3265 vol.4. doi: 10.23919/ACC.2004.1384411.

[154] S. Boyd and L. Vandenberghe, *Convex Optimization*, 1st ed. Cambridge University Press, 2004. doi: 10.1017/CBO9780511804441.

[155] T. Akasaka *et al.*, "Optimization of regularization parameters in compressed sensing of magnetic resonance angiography: Can statistical image metrics mimic radiologists' perception?," *PLoS ONE*, vol. 11, no. 1, Jan. 2016, doi: 10.1371/journal.pone.0146548.

[156] H. Bristow and S. Lucey, "Optimization methods for convolutional sparse coding," Jun. 2014, [Online]. Available: http://arxiv.org/abs/1406.2407

[157] S. Boyd, "Distributed Optimization and Statistical Learning via the Alternating Direction Method of Multipliers," *Found. Trends® Mach. Learn.*, vol. 3, no. 1, pp. 1–122, 2010, doi: 10.1561/2200000016.

[158] Y. Chen, D. M. de Bruin, C. Kerbage, and J. F. de Boer, "Spectrally balanced detection for optical frequency domain imaging," *Opt. Express*, vol. 15, no. 25, p. 16390, 2007, doi: 10.1364/OE.15.016390.

[159] Sé. Bourguignon, H. Carfantan, and Jé. Idier, "A Sparsity-Based Method for the Estimation of Spectral Lines From Irregularly Sampled Data," *IEEE J. Sel. Top. Signal Process.*, vol. 1, no. 4, pp. 575–585, Dec. 2007, doi: 10.1109/JSTSP.2007.910275.

[160] N. Mohan, I. Stojanovic, W. C. Karl, B. E. A. Saleh, and M. C. Teich, "Compressed sensing in optical coherence tomography," in *Three-Dimensional and Multidimensional Microscopy: Image Acquisition and Processing XVII*, J.-A. Conchello, C. J. Cogswell, T. Wilson, and T. G. Brown, Eds., Feb. 2010, p. 75700L. doi: 10.1117/12.844217.

[161] X. Liu and J. U. Kang, "Compressive SD-OCT: the application of compressed sensing in spectral domain optical coherence tomography," *Opt. Express*, vol. 18, no. 21, p. 22010, Oct. 2010, doi: 10.1364/OE.18.022010.

[162] J. Nešetřil and P. Ossona de Mendez, *Sparsity*, vol. 28, no. 1–2. in Algorithms and Combinatorics, vol. 28. Berlin, Heidelberg: Springer Berlin Heidelberg, 2012. doi: 10.1007/978-3-642-27875-4.

[163] D. L. Donoho, "Compressed sensing," *IEEE Trans. Inf. Theory*, vol. 52, no. 4, pp. 1289–1306, Apr. 2006, doi: 10.1109/TIT.2006.871582.

[164] B. Wohlberg, "Efficient algorithms for convolutional sparse representations," *IEEE Trans. Image Process.*, vol. 25, no. 1, pp. 301–315, Jan. 2016, doi: 10.1109/TIP.2015.2495260.

[165] T. Blumensath and M. Davies, "Sparse and shift-invariant representations of music," *IEEE Trans. Audio Speech Lang. Process.*, vol. 14, no. 1, pp. 50–57, Jan. 2006, doi: 10.1109/TSA.2005.860346.

[166] Z. Zhang, Y. Xu, J. Yang, X. Li, and D. Zhang, "A Survey of Sparse Representation: Algorithms and Applications," *IEEE Access*, vol. 3, pp. 490–530, 2015, doi: 10.1109/ACCESS.2015.2430359.

[167] L. Tawade, A. B. Aboobacker, and F. Ghante, "Image fusion based on wavelet transforms," *Int. J. Bio-Sci. Bio-Technol.*, vol. 6, no. 3, pp. 149–162, 2014, doi: 10.14257/ijbsbt.2014.6.3.18.

[168] Han Chumning, Guo Huadong, and Wang Changlin, "Edge preservation evaluation of digital speckle filters," in *IEEE International Geoscience and Remote Sensing Symposium*, Toronto, Ont., Canada: IEEE, 2002, pp. 2471–2473. doi: 10.1109/IGARSS.2002.1026581.

[169] W. Hashimoto and K. Kurata, "Properties of basis functions generated by shift invariant sparse representations of natural images," *Biol. Cybern.*, vol. 83, no. 2, pp. 111–118, Jul. 2000, doi: 10.1007/s004220000149.

[170] J. Dong, W. Wang, and J. Chambers, "Audio super-resolution using analysis dictionary learning," in *2015 IEEE International Conference on Digital Signal Processing (DSP)*, IEEE, Jul. 2015, pp. 604–608. doi: 10.1109/ICDSP.2015.7251945.

[171] H. Hongxing, J. M. Bioucas-Dias, and V. Katkovnik, "Interferometric phase image estimation via sparse coding in the complex domain," *IEEE Trans. Geosci. Remote Sens.*, vol. 53, no. 5, pp. 2587–2602, May 2015, doi: 10.1109/TGRS.2014.2361919.

[172] S. Gu, W. Zuo, Q. Xie, D. Meng, X. Feng, and L. Zhang, "Convolutional sparse coding for image super-resolution," in *2015 IEEE International Conference on Computer Vision (ICCV)*, IEEE, Dec. 2015, pp. 1823–1831. doi: 10.1109/ICCV.2015.212.

[173] M. Srinivas, D. Roy, and C. K. Mohan, "Learning sparse dictionaries for music and speech classification," in *2014 19th International Conference on Digital Signal Processing*, IEEE, Aug. 2014, pp. 673–675. doi: 10.1109/ICDSP.2014.6900749.

[174] G.-M. Zhang, C.-Z. Zhang, and D. M. Harvey, "Sparse signal representation and its applications in ultrasonic NDE," *Ultrasonics*, vol. 52, no. 3, pp. 351–363, Mar. 2012, doi: 10.1016/j.ultras.2011.10.001.

[175] C. Ekanadham, D. Tranchina, and E. P. Simoncelli, "A blind deconvolution method for neural spike identification," *Adv. Neural Inf. Process. Syst. 24 25th Annu. Conf. Neural Inf. Process. Syst. 2011 NIPS 2011*, pp. 1–9, 2011.

[176] C. Garcia-Cardona and B. Wohlberg, "Convolutional dictionary learning: A comparative review and new algorithms," *IEEE Trans. Comput. Imaging*, vol. 4, no. 3, pp. 366–381, Sep. 2018, doi: 10.1109/TCI.2018.2840334.

[177] G. Liu, S. Yousefi, Z. Zhi, and R. K. Wang, "Automatic estimation of point-spread-function for deconvoluting out-of-focus optical coherence tomographic images using information entropy-based approach," *Opt. Express*, vol. 19, no. 19, p. 18135, Sep. 2011, doi: 10.1364/OE.19.018135.

[178] D. Kundur and D. Hatzinakos, "Blind image deconvolution," *IEEE Signal Process. Mag.*, vol. 13, no. 3, pp. 43–64, May 1996, doi: 10.1109/79.489268.

[179] A. A. Moiseev, G. V. Gelikonov, P. A. Shilyagin, and V. M. Gelikonov, "Blind deconvolution algorithm for restoration OCT images with diffraction limited resolution," in *https://doi.org/10.1117/12.889731*, R. A. Leitgeb and B. E. Bouma, Eds., SPIE, Jun. 2011, p. 80911W. doi: 10.1117/12.889731.

[180] K. Shen, H. Lu, S. Baig, and M. R. Wang, "Improving lateral resolution and image quality of optical coherence tomography by the multi-frame superresolution technique for 3D tissue imaging," *Biomed. Opt. Express*, vol. 8, no. 11, p. 4887, Nov. 2017, doi: 10.1364/BOE.8.004887.

[181] B. Wohlberg and P. Wozniak, "PSF Estimation in crowded astronomical imagery as a convolutional dictionary learning problem," *IEEE Signal Process. Lett.*, vol. 28, pp. 374–378, 2021, doi: 10.1109/LSP.2021.3050706.

[182] D. L. Donoho and M. Elad, "Optimally sparse representation in general (nonorthogonal) dictionaries via \ell_1 minimization," *Proc. Natl. Acad. Sci.*, vol. 100, no. 5, pp. 2197–2202, Mar. 2003, doi: 10.1073/pnas.0437847100.

[183] L. Fang, S. Li, Q. Nie, J. A. Izatt, C. A. Toth, and S. Farsiu, "Sparsity based denoising of spectral domain optical coherence tomography images," *Biomed. Opt. Express*, vol. 3, no. 5, p. 927, May 2012, doi: 10.1364/BOE.3.000927.

[184] Y. C. Eldar, *Compressed Sensing*. Cambridge: Cambridge University Press, 2012. doi: 10.1017/CBO9780511794308.

[185] S. L. Brunton, J. L. Proctor, and J. N. Kutz, "Discovering governing equations from data by sparse identification of nonlinear dynamical systems," *Proc. Natl. Acad. Sci.*, vol. 113, no. 15, pp. 3932–3937, Apr. 2016, doi: 10.1073/pnas.1517384113.

[186] B. A. Olshausen, "Learning sparse, overcomplete representations of time-varying natural images," in *Proceedings 2003 International Conference on Image Processing (Cat. No.03CH37429)*, IEEE, 2003, p. I-41–4. doi: 10.1109/ICIP.2003.1246893.

[187] M. Lewicki and T. Sejnowski, "Coding time-varying signals using sparse, shift-invariant representations," in *Advances in Neural Information Processing Systems 11 (NIPS 1998)*, 1998.

[188] A. Cogliati, Z. Duan, and B. Wohlberg, "Context-dependent piano music transcription with convolutional sparse coding," *IEEEACM Trans. Audio Speech Lang. Process.*, vol. 24, no. 12, pp. 2218–2230, Dec. 2016, doi: 10.1109/TASLP.2016.2598305.

[189] A. Cogliati, Z. Duan, and B. Wohlberg, "Piano music transcription with fast convolutional sparse coding," in *2015 IEEE 25th International Workshop on Machine Learning for Signal Processing (MLSP)*, IEEE, Sep. 2015, pp. 1–6. doi: 10.1109/MLSP.2015.7324332.

[190] C. Liu, A. Wong, K. Bizheva, P. Fieguth, and H. Bie, "Homotopic, non-local sparse reconstruction of optical coherence tomography imagery," *Opt. Express*, vol. 20, no. 9, p. 10200, Apr. 2012, doi: 10.1364/OE.20.010200.

[191] M. Shamouilian and I. Selesnick, "Total Variation Denoising for Optical Coherence Tomography," in *2019 IEEE Signal Processing in Medicine and Biology Symposium (SPMB)*, Philadelphia, PA, USA: IEEE, Dec. 2019, pp. 1–5. doi: 10.1109/SPMB47826.2019.9037832.

[192] L. Fang, S. Li, X. Kang, J. A. Izatt, and S. Farsiu, "3-D Adaptive Sparsity Based Image Compression With Applications to Optical Coherence Tomography," *IEEE Trans. Med. Imaging*, vol. 34, no. 6, pp. 1306–1320, Jun. 2015, doi: 10.1109/TMI.2014.2387336.

[193] Y. Ling *et al.*, "Beyond Fourier transform: super-resolving optical coherence tomography," Jan. 2020, Accessed: Feb. 04, 2022. [Online]. Available: https://arxiv.org/abs/2001.03129v3

[194] L. Vinet and A. Zhedanov, "A 'missing' family of classical orthogonal polynomials," *J. Phys. Math. Theor.*, vol. 44, no. 8, p. 085201, Feb. 2011, doi: 10.1088/1751-8113/44/8/085201.

[195] B. Wohlberg, "Efficient convolutional sparse coding," in *2014 IEEE International Conference on Acoustics, Speech and Signal Processing (ICASSP)*, IEEE, May 2014, pp. 7173–7177. doi: 10.1109/ICASSP.2014.6854992.

[196] A. Cameron, D. Lui, A. Boroomand, J. Glaister, A. Wong, and K. Bizheva, "Stochastic speckle noise compensation in optical coherence tomography using non-stationary spline-based speckle noise modelling," *Biomed. Opt. Express*, vol. 4, no. 9, p. 1769, Sep. 2013, doi: 10.1364/BOE.4.001769.

[197] C. Garcia-Cardona and B. Wohlberg, "Subproblem coupling in convolutional dictionary learning," in *2017 IEEE International Conference on Image Processing (ICIP)*, IEEE, Sep. 2017, pp. 1697–1701. doi: 10.1109/ICIP.2017.8296571.

[198] J. F. C. Mota, J. M. F. Xavier, P. M. Q. Aguiar, and M. Puschel, "Distributed Basis Pursuit," *IEEE Trans. Signal Process.*, vol. 60, no. 4, pp. 1942–1956, Apr. 2012, doi: 10.1109/TSP.2011.2182347.

[199] T. Liu *et al.*, "ADMM based low-rank and sparse matrix recovery method for sparse photoacoustic microscopy," *Biomed. Signal Process. Control*, vol. 52, pp. 14–22, Jul. 2019, doi: 10.1016/j.bspc.2019.03.007.

[200] B. Wohlberg, "ADMM Penalty Parameter Selection by Residual Balancing," 2017, doi: 10.48550/ARXIV.1704.06209.

[201] J. Kang, D. Hong, J. Liu, G. Baier, N. Yokoya, and B. Demir, "Learning convolutional sparse coding on complex domain for interferometric phase restoration," *IEEE Trans. Neural Netw. Learn. Syst.*, vol. 32, no. 2, pp. 826–840, Feb. 2021, doi: 10.1109/TNNLS.2020.2979546.

[202] B. Wohlberg, "SPORCO: A Python package for standard and convolutional sparse representations," in *Proceedings of the 16th Python in Science Conference*, SciPy, 2017, pp. 1–8. doi: 10.25080/shinma-7f4c6e7-001.

[203] J. Wang and R. Adamson, "young-oct/OCT-sparse-estimation-with-CBPDN-framework," 2021. https://github.com/young-oct/OCT-sparse-estimation-with-CBPDN-framework (accessed Mar. 09, 2021).

[204] S. Moon, S.-W. Lee, and Z. Chen, "Reference spectrum extraction and fixed-pattern noise removal in optical coherence tomography," *Opt. Express*, vol. 18, no. 24, p. 24395, Nov. 2010, doi: 10.1364/OE.18.024395.

[205] Z. Wang, A. C. Bovik, H. R. Sheikh, and E. P. Simoncelli, "Image quality assessment: from error visibility to structural similarity," *IEEE Trans. Image Process.*, vol. 13, no. 4, pp. 600–612, Apr. 2004, doi: 10.1109/TIP.2003.819861.

[206] C. H. Gierull and I. C. Sikaneta, "Estimating the effective number of looks in interferometric SAR data," *IEEE Trans. Geosci. Remote Sens.*, vol. 40, no. 8, pp. 1733–1742, Aug. 2002, doi: 10.1109/TGRS.2002.802457.

[207] K. Wang, Z. Ding, M. Chen, C. Wang, T. Wu, and J. Meng, "Deconvolution with fall-off compensated axial point spread function in spectral domain optical coherence tomography," *Opt. Commun.*, vol. 284, no. 12, pp. 3173–3180, Jun. 2011, doi: 10.1016/j.optcom.2011.02.074.

[208] K. M. Kempski, M. T. Graham, M. R. Gubbi, T. Palmer, and M. A. Lediju Bell, "Application of the generalized contrast-to-noise ratio to assess photoacoustic image quality," *Biomed. Opt. Express*, vol. 11, no. 7, p. 3684, Jul. 2020, doi: 10.1364/BOE.391026.

[209] A. Rodriguez-Molares *et al.*, "The Generalized Contrast-to-Noise Ratio: A Formal Definition for Lesion Detectability," *IEEE Trans. Ultrason. Ferroelectr. Freq. Control*, vol. 67, no. 4, pp. 745–759, Apr. 2020, doi: 10.1109/TUFFC.2019.2956855.

[210] J. Liu, C. Garcia-Cardona, B. Wohlberg, and W. Yin, "Online convolutional dictionary learning," in *2017 IEEE International Conference on Image Processing (ICIP)*, IEEE, Sep. 2017, pp. 1707–1711. doi: 10.1109/ICIP.2017.8296573.

[211] M. D. Cox, J. C. Page, A. Trinidade, and J. L. Dornhoffer, "Long-term Complications and Surgical Failures After Ossiculoplasty," *Otol. Neurotol.*, vol. 38, no. 10, pp. 1450–1455, Dec. 2017, doi: 10.1097/MAO.0000000000001572.

[212] J. L. Dornhoffer and E. Gardner, "Prognostic Factors in Ossiculoplasty: A Statistical Staging System:," *Otol. Neurotol.*, vol. 22, no. 3, pp. 299–304, May 2001, doi: 10.1097/00129492-200105000-00005.

[213] J. Knutsson, A. Kahlin, and M. von Unge, "Clinical and audiological short-term and long-term outcomes of fat graft myringoplasty," *Acta Otolaryngol. (Stockh.)*, vol. 137, no. 9, pp. 940–944, Sep. 2017, doi: 10.1080/00016489.2017.1326063.

[214] J. L. Dornhoffer, "Hearing Results With Cartilage Tympanoplasty," *The Laryngoscope*, vol. 107, no. 8, pp. 1094–1099, Aug. 1997, doi: 10.1097/00005537-199708000-00016.

[215] I. Ghanad *et al.*, "A Systematic Review of Nonautologous Graft Materials Used in Human Tympanoplasty," *The Laryngoscope*, vol. 131, no. 2, pp. 392–400, Feb. 2021, doi: 10.1002/lary.28914.

[216] J. Dornhoffer, "Cartilage tympanoplasty: Indications, techniques, and outcomes in A 1,000-patient series," *The Laryngoscope*, vol. 113, no. 11, pp. 1844–1856, Sep. 2010, doi: 10.1097/00005537-200311000-00002.

[217] V. V. Tuchin, "Optical clearing of tissues and blood using the immersion method," *J. Phys. Appl. Phys.*, vol. 38, no. 15, pp. 2497–2518, Aug. 2005, doi: 10.1088/0022-3727/38/15/001.

[218] J. H. Kim *et al.*, "Optimizing tissue-clearing conditions based on analysis of the critical factors affecting tissue-clearing procedures," *Sci. Rep.*, vol. 8, no. 1, p. 12815, Aug. 2018, doi: 10.1038/s41598-018-31153-7.

[219] E. C. Costa, D. N. Silva, A. F. Moreira, and I. J. Correia, "Optical clearing methods: An overview of the techniques used for the imaging of 3D spheroids," *Biotechnol. Bioeng.*, vol. 116, no. 10, pp. 2742–2763, Oct. 2019, doi: 10.1002/bit.27105.

[220] E. A. Genina, A. N. Bashkatov, Yu. P. Sinichkin, and V. V. Tuchin, "Optical clearing of skin under action of glycerol: Ex vivo and in vivo investigations," *Opt. Spectrosc.*, vol. 109, no. 2, pp. 225–231, Aug. 2010, doi: 10.1134/S0030400X10080126.

[221] A. Bykov *et al.*, "Imaging of subchondral bone by optical coherence tomography upon optical clearing of articular cartilage," *J. Biophotonics*, vol. 9, no. 3, pp. 270–275, Mar. 2016, doi: 10.1002/jbio.201500130.

[222] J.-H. Lai, E.-Y. Liao, Y.-H. Liao, and C.-K. Sun, "Investigating the optical clearing effects of 50% glycerol in ex vivo human skin by harmonic generation microscopy," *Sci. Rep.*, vol. 11, no. 1, p. 329, Jan. 2021, doi: 10.1038/s41598-020-77889-z.

[223] I. Costantini, R. Cicchi, L. Silvestri, F. Vanzi, and F. S. Pavone, "In-vivo and ex-vivo optical clearing methods for biological tissues: review," *Biomed. Opt. Express*, vol. 10, no. 10, p. 5251, Oct. 2019, doi: 10.1364/BOE.10.005251.

[224] A. Izquierdo-Román, W. C. Vogt, L. Hyacinth, and C. G. Rylander, "Mechanical tissue optical clearing technique increases imaging resolution and contrast through Ex vivo porcine skin," *Lasers Surg. Med.*, vol. 43, no. 8, pp. 814–823, Sep. 2011, doi: 10.1002/lsm.21105.

[225] Y. He and R. K. Wang, "Dynamic optical clearing effect of tissue impregnated with hyperosmotic agents and studied with optical coherence tomography," *J. Biomed. Opt.*, vol. 9, no. 1, p. 200, 2004, doi: 10.1117/1.1629682.

[226] R. K. Wang, Y. He, and V. V. Tuchin, "Effect of dehydration on optical clearing and OCT imaging contrast after impregnation of biological tissue with biochemical agents," presented at the Biomedical Optics 2004, V. V. Tuchin, J. A. Izatt, and J. G. Fujimoto, Eds., San Jose, CA, Jul. 2004, p. 119. doi: 10.1117/12.531389.

[227] R. K. Wang, X. Xu, V. V. Tuchin, and J. B. Elder, "Concurrent enhancement of imaging depth and contrast for optical coherence tomography by hyperosmotic agents," *J. Opt. Soc. Am. B*, vol. 18, no. 7, p. 948, Jul. 2001, doi: 10.1364/JOSAB.18.000948.

[228] X. Wen, Z. Mao, Z. Han, V. V. Tuchin, and D. Zhu, "In vivo skin optical clearing by glycerol solutions: mechanism," *J. Biophotonics*, vol. 3, no. 1–2, pp. 44–52, Nov. 2009, doi: 10.1002/jbio.200910080.

[229] S.-K. Kong, K.-M. Chon, E.-K. Goh, I.-W. Lee, and S.-G. Wang, "Extratympanic observation of middle ear structure using a refractive index matching material (glycerol) and an infrared camera," *J. Biomed. Opt.*, vol. 19, no. 5, p. 055003, May 2014, doi: 10.1117/1.JBO.19.5.055003.

[230] A. N. Bashkatov *et al.*, "Measurement of tissue optical properties in the context of tissue optical clearing," *J. Biomed. Opt.*, vol. 23, no. 09, p. 1, Aug. 2018, doi: 10.1117/1.JBO.23.9.091416.

[231] K. Aaron, T. E. Cooper, L. Warner, and M. J. Burton, "Ear drops for the removal of ear wax," *Cochrane Database Syst. Rev.*, vol. 2018, no. 10, Jul. 2018, doi: 10.1002/14651858.CD012171.pub2.

[232] R. Mösges, C. M. Baues, T. Schröder, and K. Sahin, "Acute bacterial otitis externa: efficacy and safety of topical treatment with an antibiotic ear drop formulation in comparison to glycerol treatment," *Curr. Med. Res. Opin.*, vol. 27, no. 4, pp. 871–878, Apr. 2011, doi: 10.1185/03007995.2011.557719.

[233] T. I. Goldberg, "Nasal Spray for Decongesting Nasal Passages," US6641799B2 [Online]. Available: https://patents.google.com/patent/US6641799B2/en.

[234] S. M. Hartig, "Basic Image Analysis and Manipulation in ImageJ," *Curr. Protoc. Mol. Biol.*, vol. 102, no. 1, Apr. 2013, doi: 10.1002/0471142727.mb1415s102.

[235] M. M. Khan and S. R. Parab, "Average thickness of tragal cartilage for slicing techniques in tympanoplasty," *J. Laryngol. Otol.*, vol. 129, no. 5, pp. 435–439, May 2015, doi: 10.1017/S0022215115000055.

[236] T. Yu, J. Zhu, D. Li, and D. Zhu, "Physical and chemical mechanisms of tissue optical clearing," *iScience*, vol. 24, no. 3, p. 102178, Mar. 2021, doi: 10.1016/j.isci.2021.102178.

[237] C. M. Cilip, A. E. Ross, J. P. Jarow, and N. M. Fried, "Application of an optical clearing agent during noninvasive laser coagulation of the canine vas deferens," *J. Biomed. Opt.*, vol. 15, no. 4, p. 048001, 2010, doi: 10.1117/1.3463009.

[238] A. Wolfson, C. Dlugy, and Y. Shotland, "Glycerol as a green solvent for high product yields and selectivities," *Environ. Chem. Lett.*, vol. 5, no. 2, pp. 67–71, May 2007, doi: 10.1007/s10311-006-0080-z.

[239] H. Ren, S. Xu, Y. Liu, and S.-T. Wu, "Liquid-based infrared optical switch," *Appl. Phys. Lett.*, vol. 101, no. 4, p. 041104, Jul. 2012, doi: 10.1063/1.4738995.

[240] K. Zheng, B. Liu, C. Huang, and M. E. Brezinski, "Experimental confirmation of potential swept source optical coherence tomography performance limitations," *Appl. Opt.*, vol. 47, no. 33, p. 6151, Nov. 2008, doi: 10.1364/AO.47.006151.

[241] P. Horowitz, *The art of electronics*, Third edition. New York, NY: Cambridge University Press, 2015.

[242] T. Zahnert, K. Huttenbrink, D. Murbe, and M. Bornitz, "Experimental investigations of the use of cartilage in tympanic membrane reconstruction," *Am. J. Otolaryngol.*, vol. 21, no. 3, pp. 322–328, May 2000, doi: 10.1016/S0196-0709(00)80039-3.

[243] F. JW, D. R, and S. C, "Glycerol and the skin: holistic approach to its origin and functions," *Br. J. Dermatol.*, vol. 159, no. 1, pp. 23–34, Jul. 2008, doi: 10.1111/J.1365-2133.2008.08643.X.

[244] Z. Deng *et al.*, "Comparison of Porcine Acellular Dermis and Dura Mater as Natural Scaffolds for Bioengineering Tympanic Membranes," *Tissue Eng. Part A*, vol. 15, no. 12, pp. 3729–3739, Dec. 2009, doi: 10.1089/ten.tea.2008.0460.

[245] D. Sagiv, O. Y. Chin, R. C. Diaz, and H. A. Brodie, "State of the art regeneration of the tympanic membrane," *Curr. Opin. Otolaryngol. Head Neck Surg.*, vol. 28, no. 5, pp. 314–322, Oct. 2020, doi: 10.1097/MOO.0000000000000646.

[246] "Eye Drops, Ear Drops, Nasal Mist - All Natural, Homeopathic - Similasan | Similasan." https://similasan.ca/ (accessed Apr. 14, 2023).

Appendix A: Analytic derivation of OCT interferogram

Optical Coherence Tomography (OCT) employs low coherence interferometry to detect backscattered light from the sample. A classic Michelson interferometer setup, as depicted in Figure A.1 (a), consists of a light source, a reference arm, a sample arm, a beam splitter, and a detector.

Light emanates from the source and travels toward a beam splitter, where it is divided into two separate paths: the reference arm and the sample arm. The light reflected from each arm recombines, creating interference that depends on the optical path lengths of both paths. The detector then converts the interfered light intensity into an electrical signal. One can express the amplitude of the light emanating from the source as [82], [100]:

$$E_o = s(k, \omega)e^{j(kz - \omega t)} \tag{A.1}$$

where E_o is the electric field amplitude and $s(k, \omega)$ is the slow-varying complex envelope of the electric field. $s(k, \omega)$ is the function of wavenumber $k = 2\pi/\lambda$ and angular frequency $\omega = 2\pi\nu$ where λ and ν represents the wavelength and the frequency of the light wave.
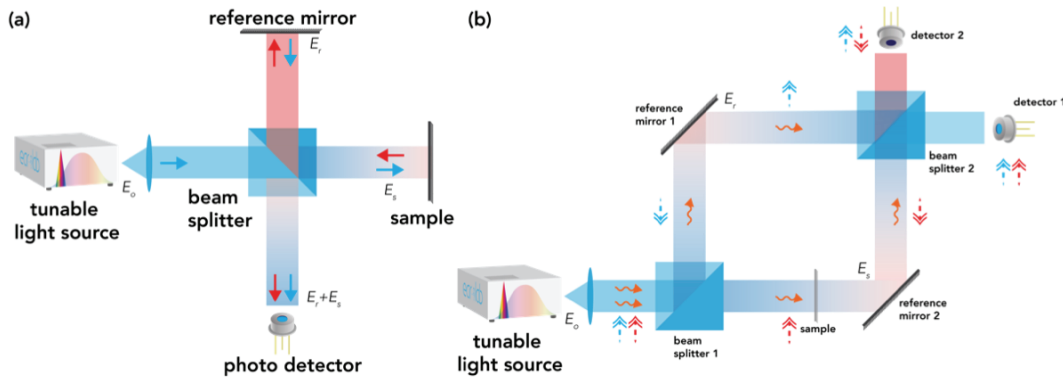
Figure A.1: FD-OCT system in (a) classic Michelson configuration where solid red and blue arrows indicate the direction of light waves propagating in the optical path and (b) Mach-Zehnder configuration, where the curly orange arrow indicates the direction of light waves propagating in the optical path whereas dashed red and blue indicate the phase of the light.

We can further express the light wave reflected from the reference and sample arms as

$$E_r = \frac{E_o}{\sqrt{2}} \alpha_r e^{j2kz_r} \tag{A.2}$$

$$E_s = \frac{E_o}{\sqrt{2}} \alpha_s e^{j2k\hat{n}z_s} \tag{A.3}$$

E_r, α_r, and z_r denote the reflected light wave, reflectivity and path length of the reference arm, while E_s, α_s, and z_s represent the same properties for the sample arm. $\hat{n}$ is the complex refractive index where $\hat{n} = n + i\alpha$ includes both refraction and losses [82], [100], where we substitute $\hat{n}$ with n for the sake of clarity and simplicity in the following derivation. The term $\frac{1}{\sqrt{2}}$ comes from splitting of light power in half at the beam splitter. The detector converts the combined light waves from both arms where we assume the responsivity of the detector to be 1 for simplicity:

$$
\begin{aligned}
I(k) &= \; < \frac{|E_r + E_s|^2}{2} > \\
I(k) &= \frac{1}{2} < |E_r|^2 + |E_s|^2 + E_r E_s^* + E_r^* E_s > \\
I(k) &= \frac{1}{4} < |E_o|^2 \alpha_r + |E_o|^2 \alpha_s + 2|E_o|^2 \sqrt{\alpha_r \alpha_s} (e^{j2kn(z_r - z_s)} \\
&\quad + e^{-j2kn(z_r - z_s)}) > \\
I(k) &= \frac{1}{4} < |E_o|^2 \alpha_r + |E_o|^2 \alpha_s + 2|E_o|^2 \sqrt{\alpha_r \alpha_s} [\cos (2kn(z_r - z_s)] > \\
I(k) &= \frac{|s(k)|^2}{4} < \alpha_r + \alpha_s + 2\sqrt{\alpha_r \alpha_s} \cos(2kn\Delta z) >
\end{aligned}
\tag{A.4}
$$

where $z_r - z_s = \Delta z$. (A.4) suggests the wavenumber, k, allows for encoding the path length difference between the reference and sample arms and it is inverse of the wavelength by $k = 2\pi/\lambda$.

In a comparison between the Michelson and Mach-Zehnder interferometers, the distinguishing factor is their distinct geometrical arrangements. The Mach-Zehnder interferometer, in particular, is characterized by the presence of two beam splitters. This configuration effectively separates the optical path of light returning from the reference arm and sample arm, a distinction that sets it apart from the Michelson interferometer.

The total separation of the of optical paths allows for a greater flexibility in the system design and achieving higher degree of beam splitting efficiency [81]. In the case of SS-OCT, an improved configuration could be considered. Instead of a conventional 50:50 ratio in both beam splitters, one might alter the arrangement. The first beam splitter could use a 90:10 ratio, favoring the power directed towards the sample arm. Meanwhile, the second beam splitter can maintain a balanced 50:50 ratio, ensuring an optimized detection [106]. This alteration could potentially enhance the performance and sensitivity of the SS-OCT system and it is also important to point out the optimal ratio can depend on many factors, such as the specific characteristics of the sample and remains to be a much-debated topic [82]. In addition, Mach-Zehnder interferometer features two outputs that complement each other with a phase difference of π. Assuming beam splitter 1 splits the light equally and simplify the discussion by omitting the full forms of the wave equations:

$$E_r = E_s = \frac{E_o}{\sqrt{2}} \tag{A.5}$$

The two waves are then recombined at the second beam splitter (50:50 beam splitter) to produce two output waves at each detector:

$$E_1 = \frac{E_r - E_s}{\sqrt{2}} \; ; \; E_2 = \frac{E_r + E_s}{\sqrt{2}} \tag{A.6}$$

The difference in sign accounts for the cumulative phase shift that occurs as light propagates through the beam splitters. When a sample is positioned in the sample arm and introduces a phase shift, $\Delta\varphi$, this leads a change in the intensity of the beam entering the two detectors:

$$I_1 = |E_1|^2 = |E_o|^2 \cdot [1 - \cos(\Delta\varphi)]/2 \tag{A.7}$$

$$I_2 = |E_2|^2 = |E_o|^2 \cdot [1 + \cos(\Delta\varphi)]/2 \tag{A.8}$$

Appendix B: Permission of reproduction

This appendix includes the essential written permissions for reproducing content from the two journal articles that form the foundation of Chapter 3 - Chapter 4 in accordance with Dalhousie University's copyright requirements for thesis submission, it also contains permissions for reproducing borrowed materials featured in Figure 1.1, Figure 1.2 and Figure 2.1. These permissions ensure compliance with intellectual property guidelines.

Appendix B.1: Copyright permission for Figure 1.1

CCC Marketplace

This is a License Agreement between Junzhe Wang ("User") and Copyright Clearance Center, Inc. ("CCC") on behalf of the Rightsholder identified in the order details below. The license consists of the order details, the Marketplace Permissions General Terms and Conditions below, and any Rightsholder Terms and Conditions which are included below.

All payments must be made in full to CCC in accordance with the Marketplace Permissions General Terms and Conditions below.

Order Date	26-Mar-2023	Type of Use	Republish in a thesis/dissertation
Order License ID	1338240-1		
ISBN-13	9783642369667	Publisher	Springer Berlin Heidelberg
		Portion	Chart/graph/table/figure

LICENSED CONTENT

Publication Title	Comprehensive and Clinical Anatomy of the Middle Ear	Country	Germany
		Rightsholder	Springer
Author/Editor	Mansour, Salah, Magnan, Jacques, Haidar, Hassan, Nicolas, Karen, Louryan, Stéphane	Publication Type	Book
Date	05/31/2013		
Language	English		

REQUEST DETAILS

Portion Type	Chart/graph/table/figure	Distribution	United States and Canada
Number of Charts / Graphs / Tables / Figures Requested	1	Translation	Original language of publication
		Copies for the Disabled?	No
Format (select all that apply)	Print, Electronic	Minor Editing Privileges?	Yes
Who Will Republish the Content?	Academic institution	Incidental Promotional Use?	Yes
Duration of Use	Current edition and up to 5 years	Currency	CAD
Lifetime Unit Quantity	Up to 499		
Rights Requested	Main product		

NEW WORK DETAILS

Title	Improved middle ear imaging with optical coherence tomography for clinical otology	Institution Name	Dalhousie University
		Expected Presentation Date	2023-03-27
Instructor Name	Junzhe Wang		

ADDITIONAL DETAILS

| Order Reference Number | N/A | The Requesting Person/Organization to Appear on the License | Junzhe Wang |

REQUESTED CONTENT DETAILS

Title, Description or Numeric Reference of the Portion(s)	Comprehensive and Clinical Anatomy of the Middle Ear	Title of the Article/Chapter the Portion Is From	Middle Ear Cavity.
Editor of Portion(s)	N/A	Author of Portion(s)	Mansour, Salah; Magnan, Jacques; Haidar, Hassan; Nicolas, Karen; Louryan, Stéphane
Volume of Serial or Monograph	N/A		
Page or Page Range of Portion	25	Issue, if Republishing an Article From a Serial	N/A
		Publication Date of Portion	2013-05-31

RIGHTSHOLDER TERMS AND CONDITIONS

A maximum of 10% of the content may be licensed for republication. The user is responsible for identifying and seeking separate licenses for any third party materials that are identified anywhere in the work. Without a separate license, such third party materials may not be reused.

If you are placing a request on behalf of/for a corporate organization, please use RightsLink. For further information visit http://www.nature.com/reprints/permission-requests.html and https://www.springer.com/gp/rights-permissions/obtaining-permissions/882. If the content you are requesting to reuse is under a CC-BY 4.0 licence (or previous version), you do not need to seek permission from Springer Nature for this reuse as long as you provide appropriate credit to the original publication. https://creativecommons.org/licenses/by/4.0/ STM Permissions Guidelines STM Permissions Guidelines (2022) - STM (stm-assoc.org) will complement the Terms & Conditions on this page CCC Payment T&Cs (copyright.com)

Marketplace Permissions General Terms and Conditions

The following terms and conditions ("General Terms"), together with any applicable Publisher Terms and Conditions, govern User's use of Works pursuant to the Licenses granted by Copyright Clearance Center, Inc. ("CCC") on behalf of the applicable Rightsholders of such Works through CCC's applicable Marketplace transactional licensing services (each, a "Service").

1) **Definitions.** For purposes of these General Terms, the following definitions apply:

"License" is the licensed use the User obtains via the Marketplace platform in a particular licensing transaction, as set forth in the Order Confirmation.

"Order Confirmation" is the confirmation CCC provides to the User at the conclusion of each Marketplace transaction. "Order Confirmation Terms" are additional terms set forth on specific Order Confirmations not set forth in the General Terms that can include terms applicable to a particular CCC transactional licensing service and/or any Rightsholder-specific terms.

"Rightsholder(s)" are the holders of copyright rights in the Works for which a User obtains licenses via the Marketplace platform, which are displayed on specific Order Confirmations.

"Terms" means the terms and conditions set forth in these General Terms and any additional Order Confirmation Terms collectively.

"User" or "you" is the person or entity making the use granted under the relevant License. Where the person accepting the Terms on behalf of a User is a freelancer or other third party who the User authorized to accept the General Terms on the User's behalf, such person shall be deemed jointly a User for purposes of such Terms.

"Work(s)" are the copyright protected works described in relevant Order Confirmations.

2) **Description of Service.** CCC's Marketplace enables Users to obtain Licenses to use one or more Works in accordance with all relevant Terms. CCC grants Licenses as an agent on behalf of the copyright rightsholder identified in the relevant Order Confirmation.

3) **Applicability of Terms.** The Terms govern User's use of Works in connection with the relevant License. In the event of any conflict between General Terms and Order Confirmation Terms, the latter shall govern. User acknowledges that Rightsholders have complete discretion whether to grant any permission, and whether to place any limitations on any grant, and that CCC has no right to supersede or to modify any such discretionary act by a Rightsholder.

4) **Representations; Acceptance.** By using the Service, User represents and warrants that User has been duly authorized by the User to accept, and hereby does accept, all Terms.

5) **Scope of License; Limitations and Obligations.** All Works and all rights therein, including copyright rights, remain the sole and exclusive property of the Rightsholder. The License provides only those rights expressly set forth in the terms and conveys no other rights in any Works

6) **General Payment Terms.** User may pay at time of checkout by credit card or choose to be invoiced. If the User chooses to be invoiced, the User shall: (i) remit payments in the manner identified on specific invoices, (ii) unless otherwise specifically stated in an Order Confirmation or separate written agreement, Users shall remit payments upon receipt of the relevant invoice from CCC, either by delivery or notification of availability of the invoice via the Marketplace platform, and (iii) if the User does not pay the invoice within 30 days of receipt, the User may incur a service charge of 1.5% per month or the maximum rate allowed by applicable law, whichever is less. While User may exercise the rights in the License immediately upon receiving the Order Confirmation, the License is automatically revoked and is null and void, as if it had never been issued, if CCC does not receive complete payment on a timely basis.

7) **General Limits on Use.** Unless otherwise provided in the Order Confirmation, any grant of rights to User (i) involves only the rights set forth in the Terms and does not include subsequent or additional uses, (ii) is non-exclusive and non-transferable, and (iii) is subject to any and all limitations and restrictions (such as, but not limited to, limitations on duration of use or circulation) included in the Terms. Upon completion of the licensed use as set forth in the Order Confirmation, User shall either secure a new permission for further use of the Work(s) or immediately cease any new use of the Work(s) and shall render inaccessible (such as by deleting or by removing or severing links or other locators) any further copies of the Work. User may only make alterations to the Work if and as expressly set forth in the Order Confirmation. No Work may be used in any way that is unlawful, including without limitation if such use would violate applicable sanctions laws or regulations, would be defamatory, violate the rights of third parties (including such third parties' rights of copyright, privacy, publicity, or other tangible or intangible property), or is otherwise illegal, sexually explicit, or obscene. In addition, User may not conjoin a Work with any other material that may result in damage to the reputation of the Rightsholder. Any unlawful use will render any licenses hereunder null and void. User agrees to inform CCC if it becomes aware of any infringement of any rights in a Work and to cooperate with any reasonable request of CCC or the Rightsholder in connection therewith.

8) **Third Party Materials.** In the event that the material for which a License is sought includes third party materials (such as photographs, illustrations, graphs, inserts and similar materials) that are identified in such material as having been used by permission (or a similar indicator), User is responsible for identifying, and seeking separate licenses (under this Service, if available, or otherwise) for any of such third party materials; without a separate license, User may not use such third party materials via the License.

9) **Copyright Notice.** Use of proper copyright notice for a Work is required as a condition of any License granted under the Service. Unless otherwise provided in the Order Confirmation, a proper copyright notice will read substantially as follows: "Used with permission of [Rightsholder's name], from [Work's title, author, volume, edition number and year of copyright]; permission conveyed through Copyright Clearance Center, Inc." Such notice must be provided in a reasonably legible font size and must be placed either on a cover page or in another location that any person, upon gaining access to the material which is the subject of a permission, shall see, or in the case of republication Licenses, immediately adjacent to the Work as used (for example, as part of a by-line or footnote) or in the place where substantially all other credits or notices for the new work containing the republished Work are located. Failure to include the required notice results in loss to the Rightsholder and CCC, and the User shall be liable to pay liquidated damages for each such failure equal to twice the use fee specified in the Order Confirmation, in addition to the use fee itself and any other fees and charges specified.

10) **Indemnity.** User hereby indemnifies and agrees to defend the Rightsholder and CCC, and their respective employees and directors, against all claims, liability, damages, costs, and expenses, including legal fees and expenses, arising out of any use of a Work beyond the scope of the rights granted herein and in the Order Confirmation, or any use of a Work which has been altered in any unauthorized way by User, including claims of defamation or infringement of rights of copyright, publicity, privacy, or other tangible or intangible property.

11) **Limitation of Liability.** UNDER NO CIRCUMSTANCES WILL CCC OR THE RIGHTSHOLDER BE LIABLE FOR ANY DIRECT, INDIRECT, CONSEQUENTIAL, OR INCIDENTAL DAMAGES (INCLUDING WITHOUT LIMITATION DAMAGES FOR LOSS OF BUSINESS PROFITS OR INFORMATION, OR FOR BUSINESS INTERRUPTION) ARISING OUT OF THE USE OR INABILITY TO USE A WORK, EVEN IF ONE OR BOTH OF THEM HAS BEEN ADVISED OF THE POSSIBILITY OF SUCH DAMAGES. In any event, the total liability of the Rightsholder and CCC (including their respective employees and directors) shall not exceed the total amount actually paid by User for the relevant License. User assumes full liability for the actions and omissions of its principals, employees, agents, affiliates, successors, and assigns.

12) **Limited Warranties.** THE WORK(S) AND RIGHT(S) ARE PROVIDED "AS IS." CCC HAS THE RIGHT TO GRANT TO USER THE RIGHTS GRANTED IN THE ORDER CONFIRMATION DOCUMENT. CCC AND THE RIGHTSHOLDER DISCLAIM ALL OTHER WARRANTIES RELATING TO THE WORK(S) AND RIGHT(S), EITHER EXPRESS OR IMPLIED, INCLUDING WITHOUT LIMITATION IMPLIED WARRANTIES OF MERCHANTABILITY OR FITNESS FOR A PARTICULAR PURPOSE. ADDITIONAL RIGHTS MAY BE REQUIRED TO USE ILLUSTRATIONS, GRAPHS, PHOTOGRAPHS, ABSTRACTS, INSERTS, OR OTHER PORTIONS OF THE WORK (AS OPPOSED TO THE ENTIRE WORK) IN A MANNER CONTEMPLATED BY USER; USER UNDERSTANDS AND AGREES THAT NEITHER CCC NOR THE RIGHTSHOLDER MAY HAVE SUCH ADDITIONAL RIGHTS TO GRANT.

13) **Effect of Breach.** Any failure by User to pay any amount when due, or any use by User of a Work beyond the scope of the License set forth in the Order Confirmation and/or the Terms, shall be a material breach of such License. Any breach not cured within 10 days of written notice thereof shall result in immediate termination of such License without further notice. Any unauthorized (but licensable) use of a Work that is terminated immediately upon notice thereof may be liquidated by payment of the Rightsholder's ordinary license price therefor; any unauthorized (and unlicensable) use that is not terminated immediately for any reason (including, for example, because materials containing the Work cannot reasonably be recalled) will be subject to all remedies available at law or in equity, but in no event to a payment of less than three times the Rightsholder's ordinary license price for the most closely analogous licensable use plus Rightsholder's and/or CCC's costs and expenses incurred in collecting such payment.

14) **Additional Terms for Specific Products and Services.** If a User is making one of the uses described in this Section 14, the additional terms and conditions apply:

a) *Print Uses of Academic Course Content and Materials (photocopies for academic coursepacks or classroom handouts).* For photocopies for academic coursepacks or classroom handouts the following additional terms apply:

i) The copies and anthologies created under this License may be made and assembled by faculty members individually or at their request by on-campus bookstores or copy centers, or by off-campus copy shops and other similar entities.

ii) No License granted shall in any way: (i) include any right by User to create a substantively non-identical copy of the Work or to edit or in any other way modify the Work (except by means of deleting material immediately preceding or following the entire portion of the Work copied) (ii) permit "publishing ventures" where any particular anthology would be systematically marketed at multiple institutions.

iii) Subject to any Publisher Terms (and notwithstanding any apparent contradiction in the Order Confirmation arising from data provided by User), any use authorized under the academic pay-per-use service is limited as follows:

A) any License granted shall apply to only one class (bearing a unique identifier as assigned by the institution, and thereby including all sections or other subparts of the class) at one institution;

B) use is limited to not more than 25% of the text of a book or of the items in a published collection of essays, poems or articles;

C) use is limited to no more than the greater of (a) 25% of the text of an issue of a journal or other periodical or (b) two articles from such an issue;

D) no User may sell or distribute any particular anthology, whether photocopied or electronic, at more than one institution of learning;

E) in the case of a photocopy permission, no materials may be entered into electronic memory by User except in order to produce an identical copy of a Work before or during the academic term (or analogous period) as to which any particular permission is granted. In the event that User shall choose to retain materials that are the subject of a photocopy permission in electronic memory for purposes of producing identical copies more than one day after such retention (but still within the scope of any permission granted), User must notify CCC of such fact in the applicable permission request and such retention shall constitute one copy actually sold for purposes of calculating permission fees due; and

F) any permission granted shall expire at the end of the class. No permission granted shall in any way include any right by User to create a substantively non-identical copy of the Work or to edit or in any other way modify the Work (except by means of deleting material immediately preceding or following the entire portion of the Work copied).

iv) Books and Records; Right to Audit. As to each permission granted under the academic pay-per-use Service, User shall maintain for at least four full calendar years books and records sufficient for CCC to determine the numbers of copies made by User under such permission. CCC and any representatives it may designate shall have the right to audit such books and records at any time during User's ordinary business hours, upon two days' prior notice. If any such audit shall determine that User shall have underpaid for, or underreported, any photocopies sold or by three percent (3%) or more, then User shall bear all the costs of any such audit; otherwise, CCC shall bear the costs of any such audit. Any amount determined by such audit to have been underpaid by User shall immediately be paid to CCC by User, together with interest thereon at the rate of 10% per annum from the date such amount was originally due. The provisions of this paragraph shall survive the termination of this License for any reason.

b) *Digital Pay-Per-Uses of Academic Course Content and Materials (e-coursepacks, electronic reserves, learning management systems, academic institution intranets).* For uses in e-coursepacks, posts in electronic reserves, posts in learning management systems, or posts on academic institution intranets, the following additional terms apply:

i) The pay-per-uses subject to this Section 14(b) include:

A) **Posting e-reserves, course management systems, e-coursepacks for text-based content**, which grants authorizations to import requested material in electronic format, and allows electronic access to this material to members of a designated college or university class, under the direction of an instructor designated by the college or university, accessible only under appropriate electronic controls (e.g., password);

B) **Posting e-reserves, course management systems, e-coursepacks for material consisting of photographs or other still images not embedded in text**, which grants not only the authorizations described in Section 14(b)(i)(A) above, but also the following authorization: to include the requested material in course materials for use consistent with Section 14(b)(i)(A) above, including any necessary resizing, reformatting or modification of the resolution of such requested material (provided that such modification does not alter the underlying editorial content or meaning of the requested material, and provided that the resulting modified content is used solely within the scope of, and in a manner consistent with, the particular authorization described in the Order Confirmation and the Terms), but not including any other form of manipulation, alteration or editing of the requested material;

C) **Posting e-reserves, course management systems, e-coursepacks or other academic distribution for audiovisual content**, which grants not only the authorizations described in Section 14(b)(i)(A) above, but also the following authorizations: (i) to include the requested material in course materials for use consistent with Section 14(b)(i)(A) above; (ii) to display and perform the requested material to such members of such class in the physical classroom or remotely by means of streaming media or other video formats; and (iii) to "clip" or reformat the requested material for purposes of time or content management or ease of delivery, provided that such "clipping" or reformatting does not alter the underlying editorial content or meaning of the requested material and that the resulting material is used solely within the scope of, and in a manner consistent with, the particular authorization described in the Order Confirmation and the Terms. Unless expressly set forth in the relevant Order Conformation, the License does not authorize any other form of manipulation, alteration or editing of the requested material.

ii) Unless expressly set forth in the relevant Order Confirmation, no License granted shall in any way: (i) include any right by User to create a substantively non-identical copy of the Work or to edit or in any other way modify the Work (except by means of deleting material immediately preceding or following the entire portion of the Work copied or, in the case of Works subject to Sections 14(b)(1)(B) or (C) above, as described in such Sections) (ii) permit "publishing ventures" where any particular course materials would be systematically marketed at multiple institutions.

iii) Subject to any further limitations determined in the Rightsholder Terms (and notwithstanding any apparent contradiction in the Order Confirmation arising from data provided by User), any use authorized under the electronic course content pay-per-use service is limited as follows:

A) any License granted shall apply to only one class (bearing a unique identifier as assigned by the institution, and thereby including all sections or other subparts of the class) at one institution;

B) use is limited to not more than 25% of the text of a book or of the items in a published collection of essays, poems or articles;

C) use is limited to not more than the greater of (a) 25% of the text of an issue of a journal or other periodical or (b) two articles from such an issue;

D) no User may sell or distribute any particular materials, whether photocopied or electronic, at more than one institution of learning;

E) electronic access to material which is the subject of an electronic-use permission must be limited by means of electronic password, student identification or other control permitting access solely to students and instructors in the class;

F) User must ensure (through use of an electronic cover page or other appropriate means) that any person, upon gaining electronic access to the material, which is the subject of a permission, shall see:

- a proper copyright notice, identifying the Rightsholder in whose name CCC has granted permission,

- a statement to the effect that such copy was made pursuant to permission,

- a statement identifying the class to which the material applies and notifying the reader that the material has been made available electronically solely for use in the class, and

- a statement to the effect that the material may not be further distributed to any person outside the class, whether by copying or by transmission and whether electronically or in paper form, and User must also ensure that such cover page or other means will print out in the event that the person accessing the material chooses to print out the material or any part thereof.

G) any permission granted shall expire at the end of the class and, absent some other form of authorization, User is thereupon required to delete the applicable material from any electronic storage or to block electronic access to the applicable material.

iv) Uses of separate portions of a Work, even if they are to be included in the same course material or the same university or college class, require separate permissions under the electronic course content pay-per-use Service. Unless otherwise provided in the Order Confirmation, any grant of rights to User is limited to use completed no later than the end of the academic term (or analogous period) as to which any particular permission is granted.

v) Books and Records; Right to Audit. As to each permission granted under the electronic course content Service, User shall maintain for at least four full calendar years books and records sufficient for CCC to determine the numbers of copies made by User under such permission. CCC and any representatives it may designate shall have the right to audit such books and records at any time during User's ordinary business hours, upon two days' prior notice. If any such audit shall determine that User shall have underpaid for, or underreported, any electronic copies used by three percent (3%) or more, then User shall bear all the costs of any such audit; otherwise, CCC shall bear the costs of any such audit. Any amount determined by such audit to have been underpaid by User shall immediately be paid to CCC by User, together with interest thereon at the rate of 10% per annum from the date such amount was originally due. The provisions of this paragraph shall survive the termination of this license for any reason.

c) *Pay-Per-Use Permissions for Certain Reproductions (Academic photocopies for library reserves and interlibrary loan reporting) (Non-academic internal/external business uses and commercial document delivery).* The License expressly excludes the uses listed in Section (c)(i)-(v) below (which must be subject to separate license from the applicable Rightsholder) for: academic photocopies for library reserves and interlibrary loan reporting; and non-academic internal/external business uses and commercial document delivery.

i) electronic storage of any reproduction (whether in plain-text, PDF, or any other format) other than on a transitory basis;

ii) the input of Works or reproductions thereof into any computerized database;

iii) reproduction of an entire Work (cover-to-cover copying) except where the Work is a single article;

iv) reproduction for resale to anyone other than a specific customer of User;

v) republication in any different form. Please obtain authorizations for these uses through other CCC services or directly from the rightsholder.

Any license granted is further limited as set forth in any restrictions included in the Order Confirmation and/or in these Terms.

d) *Electronic Reproductions in Online Environments (Non-Academic-email, intranet, internet and extranet).* For "electronic reproductions", which generally includes e-mail use (including instant messaging or other electronic transmission to a defined group of recipients) or posting on an intranet, extranet or Intranet site (including any display or performance incidental thereto), the following additional terms apply:

i) Unless otherwise set forth in the Order Confirmation, the License is limited to use completed within 30 days for any use on the Internet, 60 days for any use on an intranet or extranet and one year for any other use, all as measured from the "republication date" as identified in the Order Confirmation, if any, and otherwise from the date of the Order Confirmation.

ii) User may not make or permit any alterations to the Work, unless expressly set forth in the Order Confirmation (after request by User and approval by Rightsholder); provided, however, that a Work consisting of photographs or other still images not embedded in text may, if necessary, be resized, reformatted or have its resolution modified without additional express permission, and a Work consisting of audiovisual content may, if necessary, be "clipped" or reformatted for purposes of time or content management or ease of delivery (provided that any such resizing, reformatting, resolution modification or "clipping" does not alter the underlying editorial content or meaning of the Work used, and that the resulting material is used solely within the scope of, and in a manner consistent with, the particular License described in the Order Confirmation and the Terms.

15) **Miscellaneous.**

a) User acknowledges that CCC may, from time to time, make changes or additions to the Service or to the Terms, and that Rightsholder may make changes or additions to the Rightsholder Terms. Such updated Terms will replace the prior terms and conditions in the order workflow and shall be effective as to any subsequent Licenses but shall not apply to Licenses already granted and paid for under a prior set of terms.

b) Use of User-related information collected through the Service is governed by CCC's privacy policy, available online at www.copyright.com/about/privacy-policy/.

c) The License is personal to User. Therefore, User may not assign or transfer to any other person (whether a natural person or an organization of any kind) the License or any rights granted thereunder; provided, however, that, where applicable, User may assign such License in its entirety on written notice to CCC in the event of a transfer of all or substantially all of User's rights in any new material which includes the Work(s) licensed under this Service.

d) No amendment or waiver of any Terms is binding unless set forth in writing and signed by the appropriate parties, including, where applicable, the Rightsholder. The Rightsholder and CCC hereby object to any terms contained in any writing prepared by or on behalf of the User or its principals, employees, agents or affiliates and purporting to govern or otherwise relate to the License described in the Order Confirmation, which terms are in any way inconsistent with any Terms set forth in the Order Confirmation, and/or in CCC's standard operating procedures, whether such writing is prepared prior to, simultaneously with or subsequent to the Order Confirmation, and whether such writing appears on a copy of the Order Confirmation or in a separate instrument.

e) The License described in the Order Confirmation shall be governed by and construed under the law of the State of New York, USA, without regard to the principles thereof of conflicts of law. Any case, controversy, suit, action, or proceeding arising out of, in connection with, or related to such License shall be brought, at CCC's sole discretion, in any federal or state court located in the County of New York, State of New York, USA, or in any federal or state court whose geographical jurisdiction covers the location of the Rightsholder set forth in the Order Confirmation. The parties expressly submit to the personal jurisdiction and venue of each such federal or state court.

Last updated October 2022

Appendix B.2: Copyright permission for Figure 1.2

2023.06.14

Dear Optica copyright officer,

I am preparing my master's degree thesis for submission to the Faculty of Graduate Studies at Dalhousie University, Halifax, Nova Scotia, Canada. I am seeking your permission to include a manuscript version of the following paper(s) as a chapter in the thesis:

1. Figure 5, subplot (a) from
   In vivo imaging of middle-ear and inner-ear microstructures of a mouse guided by SD-OCT combined with a surgical microscope

2. Figure 9, subplot (a) from
   Picometer scale vibrometry in the human middle ear using a surgical microscope based optical coherence tomography and vibrometry system

Dalhousie graduate theses are collected and stored online by Dalhousie University and Library and Archives of Canada. I am seeking your permission for the material described above to be stored online in Dalhousie University's institutional repository and in Library and Archives of Canada (LAC)'s Theses Canada Collection.

Full publication details and a copy of this permission letter will be included in the thesis.

Yours sincerely,

Young Wang

---

Permission is granted for:

a) the inclusion of the material described above in your thesis.

b) **for the material described above to be included in the copy of your thesis that is sent to the Library and Archives of Canada inclusion in Theses Canada.**

c) **For the material described above to be included in the copy of your thesis that is sent to Dalhousie University's institutional repository.**

Name:	Hannah Greenwood	Title:	Authorized Agent, Optica Publishing Group
Signature:	████████████	Date:	6/27/2023

Appendix B.3: Copyright permission for Figure 2.1
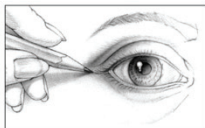
THESIS COPYRIGHT PERMISSION FORM

Title(s) of the Image(s): Chris Gralapp owns the copyright to the following image(s):

Title(s) of illustration(s):
1.Coronal perspective of the anatomy of the ear
https://otosurgeryatlas.stanford.edu/otologic-surgery-atlas/surgical-anatomy-of-the-ear/overview-of-temporal-bone/#iLightbox[gallery_image_1]/0

2. Sliding the cartilage beneath the scutal edge helps stability the prosthesis by creating longitudinal tension
https://otosurgeryatlas.stanford.edu/otologic-surgery-atlas/ossiculoplasty/ossiculoplasty-placement-technique/#iLightbox[gallery_image_1]/5

Description of the Work: Chris Gralapp hereby grants permission to reproduce the above image(s) for use in the work specified:

Thesis title: Improved middle ear imaging with optical coherence tomography for clinical otology
University : Dalhousie University
Digital Object Identifier (DOI) and Journal ISSN, if available:N/A

License Granted: Chris Gralapp hereby grants limited, non-exclusive worldwide print and electronic rights only for use in the Work specified. Chris Gralapp grants such rights "AS IS" without representation or warranty of any kind and shall have no liability in connection with such license.

Restrictions: Reproduction for use in any other work, derivative works, or by any third party by manual or electronic methods is prohibited. Ownership of original artwork, copyright, and all rights not specifically transferred herein remain the exclusive property of Chris Gralapp. Additional license(s) are required for ancillary usage(s).

Credit must be placed adjacent to the image(s) in the following format:

© *(copyright year)* Chris Gralapp, used with permission

Permission granted to:
Name: Junzhe (Young) Wang
Mailing address: 63 Portland Estates Blvd W, Dartmouth, NS B2W 6E5, Canada
Email address: Junzhe.wang@dal.ca
Phone number: (902)-830-7568

Signature_____ Date_____

Junzhe Wang

Signature_____ Date_____

Chris Gralapp, CMI

Christine Gralapp | Medical Illustration
204 Ridgeway Avenue, Fairfax, CA 94930
(415) 454-6567
eyeart@chrisgralapp.com
www.chrisgralapp.com

1

Appendix B.4: Copyright permission for Chapter 3

Subject:	RE: Copyright request[https://doi.org/10.1364/BOE.447394] for thesis use
Date:	Friday, February 24, 2023 at 12:15:42 Atlantic Standard Time
From:	Optica Publishing Group Copyright
To:	Young Wang, Optica Publishing Group Copyright

Attachments: image002.png

Dear Young Wang,

Thank you for contacting Optica Publishing Group.
For the use of material from Junzhe Wang, Brendt Wohlberg, and R. B. A. Adamson, "Convolutional dictionary learning for blind deconvolution of optical coherence tomography images," Biomed. Opt. Express 13, 1834-1854 (2022):

> Because you are the author of the source paper from which you wish to reproduce material, Optica Publishing Group considers your requested use of its copyrighted materials to be permissible within the author rights granted in the Copyright Transfer and Open Access Publishing Agreement submitted by the requester on acceptance for publication of his/her manuscript. It is requested that a complete citation of the original material be included in any publication. This permission assumes that the material was not reproduced from another source when published in the original publication.

> If the entire article is being included, it is permissible to use the **version of record**.

While your publisher should be able to provide additional guidance, we prefer the below citation formats:

> For citations in figure captions:

> [Reprinted/Adapted] with permission from [ref #] © Optica Publishing Group. (Please include the full citation in your reference list)

> For images without captions:

> Journal Vol. #, first page (year published) An example: Opt. Express 19, 2720 (2011)

Please let me know if you have any questions.

Kind Regards,
Hannah Greenwood

Hannah Greenwood
February 24, 2023
Authorized Agent, Optica Publishing Group

OPTICA
PUBLISHING GROUP | Formerly **OSA**

Appendix B.5: Copyright permission for Chapter 4

CCC
RightsLink

Home | Help ∨ | Live Chat | Sign in | Create Account

Wolters Kluwer

Optical Clearing Agents for Optical Imaging Through Cartilage Tympanoplasties: A Preclinical Feasibility Study

Author: Junzhe Wang, Gaurav Chawdhary, Xiaojie Yang, et al
Publication: Otology & Neurotology
Publisher: Wolters Kluwer Health, Inc.
Date: Apr 1, 2022

Copyright © 2022, © 2022, Otology

License Not Required

Wolters Kluwer policy permits only the final peer-reviewed manuscript of the article to be reused in a thesis. You are free to use the final peer-reviewed manuscript in your print thesis at this time, and in your electronic thesis 12 months after the article's publication date. The manuscript may only appear in your electronic thesis if it will be password protected. Please see our Author Guidelines here: https://cdn-tp2.mozu.com/16833-m1/cms/files/Author-Document.pdf?_mzts=636410951730000000.

BACK   CLOSE WINDOW